Contents

Strojniški vestnik - Journal of Mechanical Engineering
volume 64, (2018), number 2
Ljubljana, February 2018
ISSN 0039-2480

Published monthly

Papers

Strojniški vestnik - Journal of Mechanical Engineering 64(2018)2, 73-81
DOI:10.5545/sv-jme.2017.4915
Original Scientific Paper
Received for review: 2017-09-12
Received revised form: 2018-01-06
Accepted for publication: 2018-01-25

Introduction of Welds into the Dynamic Model of Laminated Structures

Primož Ogrinec — Gregor Čepon* — Miha Boltežar
University of Ljubljana, Faculty of Mechanical Engineering, Slovenia

Laminated structures, like an electric stator package, exhibit orthotropic behaviour and high levels of internal damping due to the inter-laminar friction forces. Modelling the complex geometry, number of laminae, spatial pressure distribution, and the effects of welds on the dynamic response of laminated structure remains a challenging issue. The presence of welds, that serve as a physical connection between laminae, results in non-uniform pressure distribution between laminae. Usually orthotropic material properties are proposed to account for lower stiffness in the sheet stacking direction. These models assume uniform distribution of friction forces and may even lead to occurrence of additional, unrealistic mode shapes. In this paper the dynamics model of the electric machine stator is proposed that employs a new contact formulation using beam elements, characterized by stiffness and damping parameters in the tangential direction and nonlinear contact stiffness in the normal contact direction. The welds and the welding process itself are represented using spring-thermo elasto-plastic bar model. As the contact model assumes nonuniform pressure distribution it is possible to include the effect of residual stresses that occur after the welding process. The validity of developed numerical model is demonstrated by comparing numerically and experimentally obtained eigenfrequencies and modes for three different stator packets that differ in geometry, position and the number of welds.

Keywords: Laminated structure, electric stator package, dynamics, contact model, weld, modal analysis

Highlights

- *Laminated structures are significantly more flexible as their solid counterparts and are often welded to preserve shape.*
- *Welding process affects the pressure distribution between the laminae, which greatly affects its dynamic behaviour.*
- *A two stage model is presented for modelling steel laminated structures, which determines the contact parameters based on the pressure distribution between the laminae.*
- *Experimental modal analysis was used to validate the model.*

0 INTRODUCTION

In order to reduce Eddy currents and consequently heat losses, the magnetic cores in electrical devices are usually made of large number of thin metal sheets. These sheets are stacked together and are often line welded in order to preserve shape. The magnetostriction and magetic forces are a phenomena accompanying the magnetisation process and present a problem in terms of vibrations. The intensity of vibrations depends on the dynamic properties of the structure and the magnitude of the excitation phenomena. By optimizing the design of the laminated structure, the resonant frequencies can be avoided.

In order to predict the dynamic response of such structures a valid structural model must be developed, including an effective and reliable model of a contact-dependent structure, with friction between the laminae. Laminated structures are usually substantially more flexible than the equivalent homogeneous structures **[1]** and **[2]**, and exhibit orthotropic behavior and high levels of internal damping due to the interlaminar friction forces **[3]** and **[4]**. The numerical model of a laminated structure has to account for the pressure distribution between laminae, as it influences the stiffness distribution within the structure **[4]** to **[6]**. The authors of **[6]** observed a significant increase of the eigenfrequencies even for small increases of the pressure between the laminae. Some analytical models also exist for the estimation of modal parameters of a stator packet **[7]** and **[8]**; however, they fail to take the frictional contact between the laminae into account. An efficient contact model in the field of multibody dynamics was presented in **[9]**, which separates between the normal and tangential influences of contact parameters on a highly flexible body. Laminated structures are also commonly modelled using orthotropic material properties **[10]**, **[11]** and **[12]** that are obtained experimentally, by measuring a real structure and consequently updating the numerical model. Simplified models are used in order to reduce the complexity, number of components in the analysis, number of details and number of degrees of freedom. Many of these models were developed for the modelling of composite structures. These methods are commonly referred to as homogenisation methods **[12]**. Some of the methods employ

*Corr. Author's Address: University of Ljubljana, Faculty of Mechanical Engineering, Aškerčeva 6, 1000 Ljubljana, SI- Slovenia, gregor.cepon@fs.uni-lj.s

simplifying the laminated structure by determining equivalent homogeneous material properties **[13]** and **[14]**. A more sophisticated analytical solution was proposed in **[15]** for determining the laminated structure's equivalent elasticity matrix. The paper **[16]** describes the Reissner- Mindlin model for numerical homogenisation of orthotropic structures. A very thorough review of these homogenisation methods is presented in **[17]**.

Modelling of the structure using the orthotropic material properties is performed by modifying the shear and elastic moduli of the equivalent homogeneous structure. The obtained material parameters are applicable to the specific laminated structure and assume a uniform pressure distribution and friction forces between the lamina. Thus, each modification regarding the geometry, number of laminae, number and position of welds, etc. has to be evaluated experimentally and then the valid numerical model can be created. Moreover, the introduction of orthotropic material properties can also lead to the occurrence of additional unrealistic mode shapes **[4]**. The usage of orthotropic material properties in the case of cylindrically symmetric structures also means that the modes occur in pairs, at similar frequencies. This is, however, not necessarily the case when dealing with welded laminated structures, as shown in this paper using the extended linear contact model.

Just recently, the authors of **[4]** developed a new general numerical model of laminated structures that accounts for the non-uniform distribution of inter-laminar friction forces. This numerical model employs contact elements characterized by stiffness and damping parameters in a tangential contact direction and non-linear contact stiffness in the normal contact direction. The algorithm for modelling of a contact using beam elements made it possible to accurately predict the eigenfrequencies and mode shapes for various configurations of clamped laminated stacks. In this paper the model presented in **[4]** is extended in order to predict the modal parameters of welded electrical stator packages.

The originally proposed algorithm for modelling a contact-dependent structure in **[4]** was used to model simple cubic laminated stacks without welds. Here, the developed model is general and may be applicable to geometrically complex laminated structures, e.g., electrical stators. As the contact model was thoroughly tested in **[4]**, where the influence of stack height, surface treatment of the laminae and steel types were analysed on 18 different configurations of the packages. Therefore, only the influence of non-uniform contact pressure distribution is of interest in the experimental analysis in this paper.

Effect of welds is additionally introduced into the laminated structure model as the stators are commonly line welded to preserve stack geometry. The welds serve as a physical connection between laminae and due to residual stresses influence the inter laminar pressure distribution within stator packet. Residual stresses result in a force, that influence the frictional conditions between the laminae. Analytical methods to deduce the residual stresses usually follow the calculation of heat flow and thermal expansion **[18]**, where material properties are temperature dependent **[19]**. Some authors model the heat flow and thermal expansion through the continuous material using 3D **[20]** or simplified with 1D finite elements **[21]**.
Here the weld and the welding process itself was modeled by spring-thermo-elasto-plastic bar model **[22]**. To introduce the weld model into the laminated structures the formulation presented in **[22]** had to be additionally extended in order to enable the implementation of the model in a finite element environment. To validate the developed model of laminated structures several stator packets that differ in geometry, number of laminae and position of welds were experimentally analysed.

The article is organised as follows. The second section presents the development of the numerical model, its application to the complex geometry of a stator packet and the modelling of the welds. In third section, the experimental procedure is presented. The fourth section presents results and the validation of the model based on the three different stator packets.

1 NUMERICAL MODEL

Laminated structures are usually modelled using the orthotropic material properties, which implies that the shear and tension-compression modulus are independent. Here the contact description between two adjacent laminae is based on two stage linear contact model as it is presented in **[4]**. In the first stage the link elements are spanned between laminae and pressure distribution is deduced. In the second stage the link elements are replaced with beam elements (Fig. 1). A linear relation is assumed between the computed pressure distribution and the beam shear modulus G_f in order to model the effect of the friction forces and the sliding. In the first stage the lamina surface pressure distribution is computed using static analysis based on known clamping pressure. In this paper the first stage of the contact formulation is extended to account for the influence of the welding

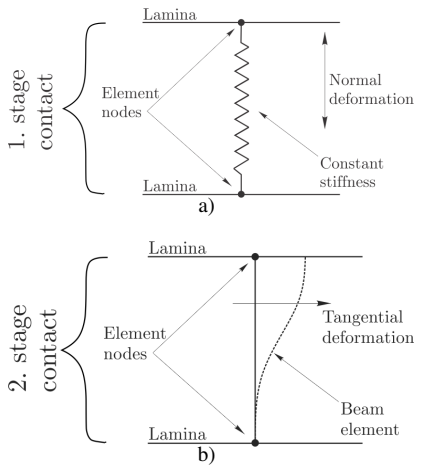

Fig. 1. *Linear contact model **[4]**; a) first stage, b) second stage*

process on the pressure distribution between laminae. The application of the proposed dynamic model of a contact using beam/link finite elements to the stator packet is presented in Fig. 2. Finite elements on the laminae are of different sizes and shapes. As the contact parameters are proportional to the size of a finite element, the geometry of each individual element had to be identified. This was not required in **[4]** as the authors applied the model only on simple geometry, which was meshed with an equally sized rectangular finite elements. The deformation pattern of applied beam finite elements used for modelling the contact conditions between the laminae consist of flexural, shear and axial deformations. Only the shear and compressional deformations are taken into account in the contact model. The shear deformation, that describes the frictional contact between laminae, is assumed to be linear. Linearisation enables the application of implicit methods in the framework of linear dynamics.

Beam finite elements were proposed to model the contact elements and shell elements to model the laminae. The beam elements had the cross-section area equivalent to the area of the corresponding shell elements on the adjacent laminae. The length of the beam elements was equal to the height of an individual lamina. It was observed that the material properties of the laminae influence mainly the in-plane modes of the structure, however the frictional contact parameters have the biggest influence on the out-of-plane modes. Compressional deformation is also allowed, and is used to determine pressure distribution between laminae in the first stage of the linear contact model.

1.1 Introduction of Welds into Laminated Structure Model

In this section the effect of welds on the dynamical behaviour of stator packet is identified and integrated in the linear contact model.

Before the welding process the stator packets were compressed with 2bar of pressure. The packets were line welded in several places along the circumference, Fig. 3. The number of welds varied depending on the type of the stator packet. Assuming near and far regions of the weld, the welding process can be modelled with a spring-thermo-elasto-plastic bar model **[22]**. A mathematical model for prediction of the residual stresses is presented in Fig. 4. The weld model is based on thermo-elasto-plastic bar, where A represents the cross section area of the weld, E the Youngs modulus and α as its coefficient of linear thermal expansion, (Fig. 4). The K_{eq} stands for the equivalent stiffness of the spring, that represents the part of the structure that is not affected by the heat treatment (welding process). Near regions of the weld are modelled using a thermo elasto plastic bar, which is subjected to deformations due to the clamping force and thermal expansion, during the welding process. Ideal elasto plastic material is proposed. As the far region is not in the heat affected region it can be represented as a spring, that deforms elastically during the clamping process.

The welding process is modelled in four stages: In the first stage, the packet is compressed with the axial force F. The compression results in a deformation u. The weld that is represented with thermo-elasto-plastic bar is then exposed to a temperature gradient ΔT, which heats the bar to its melting point. During the heating process the bar expands, thus the clamping force in the weld region reduces. It is assumed that the elastic modulus and the yield strength of the stack material reduces linearly with temperature **[22]**:

$$\sigma_y(T) = \sigma_0 \left(1 - \frac{T}{T_m}\right), \tag{1}$$

$$E(T) = E_0 \left(1 - \frac{T}{T_m}\right), \tag{2}$$

where E_0 and σ_0 represent the values of elastic modulus and yield stress at room temperature, T represents the temperature, which ranges from room to melting temperature, and T_m the melting temperature of the laminae material. The melting temperature of 1450 °C was proposed for all three stator packets. At melting temperature the stresses in the weld are equal to zero. In the third stage of the welding process the weld cools from the solidification to the surrounding

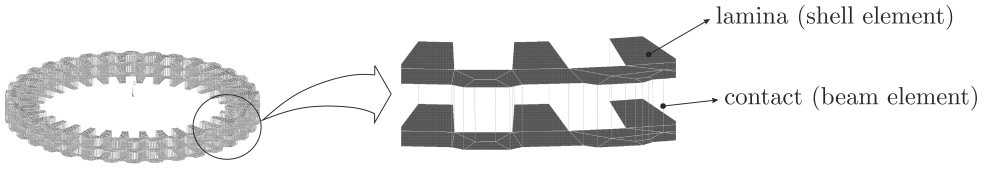

Fig. 2. *Shell elements (laminae) connected via frictional contact elements (beam)*

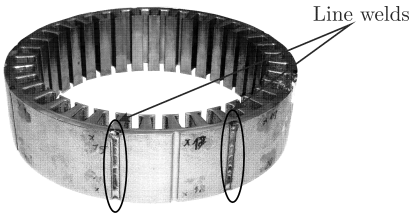

Fig. 3. *Line welds on the stator packet.*

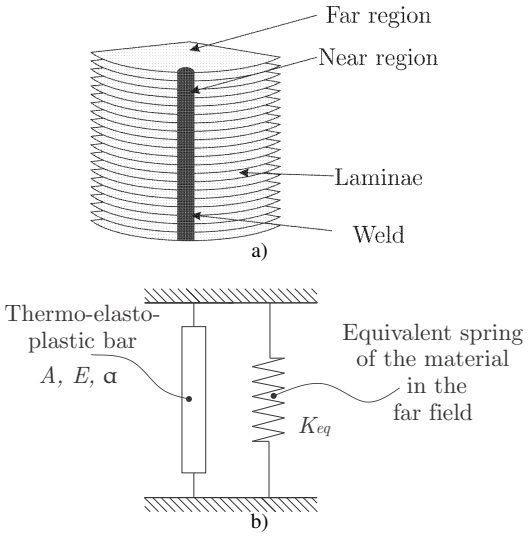

Fig. 4. *Modelling of the welded laminated structure; a) schematic representation of near and far field of the weld model, b) model of the weld for prediction of residual stresses*

temperature. The governing equation in the cooling phase can be written as:

$$\sigma = (\frac{k_{eq}}{h} + E)\,\varepsilon\,. \tag{3}$$

The k_{eq} represents the equivalent stiffness of the far region of the packet, h the height of the packet, E the Young modulus of the stator material and ε the deformation in the stator stacking direction. The equivalent stiffness of the far region of the packet k_{eq} can be obtained using the following equation:

$$k_{eq} = \frac{A\,E}{h}\,. \tag{4}$$

After the cooling process, the clamping force is removed, thus the spring modelling the far region expands and the axial load on the bar is applied. Stresses in the weld can be higher than the yield stress of the material. When the stresses reach the yield stress, the governing equation changes to

$$\sigma = \frac{k_{eq}}{h}\,\varepsilon + \sigma_0\,. \tag{5}$$

Considering the yield stress, it is possible to iteratively calculate the deformation of the weld itself. Resulting deformations can be applied to the nodes of the laminated structure, that represent the end points of the weld. Based on this deformations it is possible to deduce the pressure distribution in the stator packet due to the welding process (Fig. 5). The four stages of

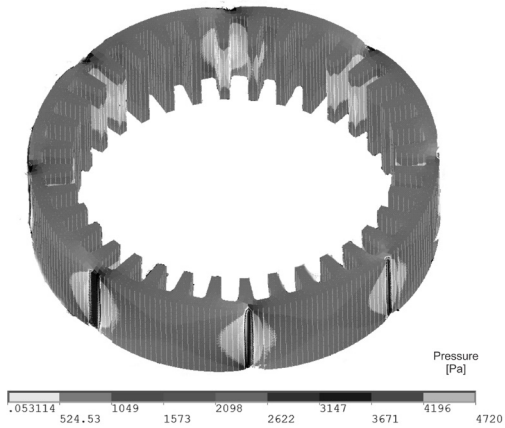

Fig. 5. *Pressure distribution between the laminae after the welding process*

the welding are schematically presented in Fig. 6.

2 VALIDATION OF THE DEVELOPED NUMERICAL MODEL

The developed numerical model was validated by comparison of numerically and experimentally obtained eigenfrequencies and modal shapes of three stator packets. Experimental modal analysis (EMA) was performed to obtain the eigenfrequencies and modal shapes for three different stator packets, that

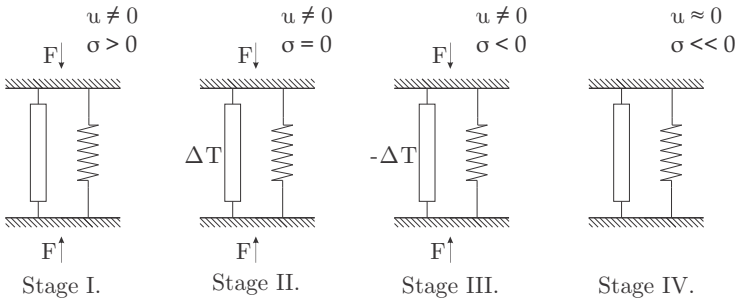

Fig. 6. *Modelling of the residual strains and stresses during welding*

are presented in the Table 1 and shown in Fig. 7. Experimentally obtained modal parameters were used to deduce the material parameters, as well as to validate the numerical model.

As the stator packets 1 and 2 had the same lamina geometry, it was possible to deduce the lamina material and contact parameters based on experimentally identified modal parameters of stator package 1. The identified parameters were then used to predict the eigen frequencies and mode shapes for the stator package 2. This enabled the validation of the developed numerical model of laminated structures with welds. The stator package 3 was included into the analysis to demonstrate the influence of asymmetrically distributed welds along the stator perimeter.

Table 1. *Stator packets under investigation*

Packet nr.	Diameter [mm]	Laminae nr.	Lamina thickness [mm]	Nr. of welds
1	140	70	0.5	8 (symmetric)
2	140	37	0.5	8 (symmetric)
3	108	55	0.5	7 (asymmetric)

2.1 Experimental Modal Analysis

In order to obtain the Accelerance (frequency response function), the system was excited with an electrodynamic shaker, with frequency range up to 6.4 kHz (Fig. 9). The excitation performed with the electrodynamic shaker was necessary due to the high levels of structural damping of the stator packets. The response of the system was measured with a rowing three axial accelerometer. The accelerometer was positioned on two bands around the circumference of each stator packet. The positions of the accelerometer can be seen in Fig. 8.

The stator packets exhibit distinct in-plane and out-of-plane modes. All modes occur in pairs and are shifted along the symmetry axis. The selected

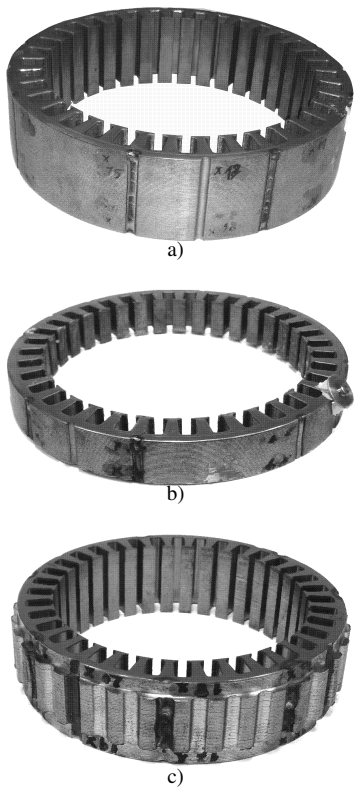

Fig. 7. *Stator packets under investigation; a) packet 1, b) packet 2, c) packet 3*

mode shapes are presented in Fig. 10. The measured eigenfrequencies are presented in the Tables 3 to 5 and are compared with the results of the numerical model.

2.2 Eigenfrequencies corresponding to In-Plane Modes

The eigenfrequencies of the in-plane modes are in direct correlation with the material parameters of the laminae. The in-plane modes namely have the same values of modal parameters regardless the number of laminae in the stator packet, contact parameter or the

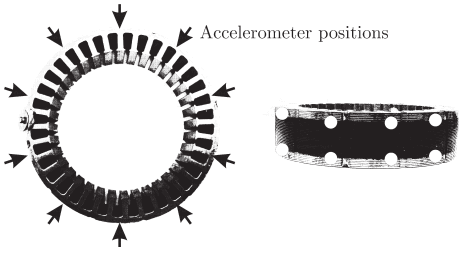

Fig. 8. *Accelerometer positions during EMA*

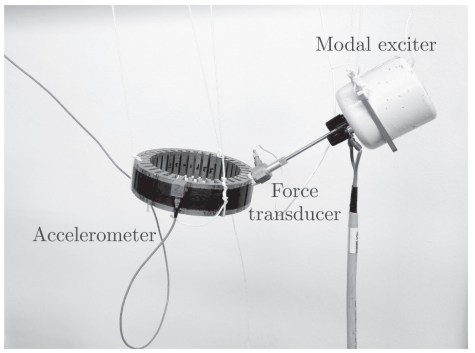

Fig. 9. *Experimental setup*

number and distribution of welds. Therefore it is possible to validate numerical model in the fist stage by comparing the eigenfrequencies corresponding to in-plane modes.

The value of elastic modulus was 206 GPa for all three laminae, and the density value of 7850 kg/m^3 was used. In Fig. 11 the comparison between experimentally and numerically obtained mode shape for first in-plane mode is presented. Based on error assessment it is evident that numerical model accurately predicts the value of the eigenfrequencies associated with in-plane modes.

2.3 Identification of Contact Parameters

The simulation procedure to deduce the contact parameters for given lamina and consequently modal parameters is presented in Fig. 12.

It is assumed in this paper that contact parameter G_f is independent of the pressure distribution within stator package and is not influenced by the number and position of welds. The contact parameter G_f is presumably a function of the frictional conditions between the two laminae. The contact parameter for stator packets 1 and 2 that were made from the same laminae, were obtained based on measurement of stator packet 1.

The identification of contact parameters relies on experimentally identified modal parameters that

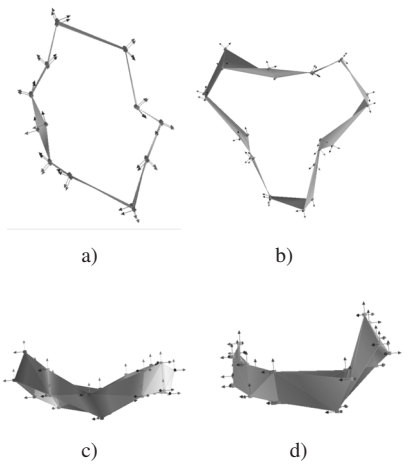

Fig. 10. *Mode shapes; a) 1st in-plane mode, b) 3rd in-plane mode, c) 1st out-of-plane mode, d) 2nd out-of-plane mode*

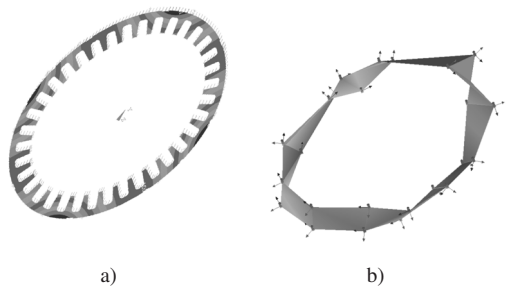

Fig. 11. *Third mode shape (1st in-plane mode) for stator packet 1; a) numerical model, a) EMA*

correspond to out-of-plane modes. The optimization function is defined as:

$$\mathrm{err}_G = \sqrt{\sum_i \left(f_{exp,i} - f_{num,i}(G_f)\right)^2}, \qquad (6)$$

where $f_{exp,i}$ is the i-th experimentally identified eigenfrequency and $f_{num,i}$ is the numerically identified eigenfrequency. In the process of calculating the contact parameter G_f only the eigenfrequencies corresponding to out-of-plane modes were used, Eq. (6). The algorithm to obtain contact parameter G_f is schematically presented in Fig. 12.

Based on the geometry of the stator packet the finite element model is generated. The packet is meshed and populated with link/beam elements. The cross section of each beam is calculated, based on the finite element mesh of the laminae. In the first contact stage all of the link elements have the same elastic modulus. By knowing clamping force and the number as well as the position of welds the pressure distribution between the laminae is calculated (Fig. 5). In the next step

the initial value for the material shear modulus G_f is selected. As the calculated nodal pressure between the laminae is non-uniformly distributed it is necessary to deduce the element shear modulus for each individual beam element:

$$G_{f,i}(p) = G_f \frac{p_{i,beam}}{p_{max}}, \tag{7}$$

where $p_{i,beam}$ is the nodal pressure at given node i and p_{max} is the max. value of identified nodal pressure within the lamina. The shear modulus $G_{f,i}(p)$ represents the friction forces by modeling beam shear deformation between two nodes on adjacent lamina. Based on the identified contact parameter the out-of plane modes are numerically predicted and the cost function err_G is estimated according to Eq. (6). If the cost function is not satisfied the optimization process is repeated with new value of contact parameter G_f. Using this procedure it is possible to deduce the contact parameter for the given type of lamina. Based on the

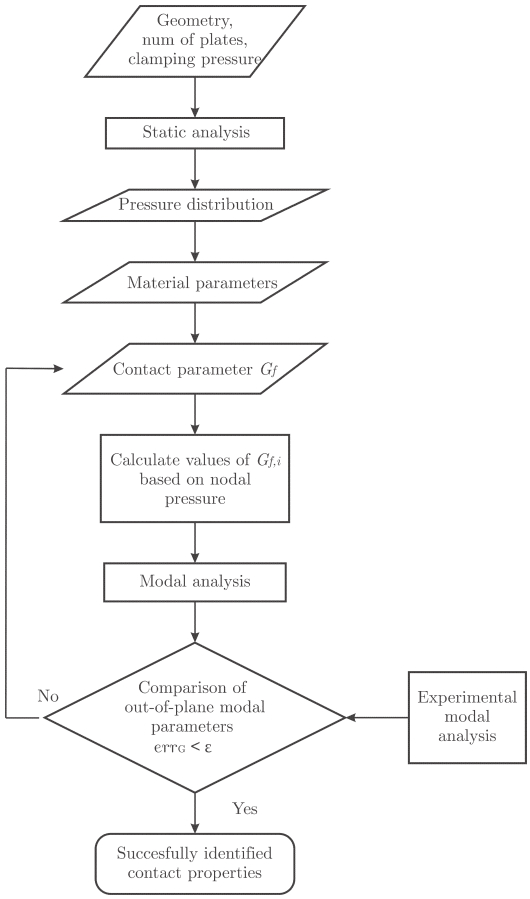

Fig. 12. *Simulation algorithm*

optimization algorithm presented in Fig. 12 the contact parameter G_f was identified for the stator package 1 and 3. The values are listed in Table 2. In this way it was possible to validate the developed numerical model of laminated structures with welds.

Table 2. *Identified contact parameter G_f*

Stator packet	Contact parameter G_f [GPa]
1, 2	0.3962
3	0.1744

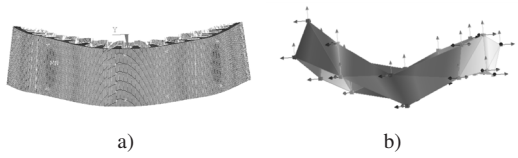

Fig. 13. *First mode shape (out of plane) for stator packet 1; a) numerical model, a) EMA*

Table 3. *Comparison of numerically and experimentally obtained eigenfrequencies for packet 1*

		Experiment	Numerical model	
Mode	Mode plane	Eigenfreq. [Hz]	Eigenfreq. [Hz]	Diff. [%]
1	out-of-plane	318.40	307.43	-3.45
2	out-of-plane	346.80	309.70	-11.98
3	in-plane	432.54	427.17	-1.24
4	in-plane	444.71	429.73	-3.37
5	out-of-plane	702.37	703.11	0.11
6	out-of-plane	892.97	837.03	-6.26

The experimentally obtained values were used as a reference to estimate the relative error of numerical model. It can be observed, that the difference between eigenfrequencies for the out-of-plane modes is not negligible. However the agreement can be considered satisfactory as the laminated structures are also subjected to great deal of uncertainties during the manufacturing process. The generality of proposed numerical model is demonstrated by accurately predicting the eigenfrequencies for the stator package 2. As the stator package 1 and 2 were made from the same type of lamina the contact parameter $G_f^{(1)}$ was obtained based on updating algorithm using stator package 1. Although the stator package 2 had different number of laminae and with this a different pressure distribution within stator package the numerical model correctly predicted the values of eigenfrequencies and corresponding modal shapes. Thus, once the contact parameter G_f is identified for given lamina it is possible to predict model parameters of stator packages that differ in geometry, clamping pressure and the number and position of welds.

Table 4. *Comparison of numerically and experimentally obtained eigenfrequencies for packet 2*

		Experiment	Numerical model	
Mode	Mode plane	Eigenfreq. [Hz]	Eigenfreq. [Hz]	Diff. [%]
1	out-of-plane	195.37	219.98	12.55
2	out-of-plane	262.35	212.13	-15.71
3	in-plane	425.22	423.14	-0.49
4	in-plane	447.39	425.53	-4.89
5	out-of-plane	637.35	656.88	3.06
6	out-of-plane	1045.29	969.13	-7.29

Table 5. *Comparison of numerically and experimentally obtained eigenfrequencies for packet 3*

		Experiment	Numerical model	
Mode	Mode plane	Eigenfreq. [Hz]	Eigenfreq. [Hz]	Diff. [%]
1	out-of-plane	342.95	342.83	-0.04
2	out-of-plane	456.75	443.85	-2.82
3	in-plane	572.57	590.49	3.13
4	in-plane	613.26	656.87	7.11
5	out-of-plane	690.16	678.13	-1.74
6	out-of-plane	820.00	764.73	-6.74

Moreover the proper modeling of the weld and the welding process itself can be demonstrated by observing eigenfrequencies of stator package 3. As the stator packets 1 and 2 have symmetrically distributed welds around the perimeter the first and the second mode shapes appear in pairs and shifted along the symmetry axis. It can be observed that first two eigenfrequencies are located closely together (Table 3). However this is not the case for the stator package 3 (Table 5), as the experimentally obtained first and second eigenfrequencies are placed distinctly apart. This is the result of unsymmetrically distributed welds along the perimeter of the stack, and the developed numerical model successfully predicted this behaviour.

3 CONCLUSION

In this paper a numerical model of laminated structures is presented in order to predict the eigenfrequencies and modal shapes of laminated stator packages. The model uses shell and link/beam finite elements to model the contact conditions between the laminae that expedite the computation time of the modal analysis, thus practically justifying the modelling of each individual plate in the stator package. The welds and the welding process are represented using spring-thermo elasto-plastic bar model. In order to identify contact parameters and to validate the numerical model three different stator packages were analyzed. The experimentally identified eigenfrequencies and corresponding mode shapes were used in the optimization process to extract the values of contact parameters.

It has been shown that the in-plane modes are in direct correlation with material properties of the lamina. The out-of-plane modes are however governed by the value of contact parameters. The generality of proposed numerical model is demonstrated with the stator package 2 where the contact parameters were identified based on stator package 1. Although the stator package 2 had different number of laminae comparing to to stator package 1 the numerical model correctly predicted the values of eigenfrequencies and corresponding modal shapes.

Moreover the proper modeling of the weld and the welding process itself is demonstrated on the stator package 3. In this case the experimentally obtained first and second eigenfrequencies are located distinctly apart which is the result of unsymmetrically distributed welds along the perimeter of the stack. In order to successfully predict this behaviour it is necessary to model the physical connection at the weld location as well as the influence of the welding process on the pressure distribution within the stator package.

4 ACKNOWLEDGEMENTS

The authors acknowledge the partial financial support from the research project EVA4Green.

5 REFERENCES

[1] Garvey, S.D. (1989) The vibrational behaviour of laminated components in electrical machines. 4th International Conference on Electrical Machines and Drives, p. 226-231.

[2] Wang, H., Williams, K. (1997). Effects of laminations on the vibrational behaviour of electrical machine stators. *Journal of Sound and Vibration*, vol. 202, no. 5, p. 703-715, **DOI:10.1006/jsvi.1996.0845**.

[3] Popp, K., Panning, L., Sextro, W. (2003). Vibration damping by friction forces: theory and applications. *Modal Analysis*, vol. 9, no. 3-4, p. 419–448, **DOI:10.1177/107754603030780**.

[4] Pirnat, M., Čepon, G., Boltežar, M. (2013). Introduction of the linear contact model in the dynamic model of laminated structure dynamics: An experimental and numerical identification. *Mechanism and Machine Theory*, vol. 64, p. 144–154, **DOI:10.1016/j.mechmachtheory.2013.02.003**.

[5] Javorski, M., Čepon, G., Slavič, J., Boltežar, M. (2013). A generalized magnetostrictive-forces approach to the computation of the magnetostriction-induced vibration of laminated steel structures. *IEEE Transactions on Magnetics*, vol. 49, no. 11, p. 5446–5453, **DOI:10.1109/TMAG.2013.2269316**.

[6] Kim, Y.C., Kim, K.W. (2006). Influence of lamination pressure upon the stiffness of laminated rotor. *JSME International Journal Series C Mechanical Systems, Machine Elements*

and Manufacturing, vol. 49, no. 2, p. 426–431, **DOI:10.1299/jsmec.49.426**.

[7] Singal, R.K., Williams, K., Verma, S.P. (1987). Vibration behaviour of stators of electrical machines, part II: Experimental study. *Journal of Sound and Vibration*, vol. 115, no. 1, p. 13-23, **DOI:10.1016/0022-460X(87)90489-5**.

[8] Verma, S.P., Singal, R.K., Williams, K. (1987). Vibration behaviour of stators of electrical machines, part I: Theoretical study. *Journal of Sound and Vibration*, vol. 115, no. 1, p. 1–12, **DOI:10.1016/0022-460X(87)90488-3**.

[9] Calì, M., Oliveri, S.M., Sequenzia, G., Fatuzzo, G. (2017). An effective model for the sliding contact forces in a multibody environment. *Advances on Mechanics, Design Engineering and Manufacturing*, p. 675-685. Springer, Cham, **DOI:10.1007/978-3-319-45781-9_68**.

[10] Wang, C., Lai, J.C.S., Astfalck, A. (2004). Sound power radiated from an inverter driven induction motor II: Numerical analysis. *IEE Proceedings - Electric Power Applications*, vol. 151, o. 3, p. 341-348, **DOI:10.1049/ip-epa:20040120**.

[11] Van der Giet, M., Kasper, K., De Doncker, R.W., Hameyer, K. (2012). Material parameters for the structural dynamic simulation of electrical machines. *XXth International Conference on Electrical Machines*, p. 2994-3000, **DOI:10.1109/ICElMach.2012.6350314**.

[12] Millithaler, P., Sadoulet-Reboul, É., Ouisse, M., É. Dupont, J.-B., Bouhaddi, N. (2015). Structural dynamics of electric machine stators: Modelling guidelines and identification of three-dimensional equivalent material properties for multi-layered orthotropic laminates. *Journal of Sound and Vibration*, vol. 348, p. 185-205, **DOI:10.1016/j.jsv.2015.03.010**.

[13] Berthelot, J.M. (2012). *Composite Materials: Mechanical Behavior and Structural Analysis*. Springer -Verlag, New York, **DOI:10.1007/978-1-4612-0527-2**.

[14] Reddy, J.N. (2003). Mechanics of Laminated Composite Plates and Shells: Theory and Analysis, CRC Press, Boca Raton.

[15] Begis, D., Bestagno, A., Duvaut, G., Hassim, A., Nuc. M. (1983). *A New Method of Computing Global Elastic Moduli for Composite Materials*. PhD thesis, INRIA, Le Chesnay Cedex.

[16] Cecchi, A., Sab, K. (2007). A homogenized reissner–mindlin model for orthotropic periodic plates: Application to brickwork panels. *International Journal of Solids and Structures*, vol. 44, no. 18-19, p. 6055-6079, **DOI:10.1016/j.ijsolstr.2007.02.009**.

[17] Kalamkarov, A.L., Andrianov, I.V., Danishevs'kyy, V.V. (2009). Asymptotic homogenization of composite materials and structures. *Applied Mechanics Reviews*, vol. 62, no. 3, p. 030802, **DOI:10.1115/1.3090830**.

[18] Rogante, M., Cesari, F.G., Ferrari, G. (2009). Analytical method for residual stresses determination in thin welded joints. *Multidiscipline Modeling in Materials and Structures*, vol. 5, no. 3, p. 269-276, **DOI:10.1163/157361109789016998**.

[19] Teng, T.L., Lin, C.C. (1998). Effect of welding conditions on residual stresses due to butt welds. *International Journal of Pressure Vessels and Piping*, vol. 75, no. 12, p. 857-864, **DOI:10.1016/S0308-0161(98)00084-2**.

[20] Deng, D., Murakawa, H. (2006). Numerical simulation of temperature field and residual stress in multi-pass welds in stainless steel pipe and comparison with experimental measurements. *Computational Materials Science*, vol. 37, no. 3, p. 269-277, **DOI:10.1016/j.commatsci.2005.07.007**.

[21] Salvini, P., Vivio, F., Vullo, V. (2000). A spot weld finite element for structural modelling. *International Journal of Fatigue*, vol. 22, no. 8, p, 645-656, **DOI:10.1016/S0142-1123(00)00044-X**.

[22] Mandal, N.R., Sundar, C.V.N. (1997). Analysis of welding shrinkage. *Welding Journal, Welding Research Supplement*, vol. 76, no. 6, p. 233-238.

Strojniški vestnik - Journal of Mechanical Engineering 64(2018)2, 82-94

DOI:10.5545/sv-jme.2017.4534 Original Scientific Paper
Received for review: 2017-04-25
Received revised form: 2017-07-15
Accepted for publication: 2017-08-24

Effects of Joint Clearance on the Motion Accuracy of Robotic Manipulators

Selçuk Erkaya*
Erciyes University, Engineering Faculty, Mechatronics Engineering Department, Turkey

Accuracy is one of the key features that improves the quality of robotic manipulators for many industrial and medical applications. Even with an accurate design and manufacturing process, clearance problems in joints cannot be eliminated in articulated systems. This leads to a loss of accuracy in robotic manipulation. In this study, the effects of joint clearance in a robotic system are investigated. The need for the trajectory of end effector is considered to analyse the motion sensitivity. The kinematics and dynamics of a six-DOF robot with joint clearance are evaluated relative to a robot without joint clearance. Different scenarios for clearance values and working periods are performed to fulfil the required motion task. A neural model is also used to predict the trajectory deviations during the working process. The results show that clearance has a significant role in the motion sensitivity of robotic manipulations. Trajectory errors can also be determined by using a dynamic neural predictor with suitable input variables.

Keywords: Trajectory error, joint clearance, NARX model, 3D motion accuracy, uncertainty

Highlights

- *Accuracy is one of the key features in robotic manipulations.*
- *Clearance in a joint is inevitable and worsens the system performance.*
- *Joint clearance effects in robotic systems are analysed for end effector trajectory.*
- *Kinematic and dynamic outputs are compared for different working scenarios.*
- *A neural model is proposed to predict the trajectory deviations in robotic systems.*

0 INTRODUCTION

Robots have been introduced in many industrial and medical areas where high accuracy, repeatability, and operation stability are desired. These are key features for robots. Some error sources in robots originate from assemblage, servo actuator resolution, reducer backlash, and joint clearances [1]. These errors reduce the accuracy of the robot and must be controlled to ensure the quality of the desired movement. In this regard, increased importance has been given to the accuracy of robots through various contributions in the relevant literature [2] to [5]. In comparison to machine tools, industrial robots are flexible and relatively cheaper in terms of cost. At the same time, such robots are susceptible to errors from many sources due to their serial structure. To ensure the positioning accuracy of a robot end effector as well as to reduce the manufacturing cost of the robot, it is necessary to quantify the influence of the uncertain factors and optimally allocate the tolerances.

A novel and simple approach to identify the positional and directional errors due to the joint clearance of linkages and manipulators based on a geometrical model was introduced [6]. A general probability density function of the endpoint of planar robots with joint clearance was established to derive the distribution functions for any position tolerance zone and any joint distribution type [7]. Some errors arising from link stiffness and clearances were considered to predict the accuracy of the parallel devices [8]. By considering the positional and directional errors of the robot hand and the manufacturing cost, the optimal allocation of joint tolerances was investigated. Interval analysis was used to predict the errors in the manipulator performance [9]. Singularity analysis and modelling of the joint clearance effects on the parallel robot's accuracy were conducted. An analytical model was presented to easily predict the pose error for a given external load, a nominal pose and the structural parameters [3]. A procedure to calculate the positional error in parallel manipulators due to both clearances and elastic deformations was proposed [10]. For analysing the location of the discontinuities, a methodology was presented and the advantages of approach were analysed using a 5R planar mechanism [11]. The effect of joint flexibility on the dynamic performance of a serial spatial robot arm with rigid links was studied by using three developed models [12]. A novel method based on trajectory planning to avoid detachment of the joint elements of a manipulator with clearances was presented. An improved detachment criterion for the different joint types was proposed [13]. The clearance effects on an industrial robot were studied during 2D welding operations. The kinematics and

*Corr. Author's Address: Erciyes University, Engineering Faculty, Mechatronics Engineering Department, 38039 Kayseri, Turkey, erkayaselcuk@gmail.com

dynamics of robots were investigated for different clearance sizes [14]. The kinematic sensitivity of a robotic system with joint clearances was studied and tested for the effectiveness of the proposed model [15]. A methodology to analyse the assembly conditions and compute the maximum pose errors of parallel manipulators was presented by considering geometric errors, joint clearances, link flexibility, and joint elasticity [1]. A space robot manipulator system was considered to analyse the joint clearance effects. A computational methodology based on the nonlinear equivalent spring-damper and Coulomb friction models was proposed [16]. The effect of joint error on the positional accuracy of a robotic manipulator was presented. A serial chain two-revolute joint planar manipulator was modelled. Under the influence of the joint clearance, a formulation was presented to analyse the positional accuracy of the end effector [17]. A spherical parallel manipulator with clearance and manufacturing error was analysed to determine the pose error of the platform in the presence of these imperfections [18]. The trajectory of a walking mechanism in a mobile robot with joint clearance was studied. A neural-fuzzy model and genetic algorithm approaches were designed to improve the system performance [19]. The effects of joint clearance, link flexibility and lubrication on the kinematics and dynamics of mechanisms were extensively performed with analytical and numerical studies [20] to [22]. For improving the mechanism precision, optimization methods were also introduced to decrease the deviations owing to the clearance joint [23] to [25]. Artificial neural networks were used to evaluate the vibration characteristics of a mechanism with or without joint clearance [26] and [27]. Both theoretical and experimental studies about joint clearance were presented [28]. The effects of joint clearances on the kinematics and dynamics of planar and spatial mechanisms with rigid and elastic links were also investigated [29] to [35]. Dry contact including the friction and lubrication effects between journal and bearing parts, different sizes of clearances and joint types were investigated in many case studies. A general and comprehensive approach was proposed to automatically adjust the time step to simplify and increase the computational ability in multibody systems. 2D and 3D partly compliant mechanisms having joint clearance were studied to show the positive effects of flexural pivot on the undesired effects of joint clearance [36] and [37]. A general computer-aided model of a 3D revolute clearance joint in multibody dynamic solvers was presented [38]. A new technique for assessing the influence that the clearance of spatial revolute joints has on the kinematics and dynamics of multibody systems was presented [39]. Examination and comparison of several friction force models dealing with different friction phenomena in the context of multibody system dynamics were presented [40] and [41]. A comparative study on the most relevant existing viscoelastic contact force models was studied [42]. A critical review was presented about the existing knowledge on the computational model of normal directional impact on rigid bodies [43].

It is clear that even with an accurate design and manufacturing process for the whole system, it is not completely possible to eliminate the clearance problem in joints. In this study, motion insensitivities arising mainly from joint clearance on a robot manipulator, which can be used for laser cutting, welding, medical applications, etc., were considered. Both the trajectory of the end effector as a kinematic characteristic and necessary force/torque as a dynamic characteristic were investigated. A dynamic neural model is proposed to predict the trajectory deviations arising from joint clearance. It is possible to evaluate the end effector deviations from the desired trajectory. The outputs of this study can be used to obtain the necessary control outputs for improving the motion sensitivity by a robust controller design. This paper is organized as follows. The mathematical model of the clearance joint and motion equation of the robot manipulator are outlined in Section 1. The basic theory of the neural predictor is given in Section 2. The obtained results and conclusions are summarized in Sections 3 and 4, respectively.

1 MODELLING OF JOINT CLEARANCE, CONTACT FORCE, AND MOTION EQUATION

Clearance can be considered to be an imperfect joint characteristic. It is inevitable, due primarily to manufacturing errors, assemblage, and wear. In fact, a suitable value of clearance in the joint parts is essential to allow the relative motion of the adjacent links. In the presence of joint clearance, different motion types between the joint parts can be observed, that is, free-flight, impact, and continuous contact modes. These motion types fully affect the kinematic and dynamic performances of the systems. During the current trajectory, it is seen that the clearance joint exhibits nearly a similar characteristic of a 2D planar revolute joint with clearance. Due to computational efficiency, neural predictor characteristics and the robust controller design for the next studies, this negligible 3D effect of this joint is not considered. As

given in the literature [23] and [29], radial clearance in a joint can be defined as the difference between the journal and bearing radii (Fig. 1).

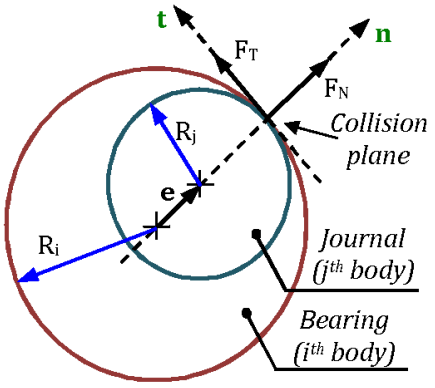

Fig. 1. *Contact forces at the collision plane*

The bearing and journal are parts of the i^{th} and j^{th} bodies, respectively. The relative penetration depth (δ) between the journal and bearing is outlined as [29] and [34]:

$$\delta = e - c, \tag{1}$$

in which e is the magnitude of the clearance vector between the bearing and journal centres, and c is the radial clearance. In a clearance joint, the force is explained by two different situations. The first one is no contact forces ($\mathbf{F_C}$) if the joint parts are not in contact. Otherwise, there is a contact between joint parts, and the contact-impact forces are modelled according to a nonlinear dissipative force model based on the Hertzian contact theory (normal force, F_N) and Coulomb's friction law (tangential force, $\mathbf{F_T}$). These two conditions can be given as [29]:

$$\begin{aligned} \mathbf{F_C} &= 0 && \text{if} && \delta < 0, \\ \mathbf{F_C} &= F_N + \mathbf{F_T} && \text{if} && \delta \geq 0, \end{aligned} \tag{2}$$

when the magnitude of the clearance vector is greater than radial clearance, an impact occurs, and the penetration depth is calculated using Eq. (1). The contact force is modelled as a spring-damper element. If this element is linear, the approach is known as the Kelvin-Voigt model. When the relation is nonlinear, the model is generally based on the Hertz contact law [29] and [44]. In the case of an unlubricated joint, the Hertzian contact force model is an appropriate choice [44]. While the original Hertzian model does not include any energy dissipation, an extension by Lankarani and Nikravesh includes energy loss due to internal damping. The contact force model is key to describing the collision dynamics between the journal and bearing in a clearance joint [45] and [46]. Due primarily to the simplicity of its contact force model, applicability to impact in multibody systems, easy calculation, and fast convergence (inclusion of energy dissipation modelling upon impact), the model developed by Lankarani and Nikravesh [47] is widely used in the dynamics of multibody systems with joint clearance. The normal force is expressed as [29]:

$$F_N = K\delta^{(3/2)} + D\dot{\delta}, \tag{3}$$

where the first term represents the elastic force component and the second term explains the energy dissipation. K is the generalized stiffness parameter and D is the hysteresis damping coefficient. K depends on the geometry and physical properties of the contacting surfaces and is defined by [29]:

$$K = \frac{4\left(E_i E_j\right)}{3\left(E_j\left(1-\nu_i^2\right)+E_i\left(1-\nu_j^2\right)\right)}\left(\frac{R_i R_j}{R_i - R_j}\right)^{1/2}, \tag{4}$$

ν and E are Poisson's coefficient and Young's modulus associated with journal and bearing parts. The hysteresis damping coefficient is outlined as [29]:

$$D = \left[3\left(1-\zeta^2\right)K\delta^{3/2}\right] / 4v_0, \tag{5}$$

where ζ is the restitution coefficient, and v_0 is the initial impact velocity. Friction is a complex phenomenon that comprises the interaction between the surfaces of contacting bodies and may lead to different friction regimes, such as sliding and sticking. Generally, Coulomb's friction model is used to represent the friction response in impact and contact process. However, the definition of Coulomb's friction law poses numerical difficulties when the relative tangential velocity is near zero. In the current study, a modified Coulomb friction model is used to represent the friction behaviour between the journal and bearing [29] and [48].

$$\mathbf{F_T} = -\mu\left(\upsilon_T\right)F_N\left(\boldsymbol{\upsilon}_T / \left|\upsilon_T\right|\right), \tag{6}$$

where $\mu(\upsilon_T)$ is the coefficient of friction. It is a function of relative sliding velocity (υ_T) in the collision point of journal and bearing, which is the velocity component in the tangential direction $\mu(\upsilon_T)$, which is not a constant, is introduced in the modified Coulomb friction model. $\mu(\upsilon_T)$ is a function of the tangential sliding velocity, which can represent the friction behaviour in impact and contact process as well as the viscous and micro-slip phenomenon in relative low-velocity cases more accurately. Furthermore, the modified Coulomb friction model can avoid the case of abrupt change of friction in the numerical calculation as the change

$$\mu(\upsilon_T)=\begin{cases}-\mu_{\mathrm{d}}sign(\upsilon_t) & for\ |\upsilon_t|>\upsilon_d \\ -\left\{\mu_{\mathrm{d}}+(\mu_{\mathrm{s}}-\mu_{\mathrm{d}})\left(\dfrac{|\upsilon_t|-\upsilon_s}{\upsilon_d-\upsilon_s}\right)^2\left[3-2\left(\dfrac{|\upsilon_t|-\upsilon_s}{\upsilon_d-\upsilon_s}\right)\right]\right\}sign(\upsilon_t) & for\ \upsilon_s\le|\upsilon_t|\le\upsilon_d, \\ \mu_{\mathrm{s}}-2\mu_{\mathrm{s}}\left(\dfrac{\upsilon_t+\upsilon_s}{2\upsilon_s}\right)^2\left(3-\dfrac{\upsilon_t+\upsilon_s}{\upsilon_s}\right) & for\ |\upsilon_t|<\upsilon_s\end{cases} \quad (7)$$

of velocity direction [29] and [48]. $\mu(\upsilon_T)$ is defined as Eq. (7), where μ_s and μ_d are the static and dynamic friction coefficients, respectively. υ_s and υ_d denote the critical velocities of the static and maximum dynamic frictions, respectively. Fig. 2 shows how the dynamic friction coefficient varies with slip velocity [41] and [48].

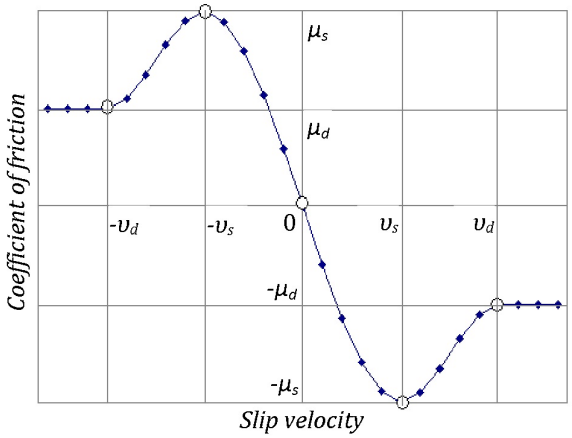

Fig. 2. *Friction coefficient and slip velocity*

A six-axis industrial robot was considered for the theoretical analysis. This robot is mainly used for laser cutting, welding, handling, assembly etc. The robot manipulator has six degrees of freedom when all joints are perfect, as shown in Fig. 3. Different sizes of artificial clearance and working period were used to investigate the effects of joint clearance on the motion accuracy of the robot manipulator. Joint clearance leads to different motion modes such as free-flight, impact and continuous contact. Therefore, a dynamic model of the robot manipulator considering joint clearance must be developed. In case of free-flight mode, the dynamic equation for the robot manipulator is given as follows,

$$\mathbf{M}(q(t))\ddot{\mathbf{q}}(t)+\mathbf{C}(q(t),\dot{q}(t))\dot{\mathbf{q}}(t)+...$$
$$...+\mathbf{Q}(\dot{q}(t))+\mathbf{G}(q(t))=\mathbf{F}(t), \quad (8)$$

where $\mathbf{q}$ is the generalized coordinate column matrix. $\mathbf{M}(q(t))$ denotes the inertia matrix of the robot manipulator. $\mathbf{C}(q(t),\dot{q}(t))$ is the vector of centrifugal and coriolis terms. $\mathbf{Q}(\dot{q}(t))$ represents the friction term, which consists of the viscous and dynamic

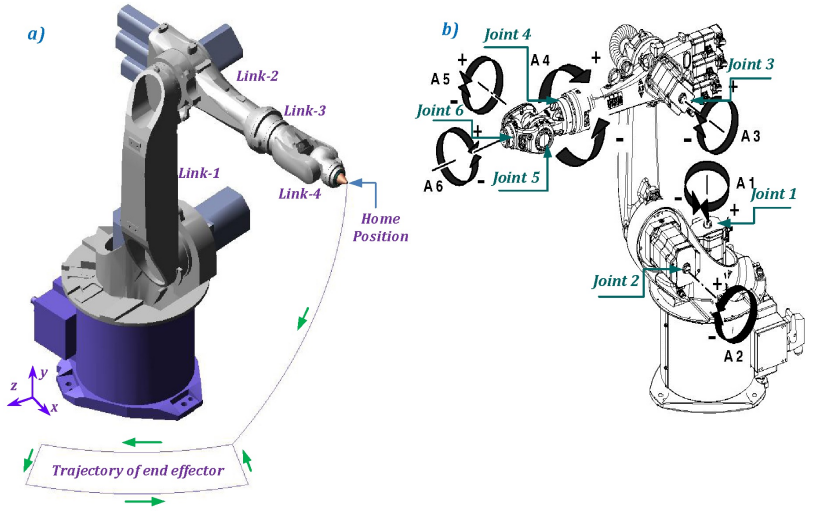

Fig. 3. *Robot manipulator: a) trajectory of end effector, b) motion capability*

frictions. $\mathbf{G}(q(t))$ and $\mathbf{F}(t)$ denote the vector of gravity term and the generalized force matrix, respectively.

In case of impact and continuous contact modes, contact force takes places between the journal and bearing in the joint. Therefore, the dynamic equation is outlined as:

$$\mathbf{M}\left(q(t)\right)\ddot{\mathbf{q}}(\mathrm{t})+\mathbf{C}\left(q(t),\dot{q}(t)\right)\dot{\mathbf{q}}(\mathrm{t})+\mathbf{Q}\left(\dot{q}(t)\right)+... \\ ...+\mathbf{G}\left(q(t)\right)=\mathbf{F}(\mathrm{t})+\mathbf{F}_{\mathbf{C}}\left(\delta,\dot{\delta}\right), \quad (9)$$

where $\mathbf{F}_{\mathbf{c}}\left(\delta,\dot{\delta}\right)$ is the contact force that comprises the normal and tangential components. One of the most important and complex parts of the simulation of multibody systems comprising the contact-impact analysis procedure is the detection of the precise instant of impact. In addition, the model used to characterize the contact between the bodies requires the knowledge of the pre-impact conditions, that is, the impact velocity and the direction of the normal to the colliding surface. Neither the contact duration nor the penetration can be predicted from the pre-impact conditions due to the influence of the kinematic constraints and other interactions on the bodies of the complete system [35]. The characteristics of the robot manipulator are outlined in Table 1. The dynamic simulation parameters of the robot manipulator with joint clearance are outlined in Table 2.

Table 1. *Characteristics of robot manipulator*

Robot Links	Length [mm]	Mass [kg]	Mass moment of inertia characteristics [kgm^2]					
			J_{xx}	J_{yy}	J_{zz}	J_{xy}	J_{yz}	J_{zx}
Link 1	680	74.08	3.26	0.32	3.25	1.84 10^{-3}	0.145	-1.32×10^{-3}
Link 2	402	43.51	0.336	1.407	1.362	-5.28×10^{-3}	-7.46×10^{-3}	9.78×10^{-3}
Link 3	268	7.87	1.83×10^{-2}	6.46×10^{-2}	5.89×10^{-2}	1.83×10^{-5}	4.02×10^{-6}	3.68×10^{-3}
Link 4	115	2.22	2.09×10^{-3}	4.9×10^{-3}	4.86×10^{-3}	7.61×10^{-10}	1.13×10^{-9}	5.56×10^{-4}

Table 2. *Simulation parameters of robot manipulator*

Description	Value	Description	Value
Dynamic friction coefficient	0.01	Young's modulus	71.7 GPa
Restitution coefficient	0.9	Integration step size	1×10^{-3} s
Poisson's coefficient	0.33	Integration tolerance	1×10^{-5}

2 NONLINEAR AUTOGRESSIVE EXOGENOUS (NARX) MODEL

Neural network applications have rapidly expanded over the last two decades owing to the advances in computer science and sensor technologies [49]. In case of system identifications using neural networks, the main purpose is usually to define a dynamically valid model that can be used for system analysis [26]. The NARX is used for modelling nonlinear dynamical systems [50]. It is one of the artificial neural network models for time series prediction. It learns the behaviour of a system in a more effective way than other neural networks do (i.e., the learning gradient algorithm is better in NARX) and converges much faster and generalizes better than other networks [51] and [52]. It has been demonstrated that it can predict the behaviours of nonlinear dynamics systems and is particularly useful for time series modelling [53] and [54]. The structure of the NARX model is similar to the traditional multi-layered perceptron (MLP) model. Among the various Artificial Neural Network (ANN) models, the MLP model is one of the most widely used for prediction due primarily to its simple and flexible nature. Both the MLP and the NARX models consist of an input, a hidden layer, and an output layer. In addition, the NARX model feeds the time history of the output signal to the input layer as part of the inputs. The current input signal together with its time history acts as the other part of the inputs to the model. The number of output neurons is equal to the number of output variables of the problem to be solved. The number of hidden neurons is determined by the user. Assume Γ is the function of the NARX model. It correlates the input time series $\{u_t\}_{t=0}^{T}$ and the output time series $\{y_t\}_{t=0}^{T}$ by the Eq. (10).

$$y_t=\Gamma\left(y_{t-1},y_{t-2},...,y_{t-\tau_y},u_t,u_{t-1},...,u_{t-\tau_u}\right), \quad (10)$$

where u_t and y_t denote the input and output of the network at time t, the function Γ is a nonlinear function, and τ_y and τ_u are the time lags for the input and output series, respectively. Fig. 4 gives the general architecture of the NARX model.

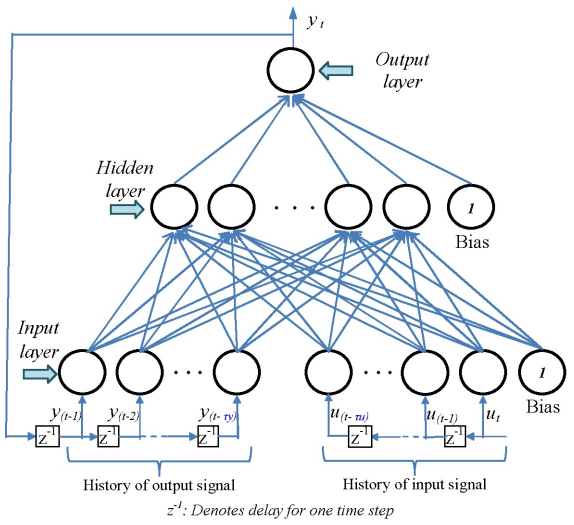

Fig. 4. *Architecture of the NARX model*

In this study, the deviations of the end effector are considered as the output of the NARX model. The inputs of the NARX model consist of the time histories of the necessary torques and path components, specifications of the joint with clearance (clearance value, number of joints with clearance, and the location of joint with clearance). Each neuron has a bias input. Input and output layers have the linear activation functions. The sigmoid function is also used in four hidden layers with ten neurons. In this study, the Levenberg-Marquardt algorithm is adopted for the learning process due to its fast convergence properties [55]. The performance index used in NARX model training is the mean squared error (MSE), which is one of the typical performance functions. The NARX model was trained using the Neural Network Toolbox of MATLAB [50]. For training, validation and testing purposes, the complete procedure performs the data during three steps. The training step is used to adjust NARX weights. The validation step is used for selecting the model variant. The last step is testing. It is used to evaluate the chosen model against unknown data. In this work, 1500 and 750 data are used for 12 and 6 second working periods, respectively. Of all data, 50 % were used in training; 20 % and 30 % of all data were used for validation and testing, respectively. It is seen from the simulation; these data numbers are adequate for designing a stable neural model.

3 RESULTS

A theoretical study was implemented to analyse the motion accuracy of robot manipulators with joint clearance. Exaggerated clearance values as an imperfect joint characteristic were adjusted in a reference joint (joint 5) as 0.2 mm, 0.4 mm and 0.6 mm for three case studies and comparisons. The working periods were considered as 6 and 12 seconds. The robot manipulator has six degrees of freedom when all joints are ideal or perfect. By using suitable input variables, a dynamic neural network was used

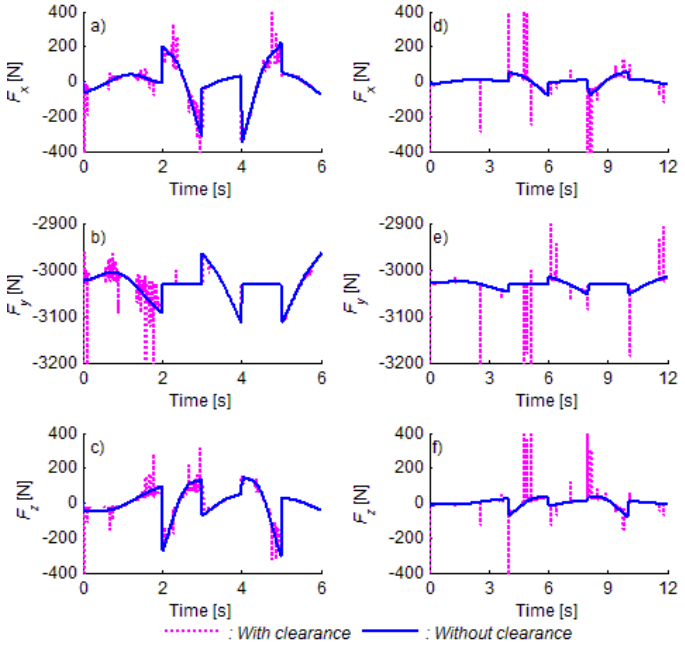

Fig. 5. *Forces for 0.2 mm clearance: a), b) and c) working for 6 seconds, d), e) and f) working for 12 seconds*

for predicting the clearance-induced deviations in the robot trajectory. In case of perfect, imperfect joint characteristics and neural modelling, all simulations were performed using a Pentium Core 2 Quad Q6600 computer. At the beginning of the manipulator motion, it was considered that the journal centre coincides with the bearing centre. To show the clear effects of joint clearance, the force components of joint 1 are considered. Figs. 5 to 7 give the force components of joint 1 for different scenarios. The same scales are used for easy comparison and evaluation of the force components. However, the maximum values of some peaks are beyond those used scales. As shown in the figures, the robot manipulator has greater force variation in a short working period [14]. The existence of joint clearance causes impulse-type contact forces.

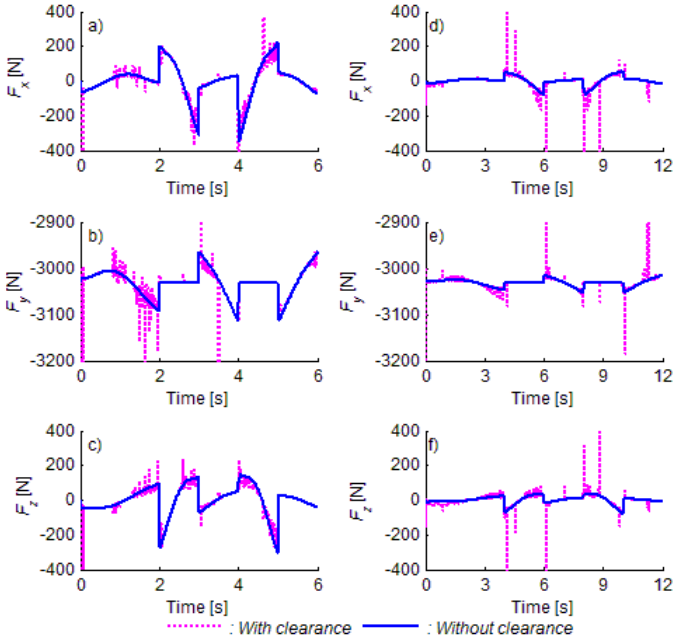

Fig. 6. *Forces for 0.4 mm clearance: a), b) and c) working for 6 seconds, d), e) and f) working for 12 seconds*

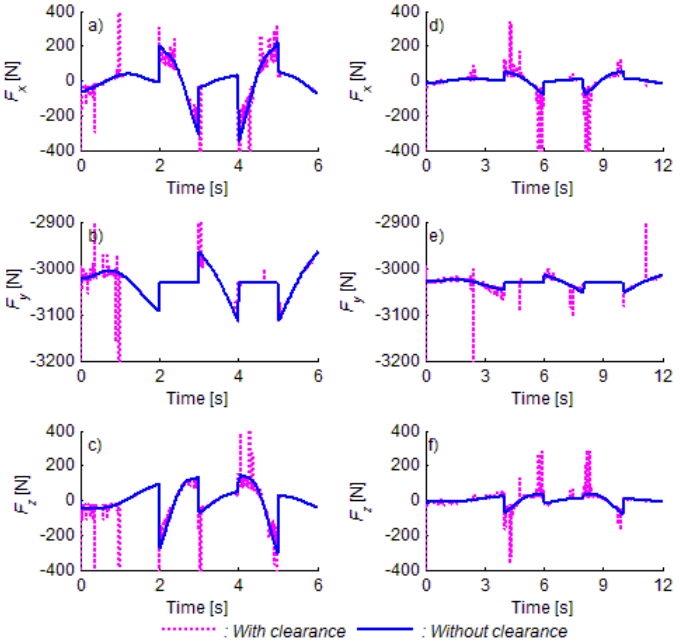

Fig. 7. *Forces for 0.6 mm clearance: a), b) and c) working for 6 seconds, d), e) and f) working for 12 seconds*

These forces occur during a short interval [16] and [48]. Particularly, these peaks are seen at the beginning of the motion, and there is an instant change in force characteristics.

Similarly, in the short working period, the robot manipulator with joint clearance has higher peak frequency [16] and [48]. When the clearance size is increased, there is also an increase in the amplitude of the contact force [22], [36] and [37]. This force characteristic not only reduces the motion sensitivity and repeatability of the robot manipulator, but also leads to a decrease in its vibration and noise quality [20], [22] and [26]. The effects of clearance on torque characteristics are given in Figs. 8 to 10 for different scenarios of clearance value and working period.

The Cartesian components of joints 1 and 2 are used to show the clearance effects on the system torque. Similarly, when the working period for the

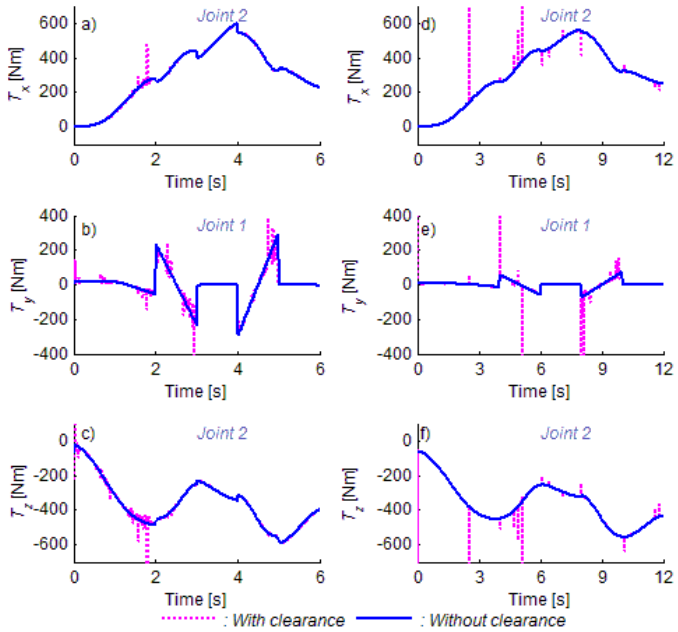

Fig. 8. *Torques for 0.2 mm clearance: a), b) and c) working for 6 seconds, d), e) and f) working for 12 seconds*

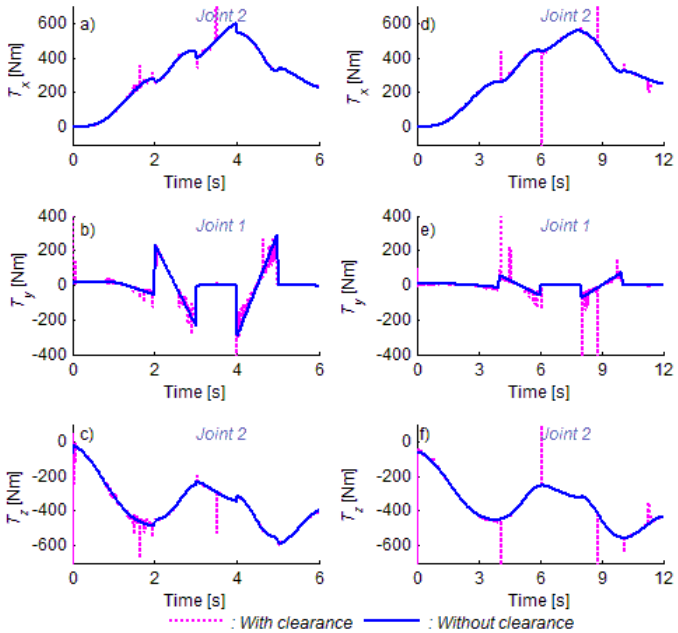

Fig. 9. *Torques for 0.4 mm clearance: a), b) and c) working for 6 seconds, d), e) and f) working for 12 seconds*

same task is reduced, the required torque is also increased. The robot manipulator with joint clearance has some peaks on torques [20]. As seen in the working area, the y component of torque is more important for accomplishing the related trajectory. This can be seen from the peak values and peak frequency. By evaluating the force and torque components together, joint clearance naturally affects all the system dynamics [31], [33], and [34]. The impulsive behaviour arising from a joint with clearance leads to the degradation of the overall system performance [28] and [48]. Similarly, clearance size has a significant role in system response. The dynamics of the robot manipulator are obviously different for the case of

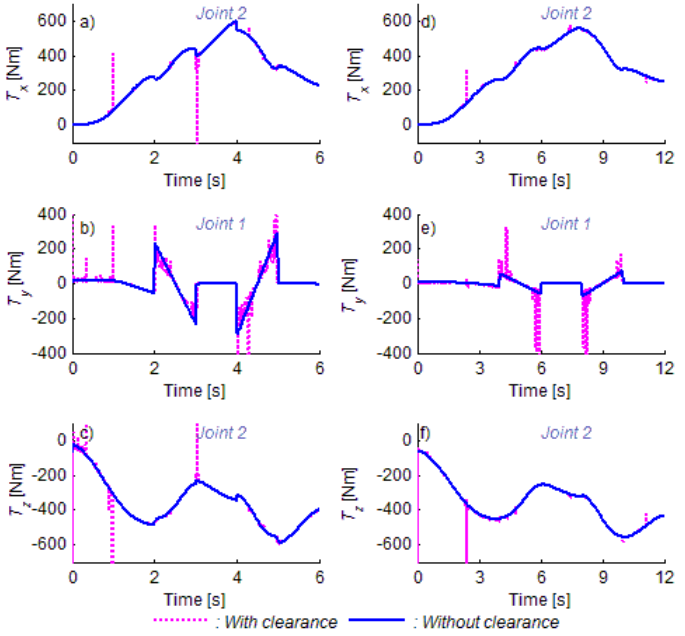

Fig. 10. *Torques for 0.6 mm clearance: a), b) and c) working for 6 seconds, d), e) and f) working for 12 seconds*

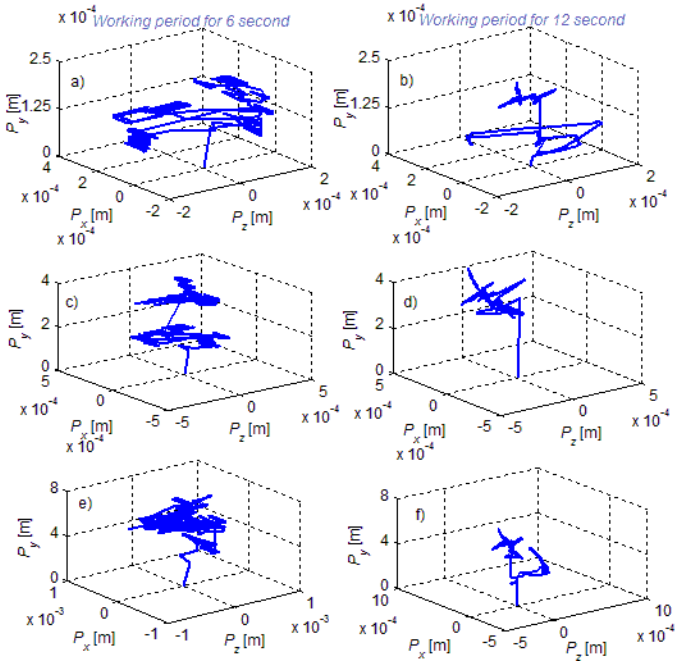

Fig. 11. *Trajectory deviations for different clearance values and working periods: a) and b) 0.2 mm clearance value, c) and d) 0.4 mm clearance value, e) and f) 0.6 mm clearance value*

different clearance sizes and working periods. A lower clearance size leads to a small impulsive character [16]. In the case of the same task, the shorter working period is a dominant factor for peak frequency.

Fig. 11 outlines the trajectory deviations of the end effector for the case of different working periods and clearance sizes. There is a clear trajectory deviation for robot manipulators having perfect and imperfect joints [19]. Motion sensitivity and repeatability are crucial for medical and industrial robots that are used for laser cutting, high-quality welding, etc. Trajectory deviations in the robot manipulator with a clearance joint are clearly seen in Fig. 11. Increases in clearance values naturally lead to an increase in trajectory deviations [6], [14] and [23]. More chaotic behaviour in deviations is seen in the case of the shorter working period for carrying out the same task. More free-flight and then impact modes are the main reasons to fulfil the same trajectory at shorter working times at higher speeds. These deviations can be predicted by using a neural model with suitable input variables. To show the proposed network's stability for predicting the deviations in path components, a 0.6 mm clearance value is considered for both working conditions as a sample application (Fig. 12). As seen in the error-time figures, the NARX model can be used to predict the deviations in trajectory. The convergence capability of the neural model is very effective [24] to [27].

The obtained results are good reflections of the modelling and predicting capabilities of this model [56]. As a performance measuring criterion, the MSE is bigger in the 6-second working period than in the 12-second working period, because the short period is the main reason for peak frequency. Similarly, more complex behaviours in the kinematics and dynamics of the robot manipulator with joint clearance are seen in this period.

Fig. 13 shows a scatter plot of the NARX model with the best fit line of the theoretical trajectory error versus the predicted one. As shown, the scatter plot of theoretical error versus NARX prediction provides a rather good insight for working periods. The correlation for the long working period is higher than for the short one. These correlations are good reflections of the proposed neural model's ability to predict the correct deviations.

4 CONCLUSIONS

Additional degrees of freedom originating from clearance lead to different motion modes. These are sources of uncertainties in robotic manipulations. The model manipulator has six degrees of freedom when all joints are perfect. In the current study, one joint was considered to be imperfect to show the effects of joint clearance on the system. All simulations show that much more computation time is necessary in the

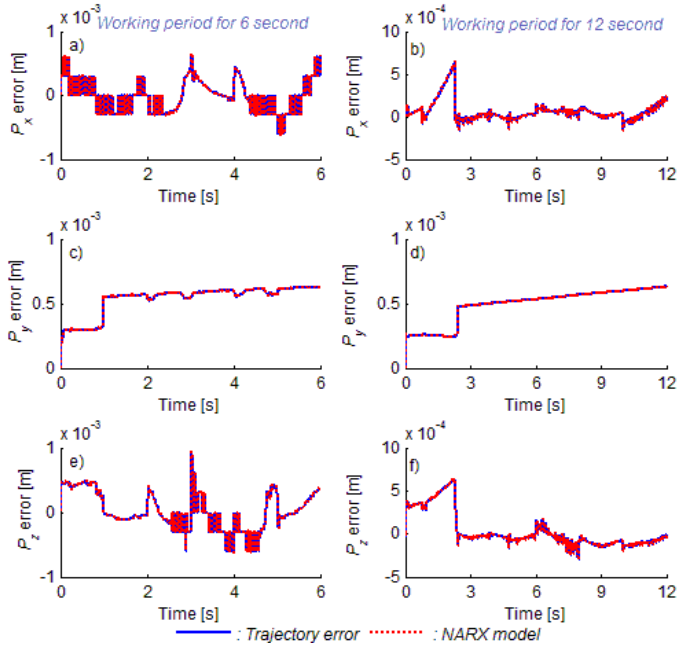

Fig. 12. *Trajectory errors and NARX model for 0.6 mm clearance value: a) and b) x component, c) and d) y component, e) and f) z component*

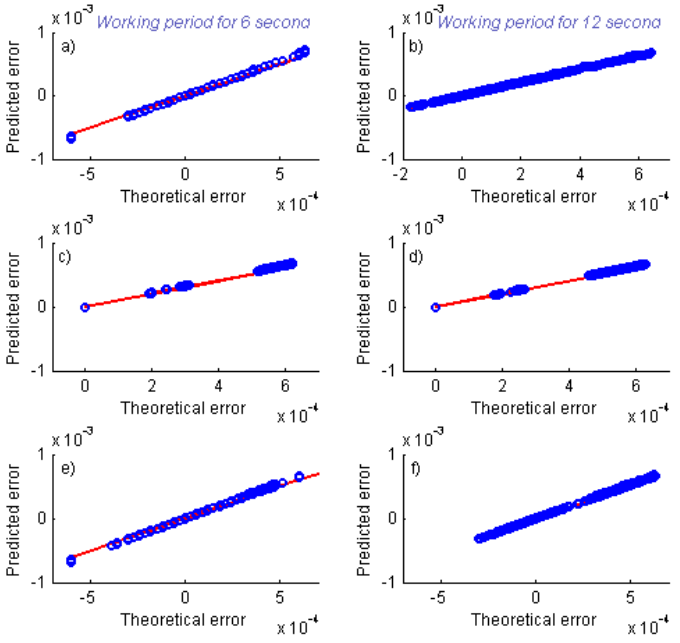

Fig. 13. *Scatter plot of NARX model including a best fit line for 0.6 mm clearance value: a) and b) x component, c) and d) y component, e) and f) z component*

case of the imperfect joint approach. The existence of joint clearance has clear effects on system kinematics and dynamics, and causes impulse-type contact force/torque during a short interval. Both clearance size and working period are important factors in peak amplitude and frequency. When the speed is increased as a result of the reduced working period for carrying out the same task, deviations in the desired trajectory are also more chaotic. An instant change in necessary force or torque leads to an impulsive effect on system outputs. Analyses of robots with joint clearance should be considered as the basis of motion accuracy in robotic manipulations even if the clearance size is small. To predict the trajectory deviations, a dynamic neural model using a suitable input matrix is proposed. This model makes the evaluation of the end effector deviations from the desired trajectory possible. By considering the working period, the approximation error of the neural predictor is smaller in the long period than it is in the short period. These outputs can be used to improve motion sensitivity by designing a robust control system for generating the necessary control outputs. For the future developments, different scenarios such as more clearance joints, lubricated joints having clearances, wear, etc. will be studied.

5 REFERENCES

[1] Corradi, D., Caro, S., Chablat, D., Cardou, P. (2014). Assembly conditions of parallel manipulators considering geometric errors, joint clearances, link flexibility and joint elasticity. *IEEE International Conference on Robotics and Automation*, p. 4067-4072, **DOI:10.1109/ICRA.2014.6907450**.

[2] Al-Widyan, K., Ma, X.Q., Angeles, J. (2011). The robust design of parallel spherical robots. *Mechanism and Machine Theory*, vol. 46, no. 3, p. 335-343, **DOI:10.1016/j.mechmachtheory.2010.11.002**.

[3] Chebbi, A-H., Affi, Z., Romdhane, L. (2009). Prediction of the pose errors produced by joints clearance for a 3-UPU parallel robot. *Mechanism and Machine Theory*, vol. 44, no. 9, p. 1768-1783, **DOI:10.1016/j.mechmachtheory.2009.03.006**.

[4] Frisoli, A., Solazzi, M., Pellegrinetti, D., Bergamasco, M. (2011). A new screw theory method for the estimation of position accuracy in spatial parallel manipulators with revolute joint clearances. *Mechanism and Machine Theory*, vol. 46, no. 12, p. 1929-1949, **DOI:10.1016/j.mechmachtheory.2011.07.004**.

[5] Wu, W., Rao, S.S. (2004). Interval approach for the modeling of tolerances and clearances in mechanism analysis. *Journal of Mechanical Design*, vol. 126, no. 4, p. 581-592, **DOI:10.1115/1.1760775**.

[6] Ting, K.L., Zhu, J., Watkins, D. (2000). The effects of joint clearance on position and orientation deviation of linkages and manipulators. *Mechanism and Machine Theory*, vol, 35, no. 3, p. 391-401, **DOI:10.1016/S0094-114X(99)00019-1**.

[7] Zhu, J., Ting, K.L. (2000). Uncertainty analysis of planar and spatial robots with joint clearances. *Mechanism and Machine Theory*, vol. 35, no. 9, p. 1239-1256, **DOI:10.1016/S0094-114X(99)00076-2**.

[8] Lim, S.R., Kang, K., Park, S., Choi, W.C., Song, J.-B., Hong, D., Shim, J.K. (2002). Error analysis of a parallel mechanism considering link stiffness and joint clearances. *KSME International Journal*, vol. 16, no. 6, p. 799-809, **DOI:10.1007/BF02939339**.

[9] Wu, W., Rao, S.S. (2007). Uncertainty analysis and allocation of joint tolerances in robot manipulators based on interval analysis. *Reliability Engineering and System Safety*, vol. 92, no. 1, p. 54-64, **DOI:10.1016/j.ress.2005.11.009**.

[10] Aginaga, J., Altuzarra, O., Macho, E., Iriarte, X. (2013). Assessing position error due to clearances and deformations of links in parallel manipulators. *Journal of Mechanical Design*, vol. 135, no. 4, p. 041006, **DOI:10.1115/1.4023633**.

[11] Altuzarra, O., Aginaga, J., Hernández, A., Zabalza, I. (2011). Workspace analysis of positioning discontinuities due to clearances in parallel manipulators. *Mechanism and Machine Theory*, vol. 46, no. 5, p. 577-592, **DOI:10.1016/j.mechmachtheory.2011.01.005**.

[12] Zaher, M.H., Megahed, S.M. (2015). Joints flexibility effect on the dynamic performance of robots. *Robotica*, vol. 33, no. 7, p. 1424-1445, **DOI:10.1017/S0263574714000848**.

[13] Bu, W., Liu, Z., Tan, J., Gao, S. (2010). Detachment avoidance of joint elements of a robotic manipulator with clearances based on trajectory planning. *Mechanism and Machine Theory*, vol. 45, no. 6, p. 925-940, **DOI:10.1016/j.mechmachtheory.2010.01.006**.

[14] Erkaya, S. (2012). Investigation of joint clearance effects on welding robot manipulators. *Robotics and Computer-Integrated Manufacturing*, vol. 28, no. 4, p. 449-457, **DOI:10.1016/j.rcim.2012.02.001**.

[15] Binaud, N., Cardou, P., Caro, S., Wenger, P. (2010). The kinematic sensitivity of robotic manipulators to joint clearances. *ASME International Design Engineering Technical Conferences & Computers & Information in Engineering Conference, Volume 2: 34th Annual Mechanisms and Robotics Conference, Parts A and B*, p. 1371-1380, **DOI:10.1115/DETC2010-28635**.

[16] Zhao, Y., Bai, Z.F. (2011). Dynamics analysis of space robot manipulator with joint clearance. *Acta Astronautica*, vol. 68, no. 7-8, p. 1147-1155, **DOI:10.1016/j.actaastro.2010.10.004**.

[17] Jawale, H.P., Thorat, H.T. (2013). Positional error estimation in serial link manipulator under joint clearances and backlash. *Journal Mechanisms Robotics*, vol. 5, no. 2, p. 021003, **DOI:10.1115/1.4023556**.

[18] Chaker, A., Mlika, A., Laribi, M.A., Romdhane, L., Zeghloul, S. (2013). Clearance and manufacturing errors' effects on the accuracy of the 3-RCC Spherical Parallel Manipulator. *European Journal Mechanics-A/Solids*, vol. 37, p. 86-95, **DOI:10.1016/j.euromechsol.2012.05.009**.

[19] Erkaya, S. (2013). Trajectory optimization of a walking mechanism having revolute joints with clearance using ANFIS approach. *Nonlinear Dynamics*, vol. 71, no. 1-2, p. 75-91, **DOI:10.1007/s11071-012-0642-5**.

[20] Erkaya, S., Uzmay, İ. (2009). Investigation on effect of joint clearance on dynamics of four-bar mechanism. *Nonlinear Dynamics*, vol. 58 , p. 179-198, **DOI:10.1007/s11071-009-9470-7**.

[21] Zheng, E., Zhu, R., Zhu, S., Lu, X. (2016). A study on dynamics of flexible multi-link mechanism including joints with clearance and lubrication for ultra-precision presses. Nonlinear Dynamics, vol. 83, no. 1-2, p. 137-159, **DOI:10.1007/s11071-015-2315-7**.

[22] Erkaya, S., Doğan, S. (2015). A Comparative analysis of joint clearance effects on articulated and partly compliant mechanisms. *Nonlinear Dynamics*, vol. 81, no. 1-2, p. 323-341, **DOI:10.1007/s11071-015-1994-4**.

[23] Erkaya, S., Uzmay, İ. (2009). Determining link parameters using genetic algorithm in mechanisms with joint clearance. *Mechanism and Machine Theory*, vol. 44, no. 1, p. 222-234, **DOI:10.1016/j.mechmachtheory.2008.02.002**.

[24] Erkaya, S., Uzmay, İ. (2009). Optimization of transmission angle for slider-crank mechanism with joint clearances. *Structural and Multidisciplinary Optimization*, vol. 37, no. 5, p. 493-508, **DOI:10.1007/s00158-008-0243-6**.

[25] Erkaya, S., Uzmay, İ. (2008). A neural–genetic (NN–GA) approach for optimising mechanisms having joints with clearance. *Multibody System Dynamics*, vol. 20, no. 1, p. 69-83, **DOI:10.1007/s11044-008-9106-6**.

[26] Erkaya, S. (2012). Prediction of vibration characteristics of a planar mechanism having imperfect joints using neural network. *Journal of Mechanical Science and Technology*, vol. 26, no. 5, p. 1419-1430, **DOI:10.1007/s12206-012-0308-8**.

[27] Eski, İ., Erkaya, S., Savaş, S., Yildirim, Ş., (2011). Fault detection on robot manipulators using artificial neural networks. *Robotics and Computer-Integrated Manufacturing*, vol. 27, no. 1, p. 115-123, **DOI:10.1016/j.rcim.2010.06.017**.

[28] Erkaya, S., Uzmay, İ. (2010). Experimental investigation of joint clearance effects on the dynamics of a slider-crank mechanism. *Multibody System Dynamics*, vol. 24, no. 1, p. 81-102, **DOI:10.1007/s11044-010-9192-0**.

[29] Flores, P., Ambrósio, J., Claro, H.C.P., Lankarani, H.M., Koshy, C.S. (2006). A study on dynamics of mechanical systems including joints with clearance and lubrication. *Mechanism and Machine Theory*, vol. 41, no. 3, p. 247-261, **DOI:10.1016/j.mechmachtheory.2005.10.002**.

[30] Flores, P. (2009). Modeling and simulation of wear in revolute clearance joints in multibody systems. *Mechanism and Machine Theory*, vol. 44, no. 6, p. 1211-1222, **DOI:10.1016/j.mechmachtheory.2008.08.003**.

[31] Erkaya, S., Uzmay, İ. (2014). Modeling and simulation of joint clearance effects on mechanisms having rigid and flexible links. *Journal of Mechanical Science and Technology*, vol. 28, no. 8, p. 2979-2986, **DOI:10.1007/s12206-014-0705-2**.

[32] Tian, Q., Liu, C., Machado, M., Flores, P. (2011). A new model for dry and lubricated cylindrical joints with clearance in spatial flexible multibody systems. *Nonlinear Dynamics*, vol. 64, no. 1-2, p. 25-47, **DOI:10.1007/s11071-010-9843-y**.

[33] Erkaya, S., Uzmay, İ. (2012). Effects of balancing and link flexibility on dynamics of a planar mechanism having joint clearance. *Scientia Iranica*, vol. 19, no. 3, p. 483-490, **DOI:10.1016/j.scient.2012.04.011**.

[34] Flores, P., Koshy, C.S., Lankarani, H.M., Ambrósio, J., Claro, J.C.P. (2011). Numerical and experimental investigation on multibody systems with revolute clearance joints. *Nonlinear*

Dynamics, vol. 65, no. 4, p. 383-398, **DOI:10.1007/s11071-010-9899-8**.

[35] Flores, P., Ambrósio, J. (2010). On the contact detection for contact-impact analysis in multibody systems. *Multibody System Dynamics*, vol. 24, no. 1, p. 103-122, **DOI:10.1007/s11044-010-9209-8**.

[36] Erkaya, S., Doğan, S., Şefkatlioğlu, E. (2016). Analysis of the joint clearance effects on a compliant spatial mechanism. *Mechanism and Machine Theory*, vol. 104, p. 255-273, **DOI:10.1016/j.mechmachtheory.2016.06.009**.

[37] Erkaya, S., Doğan, S., Ulus, Ş., (2015). Effects of joint clearance on the dynamics of a partly compliant mechanism: Numerical and experimental studies. *Mechanism and Machine Theory*, vol. 88, p. 125-140, **DOI:10.1016/j.mechmachtheory.2015.02.007**.

[38] Brutti, C., Coglitore, G., Valentini, P.P. (2011). Modeling 3D revolute joint with clearance and contact stiffness. *Nonlinear Dynamics*, vol. 66, no. 4, p. 531-548, **DOI:10.1007/s11071-010-9931-z**.

[39] Flores, P., Ambrósio, J., Claro, J.C.P., Lankarani, H.M. (2006). Spatial revolute joints with clearance for dynamic analysis of multibody systems. *Proceedings of the Institution of Mechanical Engineers, Part-K Journal of Multibody Dynamics*, vol. 220, no. 4, p. 257-271, **DOI:10.1243/1464419JMBD70**.

[40] Marques, F., Flores, P., Claro, J.C.P., Lankarani, H.M. (2016). A survey and comparison of several friction force models for dynamic analysis of multibody mechanical systems. *Nonlinear Dynamics*, vol. 86, no. 3, p. 1407-1443, **DOI:10.1007/s11071-016-2999-3**.

[41] Pennestrì, E., Rossi, V., Salvini, P., Valentini, P.P. (2016). Review and comparison of dry friction force models. *Nonlinear Dynamics*, vol. 83, no. 4, p. 1785-1801, **DOI:10.1007/s11071-015-2485-3**.

[42] Alves, J., Peixinho, N., da Silva, M.T., Flores, P., Lankarani, H.M. (2015). A comparative study on the viscoelastic constitutive laws for frictionless contact interfaces in multibody dynamics. *Mechanism and Machine Theory*, vol. 85, p. 172-188, **DOI:10.1016/j.mechmachtheory.2014.11.020**.

[43] Banerjee, A., Chanda, A., Das, R. (2017). Historical origin and recent development on normal directional impact models for rigid body contact simulation: A critical review. *Archives of Computational Methods in Engineering*, vol. 24, no. 2, p. 397-422, **DOI:10.1007/s11831-016-9164-5**.

[44] Ravn, P. (1998). A continuous analysis method for planar multibody systems with joint clearance. *Multibody System Dynamics*, vol. 2, no. 1, p. 1-24, **DOI:10.1023/A:1009759826529**.

[45] Flores, P., Machado, M., Silva, M.T., Martins, J.M. (2011). On the continuous contact force models for soft materials in multibody dynamics. *Multibody System Dynamics*, vol. 25, no. 3, p. 357-375, **DOI:10.1007/s11044-010-9237-4**.

[46] Machado, M., Moreira, P., Flores, P., Lankarani, H.M. (2012). Compliant contact force models in multibody dynamics: Evolution of the Hertz contact theory. *Mechanism and Machine Theory*, vol. 53, p. 99-121, **DOI:10.1016/j.mechmachtheory.2012.02.010**.

[47] Lankarani, H., Nikravesh, P.E. (1990). A contact force model with hysteresis damping for impact analysis of multibody systems. *Journal of Mechanical Design*, vol. 112, no. 3, p. 369-376, **DOI:10.1115/1.2912617**.

[48] Bai, Z.F., Zhao, Y. (2013). A hybrid contact force model of revolute joint with clearance for planar mechanical systems. *International Journal of Non-Linear Mechanics*, vol. 48, p. 15-36, **DOI:10.1016/j.ijnonlinmec.2012.07.003**.

[49] Suzuki, K. (2011). Artificial Neural Networks-Methodological Advances and Biomedical Applications. *InTech publication*, **DOI:10.5772/644**.

[50] *MATLAB* (2013). The MathWorks Inc, Natick.

[51] Lin, T., Horne, B.G., Tino, P., Giles, C.L. (1996). Learning long-term dependencies in NARX recurrent neural networks. *IEEE Transactions on Neural Networks*, vol. 7, no. 6, p. 1329-1338, **DOI:10.1109/72.548162**.

[52] Chan, R.W.K., Yuen, J.K.K., Lee, E.W.M., Arashpour, M. (2015). Application of nonlinear-autoregressive-exogenous model to predict the hysteretic behaviour of passive control systems. *Engineering Structures*, vol. 85, p. 1-10, **DOI:10.1016/j.engstruct.2014.12.007**.

[53] Chen, S., Bilings, S.A., Grant, P.M. (1990). Non-linear system identification using neural networks. *International Journal of Control*, vol. 51, no. 6, p. 1191-1214, **DOI:10.1080/00207179008934126**.

[54] Leontaritis, I.J., Bilings, S.A. (1985). Input-output parametric models for non-linear systems: Part I: Deterministic non-linear systems. *International Journal of Control*, vol. 41, no. 2, p. 303-328, **DOI:10.1080/0020718508961129**.

[55] Erkaya S. (2012). Analysis of the vibration characteristics of an experimental mechanical system using neural networks. *Journal of Vibration and Control*, vol. 18, no. 13, p. 2059-2072, **DOI:10.1177/1077546311429059**.

[56] Yildirim, Ş., Erkaya, S., Su Ş., Uzmay, İ. (2005). Design of neural networks model for transmission angle of a modified mechanism. *Journal of Mechanical Science and Technology*, vol. 19, no. 10, p.1875-1884, **DOI:10.1007/BF02984266**.

Strojniški vestnik - Journal of Mechanical Engineering 64(2018)2, 95-104

DOI:10.5545/sv-jme.2017.4742
Original Scientific Paper
Received for review: 2017-07-18
Received revised form: 2017-12-11
Accepted for publication: 2017-12-18

Optimization of Oil Pads on a Hydrostatic Turntable for Supporting Energy Conservation Based on Particle Swarm Optimization

Yumo Wang[1] – Zhifeng Liu[1,*] – Ligang Cai[1] – Qiang Cheng[1] – Xiangmin Dong[2]
[1] Beijing University of Technology, Key Laboratory of Advanced Manufacturing Technology, China
[2] Chengde Petroleum College, Department of Mechanical Engineering, China

The performance of hydrostatic turntables is strongly influenced by the geometry of oil pads. The properly designed structure of oil pads can reduce the power consumption of hydrostatic turntables and improves their service performance. A structural optimization of oil pads on a hydrostatic turntable based on particle swarm optimization is presented to improve the carrying performance and decrease energy costs. Using the finite difference method, the Reynolds equation is resolved to calculate the pressure distribution and flow rate in oil pads. The power cost of oil supply is determined according to the turntable working condition, and minimal energy consumption is set as the optimal solution. The geometrical parameters of the oil pad are chosen as individual elements that will converge to an optimal result by using PSO.
Keywords: hydrostatic turntable, Reynolds equation, PSO, energy conservation

Highlights

- *Performance characteristics, such as pressure distribution and oil flow rate, are determined by the Reynolds equation and finite difference method (FDM).*
- *The relationship between oil pocket scale and supporting power consumption is determined numerically. Reliability of the algorithm is verified by conducting experiments on a miniature testing table.*
- *PSO is carried out to solve the optimal pocket size for minim pump power. An efficient and practical optimization method for hydrostatic turntable design is presented.*

0 INTRODUCTION

The hydrostatic turntable is a key part of heavy-duty computerized numerical control (CNC) machine tools, which plays a supporting role and provides high precision rotary motion. The external supply system continuously pumps pressurized oil into oil pads. The cost of running a hydrostatic turntable can be reduced by reducing the power consumption of oil pads. The analysis and optimization of hydrostatic bearing are complex, requiring many numerical computations. The geometrical size of oil pad is accurate to millimetres, considering processing feasibility. Therefore, an optimization algorithm with high efficiency and acceptable accuracy is needed to optimize hydrostatic bearing; particle swarm optimization (PSO) is an efficient computational method, suitable for efficiently reducing computational load.

Wang et al. **[1]** presented a fast-convergent numerical method to solve the modified Reynolds equation. Singh et al. **[2]** applied different types of modified Reynolds equations in analysing different shapes of oil pads. Liu et al. **[3]** provided the general type of the Reynolds equation of circular and rectangular oil pads. The variation of viscosity caused by temperature changes was ignored in the study of El Khlifi et al. **[4]** based on the low moving speed working condition. Mankovits et al. **[5]** conducted his optimal research by using a support vector regression method. Gustafsson et al. **[6]** introduced changing viscosity in the Reynolds equation. Yang et al. **[7]** introduced non-Newtonian characteristics into the Reynolds equation. Masjedi and Khonsari **[8]** solved the Reynolds equation by the efficient numerical method of successive over-relaxation (SOR). Getachew and Prawal **[9]** analysed the lubrication performance of a slider by using finite different method (FDM). Cai et al. **[10]** optimized the oil pad structure to improve the stiffness of the hydrostatic guideway. Weißbacher et al. **[11]** reformed the film clearance to improve the support performance of hydrostatic journal bearing. Cheng et al. **[12]** applied PSO to diverse types of hydrostatic and aerostatic bearing. Chang and Jeng **[13]** designed a double-pad aerostatic bearing using PSO. Chan **[14]** conducted an optimization research on hybrid journal bearings by PSO. Soltani-Mohammadi et al. **[15]** proved that the PSO is more efficient in computing in comparison to a simulated annealing method. Zheng and Liao **[16]** used social emotional PSO (SEPSO). Srisha Rao and Jagadeesh **[17]** improved the convergence of an optimization algorithm by using vector evaluated PSO (VEPSO). Flocker and Bravo **[18]** discussed the global convergence of PSO in their article. Tang et al. **[19]**

*Corr. Author's Address: Beijing University of Technology, Key Laboratory of Advanced Manufacturing Technology, China, lzfeng1@126.com

applied PSO in the energy conservation of a workshop. Luo et al. [20] proposed a dynamic optimal solution based on Species-based PSO (SPSO). Liu et al. [21] made a comparison between different optimization methods in a review. All the above studies show that PSO is a broadly applicable optimization method for many circumstances.

A practical optimization method based on PSO for a hydrostatic turntable is proposed in this work to improve its service performance. The Reynolds equation of the hydrostatic turntable is modified according to the working condition. Performance characteristics, such as pressure distribution and oil flow rate, are determined by FDM. The geometry size of oil pads is selected as individuals in the optimization progress. With minimum film thickness set to a constant safety level, the power consumption is chosen as the fitness of each individual. Finally, through the PSO algorithm, the optimal solution is determined.

1 HYDROSTATIC TURNTABLE MODELING AND GENERAL EQUATIONS

1.1 Model of Hydrostatic Turntable

A hydrostatic turntable is an essential part of heavy machine tools, which is supported by several oil pads on the base. A model of a hydrostatic turntable is shown in Fig. 1.

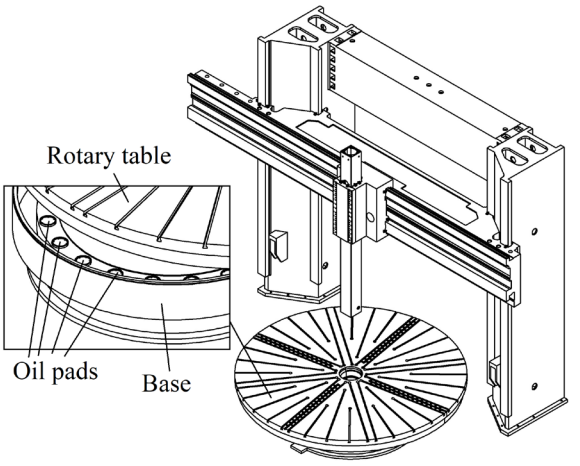

Fig. 1. *Model of hydrostatic turntable on heavy machine tools*

The supporting oil pad of hydrostatic turntable is a circular step pad with concentric oil pockets, and there are N supporting pads on the rotary table. A model of a circular oil pad is shown in Fig. 2, where R_0 is the radius of oil pad, R_1 is the radius of oil pocket, H is the oil film thickness of the supporting pad.

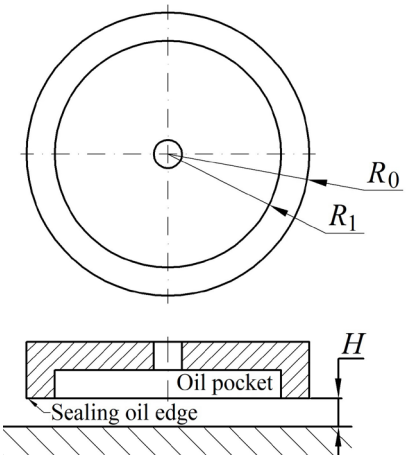

Fig. 2. *The structure of the supporting oil pad*

In [10], the load-carrying capacity of the bearing and oil film thickness are considered to be a -3 power relationship. Without maximum pump pressure limit, the bearing ability is infinitely large when film thickness approaches zero. In real working conditions, this assumption leads to inaccurate calculations, especially when the oil film is thin. Due to factors such as surface roughness, geometry error, and tilting, a thinner oil film means more chance for film collapse, which seriously affects the service performance of machine tools. Therefore, the oil film of a hydrostatic turntable needs to be regulated to a safe level to avoid damage. The working condition of the hydrostatic turntable can be written as:

$$\begin{cases} H \geq H_0 \\ \sum_{i=1}^{N} W_i = mg \end{cases}, \tag{1}$$

where H_0 is the pre-set film thickness, W_i is the load-carrying capacity of i^{th} oil pad, N is the total number of oil pads, m is the carrying load, and g is the acceleration of gravity.

1.2 The Reynolds Equation and FDM Solution

The Reynolds equation is widely used in the analysis of hydrostatic systems to describe the pressure distribution of viscous oil film in oil pads. The following dimensionless parameters are defined before solving the Reynolds equation:

$$\overline{p} = \frac{p}{P_0}, \quad \overline{p_0} = 1, \quad \overline{r} = \frac{r}{R_0}, \quad \overline{R}_0 = 1, \quad \overline{z} = \frac{z}{H},$$

$$\bar{h}=\frac{h}{H},\quad \bar{H}=1,\quad \bar{U}_r=\frac{U_r}{\frac{H_0^2P_0}{R_0\eta}},\quad \bar{U}_\theta=\frac{U_\theta}{\frac{H_0^2P_0}{R_0\eta}},$$
$$\bar{W}=\frac{W}{R_0^2P_0},\quad \bar{q}=\frac{Q}{\frac{H_0^3P_0}{\eta}}, \tag{2}$$

where p is the pressure, P_0 is the pressure in the oil pocket, r is the radial coordinate, h is the film thickness, U_r is the radial velocity, U_θ is the circumferential velocity, W is the load-carrying capacity, Q is the volumetric flow rate of each oil pad, and η is the viscosity. Furthermore, $\bar{p}$ is the dimensionless pressure, $\bar{h}$ is the dimensionless film thickness, $\bar{U}_r$ is the dimensionless radial velocity, $\bar{U}_\theta$ is the dimensionless radial velocity, $\bar{W}$ is the dimensionless load-carrying capacity, and $\bar{q}$ is the dimensionless flow rate.

The oil pocket is usually designed to be of 5 mm to 10 mm depth, thicker than the boundary layer of the oil flow. Therefore, no pressure loss exists when the oil flows through the oil pocket. The film thickness at the oil-sealing edge is usually designed to be from tens to hundreds of microns, smaller than the boundary layer of oil flow, so the oil-sealing edge keeps the pressure unchanged in the oil pocket. In a polar coordinate system, the Reynolds equation describing the pressure distribution of the oil film in an oil-sealing edge is written as Eq. (3) **[3]**:

$$\frac{\partial}{\partial\bar{r}}\left(\bar{r}\cdot\bar{h}^3\cdot\frac{\partial\bar{p}}{\partial\bar{r}}\right)+\frac{\partial}{\partial\bar{\vartheta}}\left(\bar{h}^3\cdot\frac{\partial\bar{p}}{\bar{r}\partial\bar{\vartheta}}\right)=$$
$$=6\frac{\partial}{\partial\bar{r}}\left(\bar{r}\overline{U_r}\bar{h}\right)+6\frac{\partial}{\partial\bar{\vartheta}}\left(\overline{U_\vartheta}\bar{h}\right). \tag{3}$$

The hydrostatic turntable remains steady in this research, so the velocity can be ignored. The Reynolds equation is modified as Eq. (4):

$$\frac{\partial}{\partial\bar{r}}\left(\bar{r}\cdot\bar{h}^3\cdot\frac{\partial\bar{p}}{\partial\bar{r}}\right)+\frac{\partial}{\partial\bar{\vartheta}}\left(\bar{h}^3\cdot\frac{\partial\bar{p}}{\bar{r}\partial\bar{\vartheta}}\right)=0. \tag{4}$$

The discretization of the Reynolds partial differential equation is performed by adopting the FDM method; dimensionless pressure distribution can be determined via the Gauss-Seidel iteration. Therefore, the discrete Reynolds equation is written as **[9]**:

$$\left[A1_{i,j}\,A2_{i,j}\,A3_{i,j}\,A4_{i,j}\,A5_{i,j}\right]\begin{bmatrix}\bar{p}_{i+1,j}\\ \bar{p}_{i-1,j}\\ \bar{p}_{i,j}\\ \bar{p}_{i,j-1}\\ \bar{p}_{i,j+1}\end{bmatrix}=0, \tag{5}$$

$$\begin{cases} A1_{i,j}=\dfrac{\bar{r}_i\bar{h}_{i,j}^3}{\bar{r}_{step}^2}\\ A2_{i,j}=\dfrac{\bar{r}_{i-1}\bar{h}_{i-1,j}^3}{\bar{r}_{step}^2}\\ A3_{i,j}=-\left(\dfrac{\bar{r}_i\bar{h}_{i,j}^3}{\bar{r}_{step}^2}+\dfrac{\bar{r}_{i-1}\bar{h}_{i-1,j}^3}{\bar{r}_{step}^2}+\dfrac{\bar{h}_{i,j-1}^3}{\bar{r}_i\bar{\theta}_{step}^2}+\dfrac{\bar{h}_{i,j}^3}{\bar{r}_i\bar{\theta}_{step}^2}\right)\\ A4_{i,j}=\dfrac{\bar{h}_{i,j-1}^3}{\bar{r}_i\bar{\theta}_{step}^2}\\ A5_{i,j}=\dfrac{\bar{h}_{i,j}^3}{\bar{r}_i\bar{\theta}_{step}^2}\end{cases}, \tag{6}$$

where $\bar{r}_{step}$ is the step length for the r coordinate, $\bar{\theta}_{step}$ is the step length for the θ coordinate, and i and j are numerical counts of the elements on r and θ coordinate, respectively. The boundary condition of dimensionless pressure $p_{i,j}$ is chosen as 1 in the oil pocket and 0 at the external edge of the oil pad:

$$\bar{p}_{i,j}=\begin{cases}1, & \bar{r}_i<\bar{R}_1\\ 0, & \bar{r}_i=1\end{cases}. \tag{7}$$

The calculation process of FDM will be terminated when the results match the error tolerance tol_{FDM}. The dimensionless load-carrying capacity of the oil pad can be calculated by integrating the hydrostatic dimensionless pressure distribution, while the dimensionless flow rate is determined by integrating the outer flow speed on the external surface. The load-carrying performance is written as Eq. (8):

$$\begin{cases}\bar{w}=\bar{p}\,\bar{r}\,d\bar{r}\,d\bar{\theta}\\ \bar{q}=\int\dfrac{\bar{z}^2-\bar{z}}{2\eta}\dfrac{\partial\bar{p}}{\partial\bar{r}}d\bar{z},\quad where\ \bar{r}_i=1\end{cases}, \tag{8}$$

$\bar{w}$ and $\bar{q}$ are important parameters to evaluate the supporting performance of hydrostatic bearings, which varies with the changing of $\bar{R}_1$ value. For the safe operation of the machine tool, a minimum film thickness H_0 is chosen to avoid damaging the machine tools. The safety film thickness is set as $H\geq H_0$. Assuming the carrying weight is constant, the pump power P_s is **[10]**:

$$\begin{cases}P_0=\dfrac{mg}{N\bar{w}\pi R_0^2}\\ Q=\bar{q}\dfrac{H_0^3P_0}{\eta}\\ P_s=N\cdot P_0\cdot Q\end{cases}, \tag{9}$$

where P_s is the supporting power consumption, and it only describes the pump power caused in oil pads. To control variables in this optimization, motor efficiency and pressure losses are ignored.

1.3 Particle Swarm Optimization

PSO is an emerging optimization method with high computational and implementation efficiency. The analysis of the hydrostatic turntable using the FDM technique requires performing many numerical calculations that make the process very time-consuming. Different values of R_1 result in different $\overline{w}$ and $\overline{q}$, i.e. different supporting power consumption. Aiming at the pump power optimization, many calculation loops are required to calculate the optimal value of R_1, so PSO is a suitable method to efficiently reduce the calculation time and simplify the optimization process. In this paper, PSO is basically performed by evaluating the fitness of each individual in the domain to search for a fitting range until it matches error tolerance. An inertia weight ω is introduced to improve local search ability [16]:

$$\begin{cases} v_n^{(k+1)} = \omega v_n^{(k)} + c_1\left(Pbest_n - x_n^{(k)}\right) + c_2\left(Gbest_n - x_n^{(k)}\right) \\ x_n^{(k+1)} = x_n^{(k)} + v_n^{(k+1)} \end{cases}, \quad (10)$$

where x_n and v_n are the position and velocity of the n^{th} individual, respectively, $Pbest_n$ is the position of the privative best fitness of the n^{th} individual, $Gbest_n$ is the position of the global best fitness of all individuals, and k is the loop iteration count.

Every individual represents a value of R_1, and makes $R_1 = x_n \cdot R_0$. FDM can solve and case by case. The fitness of each individual is evaluated by the supporting power consumption. The minimization of pump power is chosen as the optimal target. Computing will be terminated when every single individual as while as the whole swarm matches the error tolerance. The design tolerance of oil pad is generally at the millimetre scale, so error tolerance of PSO is set as 10^{-2} [13]. The terminating condition is:

$$\begin{cases} \left|x_n^{(k)} - x_n^{(k-1)}\right| \le tol_{PSO} \\ \max\left(x_n^{(k)}\right) - \min\left(x_n^{(k)}\right) \le tol_{PSO} \end{cases}. \quad (11)$$

The algorithm presented in this work is mainly composed of three parts: FDM solution of the Reynolds equation, evaluation of supporting power and PSO for minimal power consumption; Fig. 3 illustrates the detailed calculation process [12].

2 NUMERICAL RESULTS AND DISCUSSION

2.1 Influence of Dimensionless Pocket Scale on the Load-Carrying Performance of Circular Oil Pads

The optimal pocket size can be determined by the algorithm shown in Fig. 3 for minimum supporting power consumption. Table 1 lists the values of the

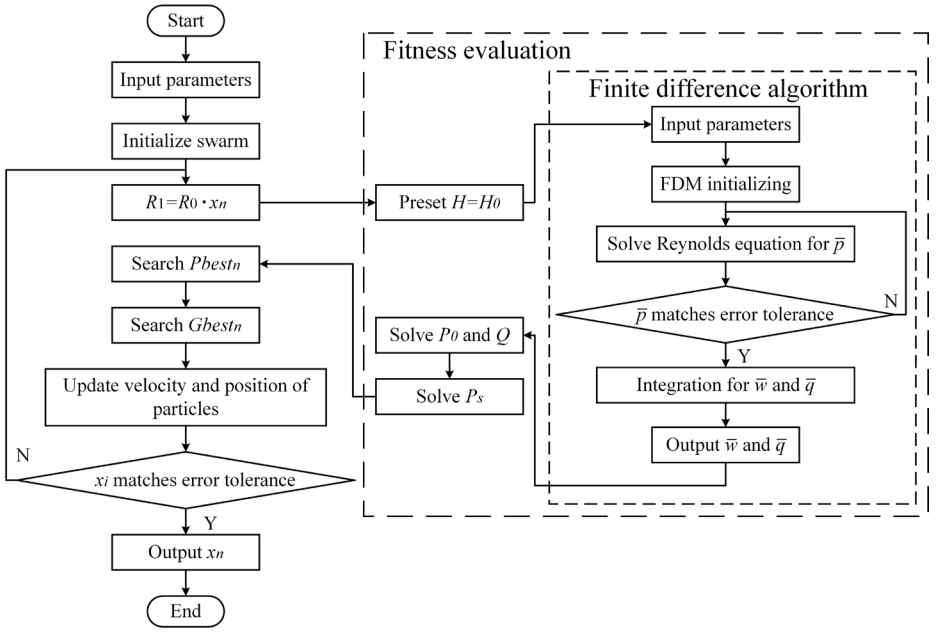

Fig. 3. *The PSO implementation framework*

main parameters involved in the computational process.

Table 1. *Values/Ranges of major parameters*

Parameter	Value	Parameter	Value
R_0	0.085 m	n	5
m	24800 kg	ω	0.2
N	20	c_1	0.4
η	0.06 Pa·s	c_2	0.9
Tol_{FDM}	1×10^{-7}	Tol_{PSO}	6

The supporting performance of an oil pad can be described by dimensionless load-carrying capacity and dimensionless flow rate. The dimensionless load-carrying capacity corresponds to the force output of oil pads, while the dimensionless flow rate corresponds to the oil flow required to maintain the film thickness. Changes in oil pocket size will influence both the dimensionless carrying capacity and dimensionless flow rate. The pressure distribution for different oil pocket sizes is shown in Fig. 4.

As shown in Fig. 4, the oil pocket is filled with pressurized oil which provides most of the load-carrying capacity of the oil pad. Therefore, a larger oil pocket means greater load-carrying force. With dimensionless oil pocket size increases, the slope at the oil film sealing edge grows leading to the increase of the dimensionless flow rate. Fig. 5 shows the dimensionless pocket size effect on the supporting performance of the oil pad.

From Fig. 5, both the dimensionless carrying capacity $\bar{w}$, and flow rate $\bar{q}$ increase with the increase of pocket size $\bar{R}_1$. Flow rate $\bar{q}$ grows more significantly than $\bar{w}$. A larger dimension of the pocket means greater supply flow rate and lower pump pressure. The supporting power consumption is highly related to the supply flow rate and pump pressure. The difference between the influence of the pocket dimension on the supply flow rate and the pump pressure shows that there is room for improvement. When $\bar{R}_1$ varies within the range (0.1, 0.9), the influence of the pocket on supporting power is shown

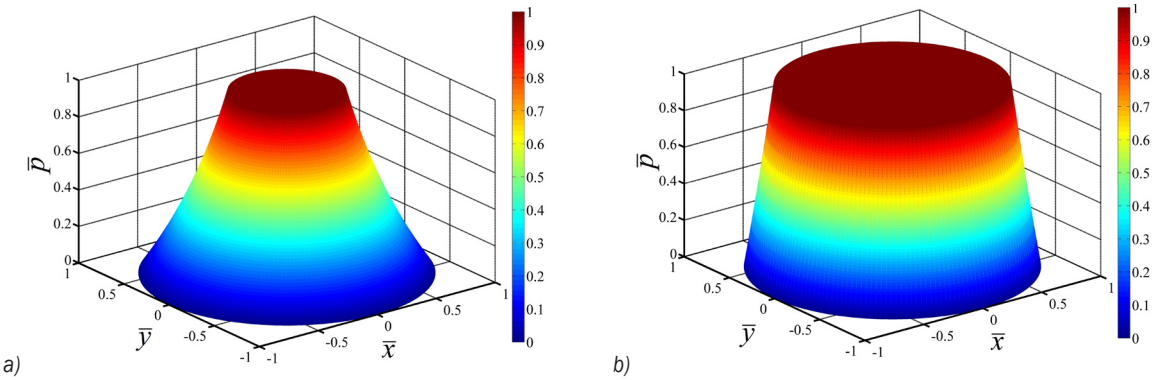

Fig. 4. *Dimensionless pressure distribution of circular oil pad; a)* $\bar{R}_1$ *=0.4, and b)* $\bar{R}_1$ *=0.8*

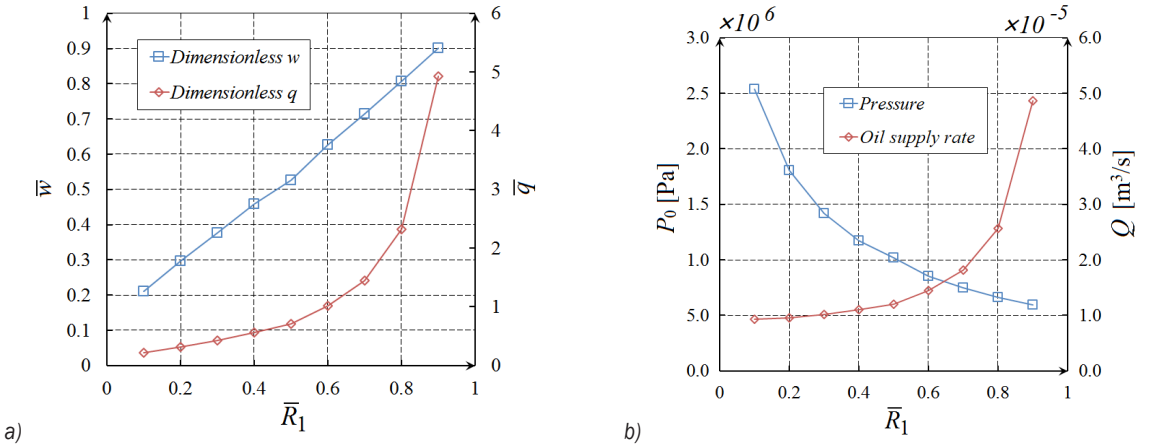

Fig. 5. *Supporting performance of circular oil pad for different* $\bar{R}_1$ *; a) dimensionless load-carrying capacity and flow rate, and b) pressure and oil supply rate*

in Fig. 6, and a minimum value of the curve of supporting power P_s clearly exists:

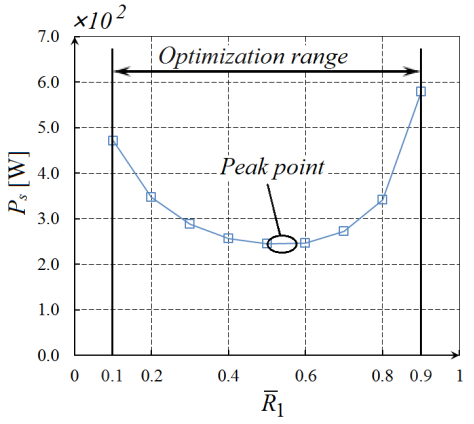

Fig. 6. *Supporting power consumption varying* $\bar{R}_1$

However, the exhaustive method can only show the trend vaguely and thus is not suitable for solving optimal result. The exact place where P_s achieves its minimum needs to be determined with the help of PSO.

2.2 Experimental Verification on a Miniature Oil Pad

Due to cost and safety constraints, it is difficult to carry out experiments on a hydrostatic turntable. To verify the theoretical calculations, an experiment table for a single oil pad is designed. The carrying performance of a replaceable oil pad can be measured under different bearing situations. Oil is supplied by a pump, and the flow rate is adjusted by a flow valve. Film thickness can be changed by a lead screw with a very large reduction ratio. The film thickness varies 2 μm for every turn of the screw hand wheel. Three force sensors, two dial indicators, one flowmeter, one manometer, and one thermometer are deployed to measure related parameters. Data from each sensor is stored by a collector by real time. The experimental table is shown in Fig. 7.

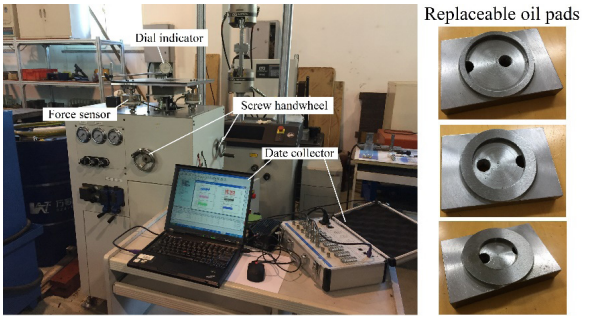

Fig. 7. *Experimental table to test single oil pad*

To verify the reliability of the theoretical algorithm, four different oil pads are tested. Their structural parameters are shown in Table 2.

Table 2. *Structural parameters of testing oil pads*

	R_0	R_1	$\bar{R}_1$
Pad 1	0.033 m	0.028 m	0.848485
Pad 2	0.033 m	0.023 m	0.69697
Pad 3	0.033 m	0.018 m	0.545455
Pad 4	0.033 m	0.013 m	0.393939

Several tests are conducted to determine the dimensionless carrying ability and flow rate of oil pads, based on Eq. (2). Compared with the theoretical result, the experimental results of dimensionless carrying ability are smaller, and the maximum error is about 18 %. Deviation also appears between the

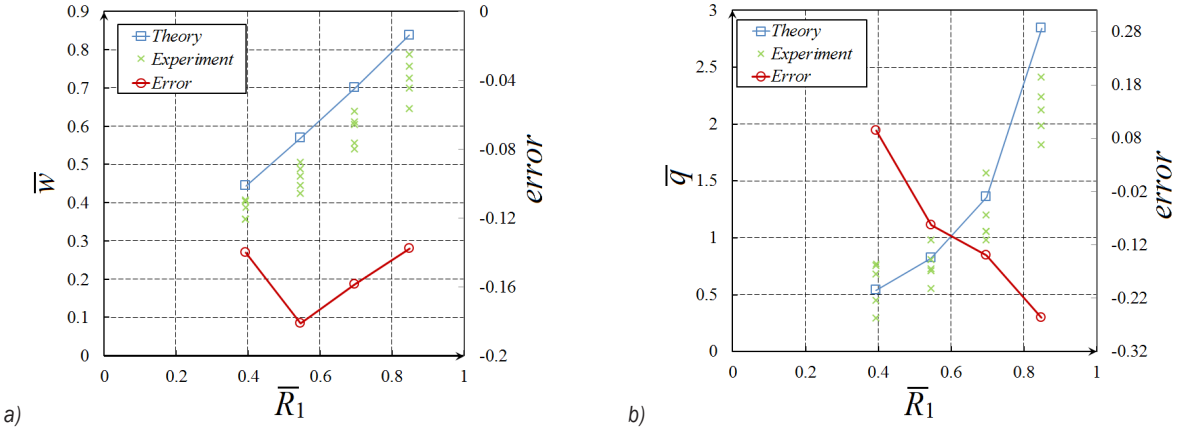

Fig. 8. *Comparison between theoretical and experimental results; a) dimensionless carrying force, b) dimensionless flow rate*

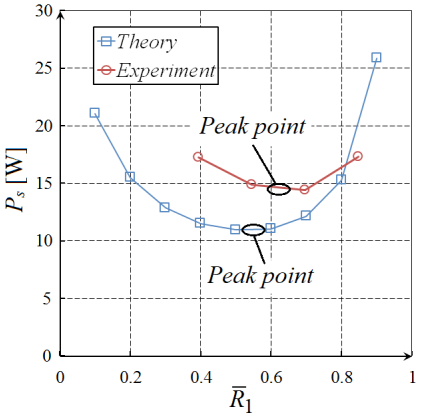

Fig. 9. *Power estimate of single oil pad testing*

theoretical and experimental dimensionless flow rates. The maximum error is about 25 %. Although there are some errors between the calculation and tests, the varying trend of dimensionless carrying force and flow rate with $\bar{R}_1$ is the same as predicted.

According to the result shown in Fig. 6, there is an optimal value of $\bar{R}_1$ to achieve minimum supporting power P_s. The supporting power is calculated based on the experimental result shown in Fig. 8.

As shown in Fig. 9, both the theoretical and experimental result shows a minimum P_s exists. The following optimization is carried out by the real hydrostatic turntable parameters shown in Table 1.

2.3 Optimal Solution of Oil Pocket Scale Based on Particle Swarm Optimization

The initial position and speed of particles x_n are chosen randomly in the domain. Assuming $R_1 = x_n \cdot R_0$, the oil pocket scale is related with particle positions. The film thickness is set to H_0, and the supporting performance is solved by FDM to determine the pump power consumption. PSO can determine the position of minimum power consumption by evaluating the fitness of each particle. Fig. 10 shows the iteration process of PSO when $H_0 = 5\times10^{-5}$ m, where *OS* is optimal solution determined by PSO and *I*1, *I*2, …,

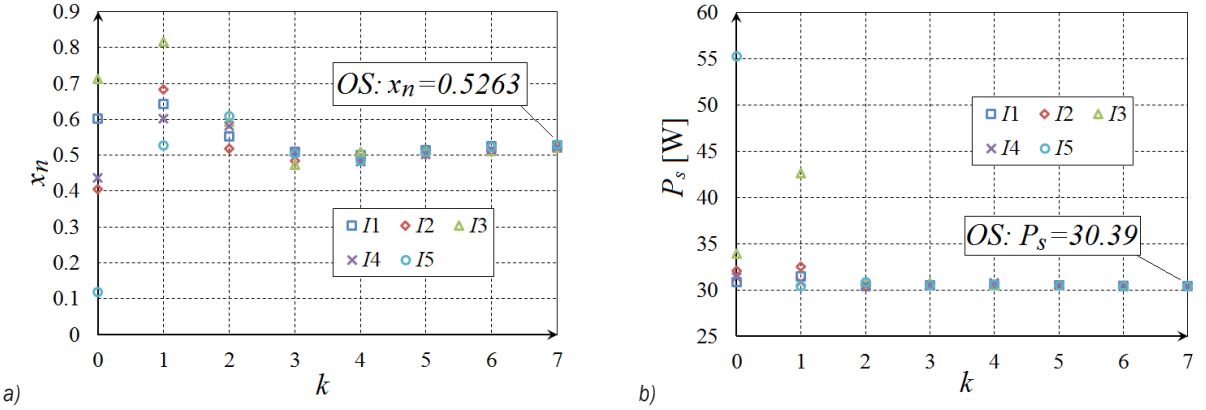

a) b)

Fig. 10. *Iterative process of PSO ($H_0 = 5\times10^{-5}$ m); a) position of each individual, b) supporting power of each individual*

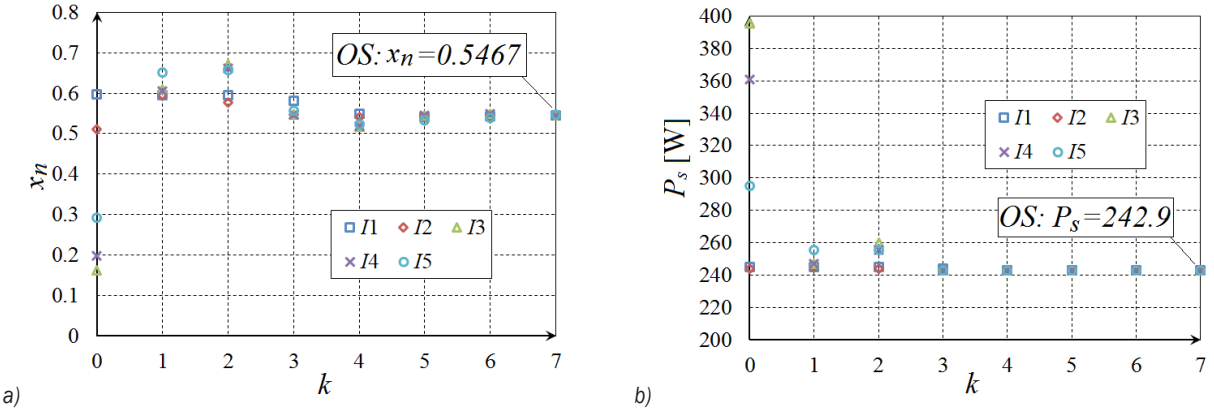

a) b)

Fig. 11. *Iterative process of PSO ($H_0 = 10\times10^{-5}$ m); a) position of each individual, and b) supporting power of each individual*

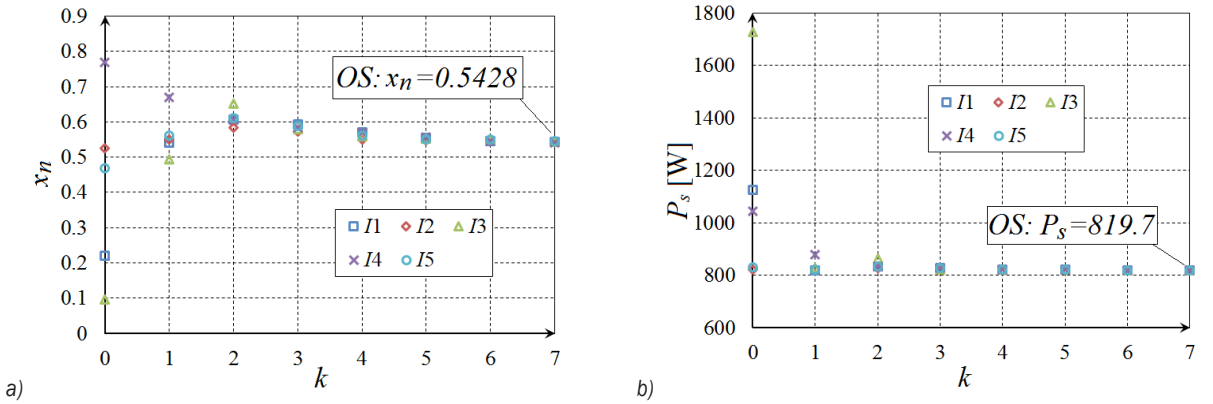

Fig. 12. *Iterative process of PSO (H_0 = 15×10^{-5} m); a) position of each individual, and b) supporting power of each individual*

In are individuals. From Fig. 7, the algorithm needs 7 loops to meet the error tolerance when the number of particle swarms is chosen as 5. Individuals get close to each other rapidly from distinct positions and converge to x_n = 0.5263 where P_s = 30.39. Figs. 11 and 12 show the iteration process of PSO when H_0 is set to 10×10^{-5} m and 15×10^{-5} m, respectively.

The algorithm needs 7 loops to meet the error tolerance. When H_0 = 10×10^{-5} m, all particles converge to x_n = 0.5467 where P_s = 242.9. When H_0 = 15×10^{-5} m, all particles converge to x_n = 0.5428 where P_s = 819.7. The change of H_0 value influences the final result x_n by no more than 3.9 %. However, varying H_0 has a strong effect on P_s, meaning a thicker film thickness needs a higher supporting power. Taking 14 different samples of H_0, the relationship between film thickness, pump power consumption, and optimal pocket size is shown in Fig. 13.

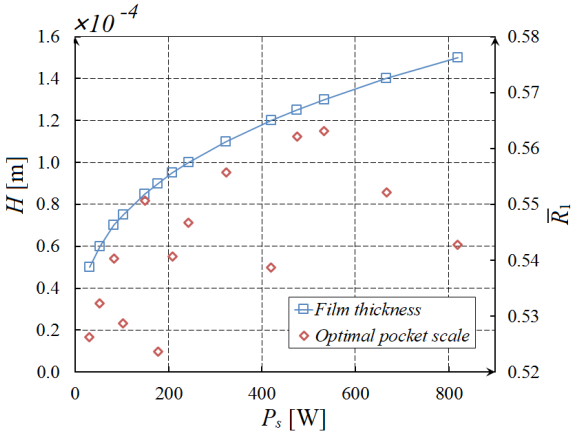

Fig. 13. *Relationship between film thickness, supporting power and oil pocket scale*

The supporting power consumption raises with the film thickness increase. The optimal pocket scale changes no more than 7 % under different film thickness, a percentage that could be considered as a computational error. The average optimal pocket size of 14 samples is determined as $\bar{R}_1$ = 0.5431.

3 CONCLUSIONS

In this work, the load-carrying performance of a hydrostatic turntable is analysed using an FDM solution of the Reynolds equation. The relationship between oil pocket scale and supporting power consumption is determined numerically. The reliability of the algorithm is verified by conducting experiments on a miniature testing table. PSO is carried out to solve the optimal pocket size for minimal pump power. An efficient and practical optimization method for hydrostatic turntable design is presented, and the following conclusions can be drawn:

1. The oil pocket scale strongly influences the supporting power consumption. A properly designed oil pocket reduces the supporting power and improves the service performance of the hydrostatic turntable.
2. When the film thickness is set as a constant (to a safety value), the optimal pocket size of $\bar{R}_1$ = 0.5431 is calculated. With increases in film thickness, the supporting power consumption grows, but optimal pocket size remains nearly the same. The optimal oil pocket scale varies no more than 7 % under different film thicknesses.
3. The design tolerances of the oil pad are at a millimetre scale, and the FDM analysis processes are always very time-consuming. Therefore, the PSO is a suitable optimization method to speed up calculations and overcome such issues.

4 ACKNOWLEDGMENT

The authors would like to thank the National Natural Science Fund coded 51575009, the National Science and Technology Major Project coded 2018ZX04043, Beijing Natural Science Fund coded 3162003 and Jing-Hua Talents Project of Beijing University of Technology for supporting the research.

5 NOMENCLATURES

$A1_{i,j}$, $A2_{i,j}$, …	coefficient matrix, [-]
g	acceleration of gravity, [m·s^{-2}]
$Gbest_n$	position of the global best fitness of all individuals, [-]
H	film thickness, [m]
H_0	preset film thickness, [m]
$\bar{h}$	dimensionless film thickness, [-]
i	numerical counts of the elements on r coordinate
j	numerical counts of the elements on θ coordinate, [-]
k	loop iteration count, [-]
N	total number of oil pads, [-]
m	carrying load, [kg]
p	pressure, [Pa]
P_0	pressure in the oil pocket, [Pa]
P_S	supporting power, [W]
$\bar{p}$	dimensionless pressure, [-]
$Pbest_n$	position of the privative best fitness of the n^{th} individual, [-]
R_0	radius of oil pad, [m]
R_1	radius of oil pocket, [m]
$\bar{r}_{step}$	step length for the r coordinate, [-]
Q	volumetric flow rate, [m^3·s^{-1}]
$\bar{q}$	dimensionless flow rate, [-]
U_r	radial velocity, [m·s^{-1}]
U_θ	circumferential velocity, [m·s^{-1}]
$\bar{U}_r$	dimensionless radial velocity, [-]
$\bar{U}_\theta$	dimensionless radial velocity, [-]
v_n	velocity of the n^{th} individual, [-]
x_n	position of the n^{th} individual, [-]
W	load-carrying capacity, [N]
W_i,	load-carrying capacity of i^{th} oil pad, [N]
$\bar{W}$	dimensionless carrying capacity, [-]
η	viscosity, [Pa·s]
$\bar{\theta}_{step}$	step length for the θ coordinate

6 REFERENCES

[4] Wang, N., Cha, K.-C., Huang, H.-C. (2012). Fast convergence of iterative computation for incompressible-fluid Reynolds equation. *Journal of Tribology*, vol. 134, no. 4, p. 024504, **DOI:10.1115/1.4006360**.

[5] Singh, U.P., Gupta, R.S., Kapur, V.K. (2012). On the steady performance of annular hydrostatic thrust bearing: Rabinowitsch fluid model. *Journal of Tribology*, vol. 134, no. 4, p. 044502, **DOI:10.1115/1.4007350**.

[6] Liu, Z., Wang, Y., Cai, L., Cheng, Q., Zhang, H. (2016). Design and manufacturing model of customized hydrostatic bearing system based on cloud and big data technology. *The International Journal of Advanced Manufacturing Technology*, vol. 84, no. 1-4, p. 261-273, **DOI:10.1007/s00170-015-8066-2**.

[7] El Khlifi, M., Souchet, D., Hajjam, M., Bouyahia, F. (2007). Numerical modeling of non-Newtonian fluids in slider bearings and channel thermohydrodynamic flow. *Journal of Tribology*, vol. 129, no. 3, p. 695-699, **DOI:10.1115/1.2736732**.

[8] Mankovits, T., Szabó, T., Kocsis, I., Páczelt, I. (2014). Optimization of the shape of axi-symmetric rubber bumpers. *Strojniški vestnik - Journal of Mechanical Engineering*, vol. 60, no. 1, p. 61-67, **DOI:10.5545/sv-jme.2013.1315**.

[9] Gustafsson, T., Rajagopal, K.R., Stenberg, R., Videman, J. (2015). Nonlinear Reynolds equation for hydrodynamic lubrication. *Applied Mathematical Modelling*, vol. 39, no. 17, p. 5299-5309, **DOI:10.1016/j.apm.2015.03.028**.

[10] Yang, Q., Huang, P., Fang, Y. (2016). A novel Reynolds equation of non-Newtonian fluid for lubrication simulation. *Tribology International*, vol. 94, p. 458-463, **DOI:10.1016/j.triboint.2015.10.011**.

[11] Masjedi, M, Khonsari, M.M. (2015). On the effect of surface roughness in point-contact EHL: Formulas for film thickness and asperity load. *Tribology International*, vol. 82, part A, p. 228-244, **DOI:10.1016/j.triboint.2014.09.010**.

[12] Deresse, G.A., Sinha, P. (2011). THD analysis for finite slider bearing with roughness: special reference to load generation in parallel sliders. *Acta Mechanica*, vol. 222, no. 1-2, p. 1-15, **DOI:10.1007/s00707-011-0515-x**.

[13] Cai, L., Wang, Y., Liu, Z., Cheng, Q. (2015). Carrying capacity analysis and optimizing of hydrostatic slider bearings under inertial force and vibration impact using finite difference method (FDM). *Journal of Vibroengineering*, vol. 17, no. 6, p. 2781-2794.

[14] Weißbacher, C., Schellnegger, C:, John, A., Buchgraber, T., Pscheidt, W. (2014). Optimization of journal bearing profiles with respect to stiffness and load-carrying capacity. *Journal of Tribology*, vol. 136, no. 3, p. 031709, **DOI:10.1115/1.4027399**.

[15] Cheng, Q., Zhan, C., Liu, Z., Zhao, Y., Gu, P. (2015). Sensitivity-based multidisciplinary optimal design of a hydrostatic rotary table with particle swarm optimization. *Strojniški vestnik - Journal of Mechanical Engineering*, vol. 61, no. 7-8, p. 432-447, **DOI:10.5545/sv-jme.2015.2478**.

[16] Chang, S.H., Jeng, Y.R. (2013). A modified particle swarm optimization algorithm for the design of a double-pad aerostatic bearing with a pocketed orifice-type restrictor. *Journal of Tribology*, vol. 136, no. 2, p. 021701, **DOI:10.1115/1.4026061**.

[17] Chan, C.-W. (2015). Modified particle swarm optimization algorithm for multi-objective optimization design of hybrid journal bearings. *Journal of Tribology*, vol. 137, no. 2, p. 021101, **DOI:10.1115/1.4028606**.

[18] Soltani-Mohammadi, S., Safa, M., Mokhtari, H. (2016). Comparison of particle swarm optimization and simulated annealing for locating additional boreholes considering combined variance minimization. *Computers & Geosciences*, vol. 95, p. 146-155, **DOI:10.1016/j.cageo.2016.07.020**.

[19] Zheng, Y.-x., Liao, Y. (2016). Parameter identification of nonlinear dynamic systems using an improved particle swarm optimization. *Optik - International Journal for Light and Electron Optics*, vol. 127, no. 19, p. 7865-7874, **DOI:10.1016/j.ijleo.2016.05.145**.

[20] Srisha Rao, M.V., Jagadeesh, G. (2010). Vector evaluated particle swarm optimization (VEPSO) of supersonic ejector for hydrogen fuel cells. *Journal of Fuel Cell Science and Technology*, vol. 7, no. 4, p. 041014, **DOI:10.1115/1.4000676**.

[21] Flocker, F.W., Bravo, R.H. (2016). On global convergence in design optimization using the particle swarm optimization technique. *Journal of Mechanical Design*, vol. 138, no. 8, p. 081402, **DOI:10.1115/1.4033727**.

[22] Tang, D., Dai, M., Salido, M.A., Giret, A. (2016). Energy-efficient dynamic scheduling for a flexible flow shop using an improved particle swarm optimization. *Computers in Industry*, vol. 81, p. 82-95, **DOI:10.1016/j.compind.2015.10.001**.

[23] Luo, W., Sun, J., Bu, C., Liang, H. (2016). Species-based particle swarm optimizer enhanced by memory for dynamic optimization. *Applied Soft Computing*, vol. 47, p. 130-140, **DOI:10.1016/j.asoc.2016.05.032**.

[24] Liu, Z., Wang, Y., Cai, L., Zhao. Y., Cheng, Q., Dong, X. (2017). A review of hydrostatic bearing system: Researches and applications. *Advances in Mechanical Engineering*, vol. 9, no. 10, p. 1-27, **DOI:10.1177/1687814017730536**.

Strojniški vestnik - Journal of Mechanical Engineering 64(2018)2, 105-113
DOI:10.5545/sv-jme.2017.5048
Original Scientific Paper
Received for review: 2017-11-04
Received revised form: 2018-01-08
Accepted for publication: 2018-01-24

Compressive Response Determination of Closed-Cell Aluminium Foam and Linear-Elastic Finite Element Simulation of μCT-Based Directly Reconstructed Geometrical Models

Tamás Mankovits[1,*] – Tamás Antal Varga[1] – Sándor Manó[2] – Imre Kocsis[1]

[1] University of Debrecen, Faculty of Engineering, Hungary
[2] University of Debrecen, Faculty of Medicine, Hungary

The development of an efficient procedure for three-dimensional modelling and finite element simulation of metal foams remains one of the greatest challenges for engineers. The numerical determination of compressive properties of foam structure is a demanding engineering task and is indispensable for design purposes. In the design of load-bearing metal foam structures, the elastic behaviour under working circumstances must be considered and for the engineering calculations on the actual foam structure its precise geometrical modelling is necessary. Closed-cell aluminium foam produced from Duralcan F3.S.20S metal matrix composite (MMC) and fabricated by direct foaming technique is analysed. To ensure full comparability, specimens are characterized according to the ruling standard for compression test for porous materials. In this paper, a manual geometrical reconstruction process based on evaluation of images given by X-ray computed tomography and the related finite element calculations is introduced. The proposed procedure is capable of investigating the actual structure as a three-dimensional problem from any kind of material that can be analysed on the basis of computed tomography (CT) images. The geometrical reconstruction and the finite element calculation results show good correlation with the measured values in the elastic, which proves the utility of the presented method.

Keywords: closed-cell foam, geometrical reconstruction, compression test, finite element method

Highlights

- *Foam structure produced from Duralcan F3.S20S MMC is analysed experimentally and numerically.*
- *Manual geometric reconstruction of closed-cell foam structures is presented.*
- *Finite element calculations of the actual geometry of foam structures are executed.*
- *Calculations based on geometrical model precisely described the compressive response in the elastic region.*

0 INTRODUCTION

Metal foams have a lightweight cellular structure with excellent mechanical and physical properties. It is well known that metal foams have high compression strength combined with good energy absorption characteristics [1]. Therefore, the interest in these materials is widespread not only as a vibration damper or sound absorber but also as a load-bearing structural element. Numerous applications rely on the compressive property of metal foams, which directly depend on its structure. As a load-bearing structural element (e.g. vehicle part, biomedical implant) metal foam is expected to behave elastically under working circumstances, so the material response must be predicted precisely in the elastic region. Numerical determination of compressive properties of foam structure remains a demanding engineering task, and it is indispensable for design purposes.

A number of studies have reported on measuring the material response of different types of metal foams in destructive ways. The compressive properties of open cell metal foams in [2] and [3], metal matrix syntactic foams in [4] to [8], and titanium foam in [9] were investigated, while the elastic behaviour of closed-cell aluminium foam under uniaxial loading and bending conditions was also studied in [10].

Geometrical modelling is an essential part of the procedure aiming the investigation of metal foam structures in a numerical way. Numerous approaches can be found in the literature for the proper description of foam structures, one of which is the usage of uniform cell models which results in simplified geometry compared with the actual structure. A combination of spherical and cruciform-shaped cells was used to model closed-cell aluminium foam and to simulate its material response in [11], while different uniform cell structures were applied to the model and simulate open cell metal foams in [12] to [14]. Diamond and cubic cell foam structure were also used to simulate the effect of cell shape on the mechanical behaviour of open cell metal foams in [15].

Since the inner structure of different types of metal foams is quite complicated, a surface analysis can result in imperfect or false data. Recent studies proved X-ray computed tomography to be an efficient and powerful tool for mapping the complete structure

*Corr. Author's Address: University of Debrecen, Faculty of Engineering, Ótemető 2-4, H-4028 Debrecen, Hungary, tamas.mankovits@eng.unideb.hu

of materials in a non-invasive and non-destructive way.

The development of a mesoscale simulation modelling voids and sintered hollow spheres as a metal foam structure was presented in [16]. 3D models of microporous ceramics were generated, and the determination of the porosity was studied in [17]. Two-dimensional models based on μCT images were established to investigate mechanical properties of different foam structures in [18] to [24]. An overview of the auxetic cellular materials was presented in [25].

A new CAD modelling procedure applied to a circular foam billet was proposed, and the structure was obtained, introducing spherical surfaces, which represented the internal voids of an aluminium foam in [26]. The linear elastic properties were determined by the usage of finite element method based on random tessellations for the generation of microstructure in [27], and geometrical reconstruction processes of open cell foam structures were investigated in [28] and [29]. Randomly shaped Voronoi polyhedrals were used to form the pore network of open cell titanium foam and finite element prediction of the compressive characteristics was presented in [30]. A finite element model was introduced for the determination of mechanical properties of non-uniform cellular aluminium in [31]. A random number generator was established to model the proper distribution of the hollow spheres, and finite element simulation was performed to determine the compressive material response of metal matrix syntactic foams in [32]. Syntactic foam structure was analysed and the three-dimensional CAD model was established in [33]. Three mesh generating methods (Voronoi description of the microstructure, voxel meshes, and tetrahedral meshes) using tomographic images of the actual shape of cellular structures were investigated in [34]. The exact geometrical data of single sintered metallic hollow spheres were obtained by CT scanning, and the corresponding finite element models were created in [35]. Advanced pore morphology (APM) foam elements were investigated and compressive force-displacement response was evaluated numerically in [36].

Three-dimensional models were generated based on μCT images and numerical calculations were performed on cellular structures in [37] and [38]. The local deformation mechanisms of the actual foam structure during compression were investigated using different mesh size discretizations in [39]. Closed-cell aluminium foams in [40] and [41] and open cell aluminium foams in [42] to [44] were investigated numerically based on μCT images and the material response for compression was determined. The deformation and plastic collapse mechanisms of closed-cell aluminium foams were analysed with finite element method based on μCT. The geometrical reconstruction was performed with software RapidForm™ in [45]. The 3D geometry of closed-cell aluminium foam derived from the synthesis of digital cross-section images was used to build the finite element model simulating the deformation conditions of the foam under micro-tension loads and compression in [46] and [47]. The strain rate-dependent compression response of Ni-foam was determined by the finite element method based on μCT images in [48]. A novel reconstruction method with Matlab image processing and CT scanning was applied and the finite element method was used to determine the thermal conductivity and the material response of a closed-cell aluminium foam in [49] and [50].

The number of publications in the field of geometrical modelling and finite element analysis of metal foam structures demonstrates that this topic is in the focus of studies. To obtain high-quality predictions of a porous material response, it is critical to constructing FEM models that provide an adequate description of the actual geometry. In this research, a geometrical reconstruction of closed-cell aluminium foam and finite element analysis of the structure in the elastic region is presented. The deviation between the simulation and measurement results is not significant, proving that the method is suitable for the description of real structures.

An essential part of the procedure is a manual reconstruction method for objects of complex geometry. The first step is the preparation of plane sections (CT images) with parallel planes of given density. The second is the performance of a series of transformations providing a geometrically accurate three-dimensional object that is suitable for finite element analysis. The investigation of specimens proves that the accuracy of the proposed reconstruction method meets the requirements and the procedure can be reproduced and validated.

1 MATERIALS AND EXPERIMENTAL METHODS

The examined closed-cell aluminium foam was produced from Duralcan F3S.20S Metal Matrix Composite and fabricated using a direct foaming technique by adding blowing agent. Considering the finite element investigations, the relevant physical and mechanical properties of the solid phase were measured [51]. The chemical composition was also evaluated with EDX analysis and compared with the

data available in the literature. The density of the raw material was measured. The SiC median particle size was determined by microscopic analysis using a Hitachi Tabletop 3030 SEM microscope. According to the ASTM E9-09 standard [52], the modulus of elasticity was evaluated by compression test using an INSTRON 8874 testing machine. The diameter and the length of the solid specimens were 13 mm and 25 mm, respectively. The measuring results listed in Table 1 showed good conformity with the commercial data. Several physical and mechanical properties of the three specimens were investigated. According to the measurement data, porosity of pieces showed low variability.

Table 1. *Chemical composition and related physical and mechanical properties of the applied matrix material*

Main components	Commercial and literature data [53]	Measured data
Al [wt%]	68.53	69.26
Si [wt%]	9.3	9.21
Mg [wt%]	0.55	0.53
SiC [wt%]	21.4	20.8
other [wt%]	0.22	0.2
Properties		
SiC median particle size [mm]	12.8	13.24
Density [kg/m^3]	2850	2875.12
Modulus of elasticity [GPa]	98.6	97.2

The size of the specimens was determined according to the ISO 13314 standard on the basis of a statistical analysis of the pore sizes. Similar investigations were published in [51] by the authors. The size of the specimens was 14.5 mm × 14.5 mm × 14.5 mm (see Fig. 1); STRUERS Labotom-15 was used for cutting.

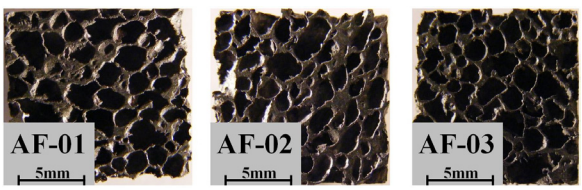

Fig. 1. *Closed-cell aluminium foam specimens*

The compression tests were performed on an INSTRON 8874 type universal testing machine at room temperature. The compression tests were carried out with the application of lubricant. The deformation rate was maintained in quasi-static condition at 8.7 mm/min. During the tests, the engineering stress-engineering strain curves were registered and processed according to the ruling standard for the compression test for porous and cellular materials [54].

The basis of the geometrical reconstruction was the microcomputed-tomography analysis that was performed using a YXILON CT Modular type industrial CT equipment with X-ray tube of 225 kV and resolution of 7 mm.

Using Materialise Mimics v10.1 and its complement Materialise Magics v9.9, the reconstruction of the geometry of the samples were established through some manual steps. The automatic reconstruction was compared with the manual reconstruction process, and the results of the proposed process were qualified. An evaluation copy of VGStudio Max 3.0 was used to control the quality of the geometric reconstruction; the original structure was compared with the reconstructed one. The finite element calculations with Femap 9.3 was used to generate load-displacement curves in the elastic region. The results showed excellent correlation with the compression tests.

2 RESULTS AND DISCUSSION

2.1 Compressive Properties

The compressive properties of the three aluminium foam specimens were determined at a constant loading speed of 8.7 mm/min according to the standard [54]. The standard introduces several important terms to evaluate the behaviour and compressive properties of metal foams and cellular metallic materials. The most important ones are plateau stress (average stress between 20 % and 40 % compressive strain); quasi-

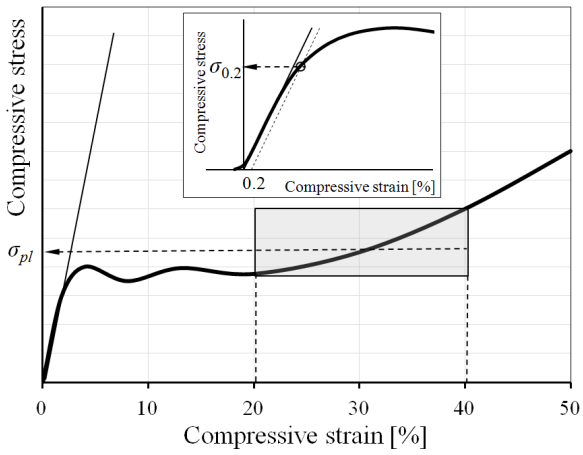

Fig. 2. *Determination of the plateau stress (σpl), the quasi-elastic gradient and the compressive offset stress (σ0.2) based on ISO 13314:2011*

elastic gradient (gradient of the straight line within the linear deformation region at the beginning of the compressive stress-strain curve); compressive offset stress (compressive stress at the plastic compressive strain of 0.2 %), see Fig. 2.

The compressive stress-strain curve of the investigated specimens can be seen in Fig. 3. The compressive offset stress, the quasi-elastic gradient and the plateau stress were calculated from the compressive stress-strain curves.

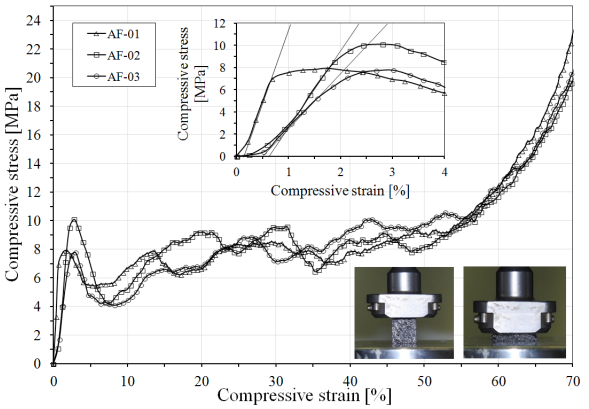

Fig. 3. *Compressive stress-strain curve of foam specimens*

The results of the compression tests are listed in Table 2.

Table 2. *Compressive properties of the aluminium foam specimens*

Compressive properties	AF-01	AF-02	AF-03
Compressive offset stress [MPa]	7.434	9.760	7.332
Quasi-elastic gradient [MPa]	1295	738.9	500.5
Plateau stress [MPa]	7.757	8.085	8.355

Table 2 shows that significant deviation of plateau stresses cannot be observed, while the elastic properties (compressive offset stress and quasi-elastic gradient) are different. Considering the specific structure of the closed-cell metal foams, it can be supposed that the elastic properties primarily depend on the porosity, the distribution of the cell volume (described by quartiles, Q_1, Q_2, Q_3), the sum of the cell volumes in the failure zone (V_C) and the area of the surfaces (A_C) contacting the compression plates. The porosity evaluation was based on weight and volume measurements. Foam structure analysis was carried out with VGStudio Max 3.0, and the extents of the contact surface were determined by image processing analysis. The measurement results are listed in Table 3. During the compression test, it is obtained that the failure starts in the middle section of the specimens.

Table 3. *Structural properties of the aluminium foam specimens*

	AF-01	AF-02	AF-03
Porosity [%]	85.16	85.4	85.38
Mass [g]	1.33	1.36	1.34
Q_1	0.28	0.35	0.31
Q_2	0.72	0.91	0.82
Q_3	1.94	2.12	2.24
V_C [mm³]	211.93	189.64	204.45
A_C [%]	41.39	47.48	50.27

According to Table 3, the structural properties of the aluminium foam, depending on the manufacturing technology, show no significant deviation, while the extent of contact surfaces is highly influenced by the position of the cutting planes. Furthermore, a significant variance can be detected in the sum cell volumes in the failure zone. Because of the deviation of the elastic properties (Fig. 3), a finite element analysis is necessary in the elastic sector. According to our investigations, the extent of the contact surfaces and the elastic properties seem to be related, but further research is necessary to obtain a more precise connection.

2.2 Geometrical Reconstruction Process

The basis of the procedure is a series of CT images in DICOM format that is converted into an image stack, the input of the software that provides the structure in STL format. Transformations of this structure yield a format (IGES, NAS, etc.) that is suitable for further engineering calculations.

The accuracy of the finite element calculations highly depends on the deviation between the original and the reconstructed geometry.

Finding the connecting points of cell walls requires sharp contours between phases in section images. The contours in CT images used in the investigation can be detected with high accuracy, but the images contain noise because of the imaging technique.

The accuracy of the reconstruction also depends on the distance between slicing planes, which affects the minimum level of the detectable cell size and on the complexity of cell wall surfaces (a non-smooth surface and a deviation from sphere reduce the accuracy of the reconstruction).

Materialise Mimics v10.1 is used for the reconstruction process; this software allows the automatic reconstruction, which results in a model that is suitable for finite element analysis, but the accuracy of the geometrical conformity is not high

enough. Instead of an automatic reconstruction process, the software allows custom parameter setting defined by the user in each step of the transformation. The order of transformations can be chosen resulting in different model properties. The transformations provide STL files with different properties, e.g. mass, volume, number of elements. Fig. 4. shows the order of transformations that was proved to be the best for approximation in the modelling of closed-cell aluminium foams (the figure contains the original command names used in Mimics).

The five steps of the parameterized transformation resulted in 3.79×10^6, 3.58×10^6, 3.54×10^6 elements, while the automatic transformation led to a model of 9.10×10^6, 8.81×10^6, 6.88×10^6 elements, respectively. The total mass [g] after the parameterized transformation (1.3454, 1.3826, 1.3864) was close to the initial value (1.3509, 1.3762, 1.3660), while the total mass in the case of automatic reconstruction was 1.55, 1.53, 1.58, respectively, that is, significantly higher than the initial values.

The accuracy of geometry was checked by comparing the foam model provided by the reconstruction process with the model described by the STL file using the evaluation copy of VGStudio Max 3.0. The comparison resulted in a statistical evaluation of deviations. The regions where the deviation was significant were investigated to determine the accuracy of the given geometrical model. The ratio of surface values in the domain where the deviation between the initial and the transformed foam structure is greater than 0.02 mm is listed in Table 4.

Table 4. *Ratio of surface values where the deviation is greater than 0.02 mm*

	AF-01	AF-02	AF-03
Ratio [%] - automatic	1.703	1.293	1.290
Ratio [%] - parameterized	0.581	0.613	0.468

According to the analysis, the ratio of the surface where the deviation is greater than 0.02 mm was more than two times higher in the case of automatic reconstruction compared to the parameterized case. The image provided by the software enables the detailed investigation of high deviations. Fig. 5 shows a 2 mm × 2 mm × 2 mm size foam part; two details are highlighted where the two models differ.

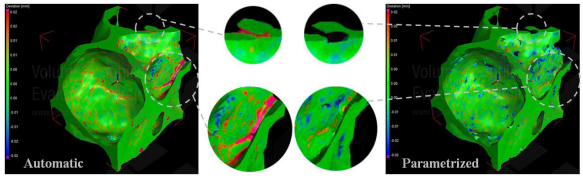

Fig. 5. *Detailed investigation using the images provided by the software*

Fig. 6 shows the complete modelling procedure in pictures: manufactured specimen, CT scanned image, image-stack, initial STL structure, reconstructed STL structure, meshed foam model and finite element evaluation. The benefit of the proposed procedure is the high precision preparation of the foam structure attained by the custom parameterized reconstruction method.

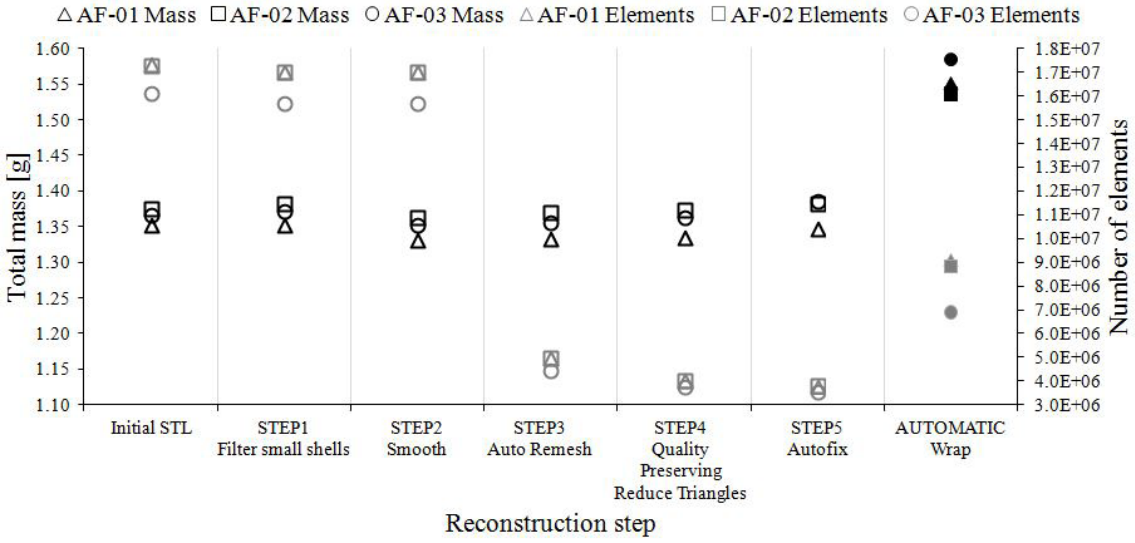

Fig. 4. *Comparison of the automatic and the parameterized processes (total volume, number of elements)*

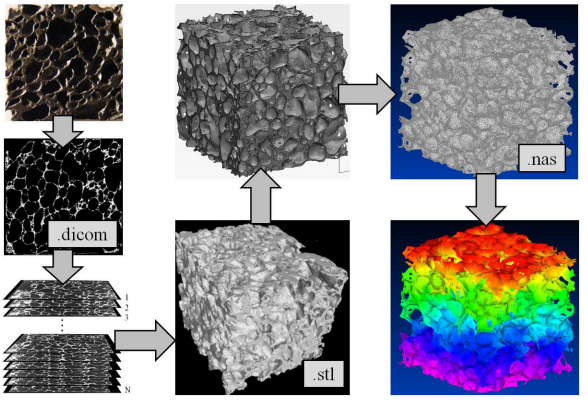

Fig. 6. *Complete modelling procedure*

2.3 Finite Element Calculations

The computational models were prepared to represent the experimental setup, and each consisted of an aluminium foam specimen and two rigid plates. Frictionless contact was assumed and used in the model. The rigid top plate had a prescribed displacement, and the bottom plate was fixed and used to measure the reaction force. The aluminium foam specimens were meshed with tetrahedron elements, and material properties were determined using experiments by the authors [51]. The properties of the finite element models are listed in Table 5. The computational models were analysed using the commercial finite element software Femap 9.3 with NX Nastran solver for quasi-static loading.

Table 5. *Properties of the finite element models*

	AF-01	AF-02	AF-03
Number of volume elements	6228541	5916312	5885768
Number of nodes	1852991	1759080	1744979
Largest volume element [mm³]	0.1661	0.05099	0.1342

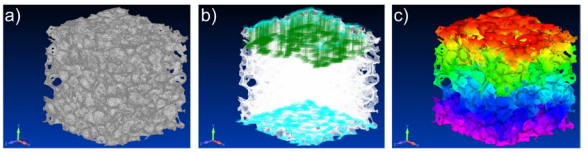

Fig. 7. *a) The meshed model, b) the boundary conditions, and c) the displacement state of a foam specimen*

The finite element settings and the simulation results are shown in Figs. 7 and 8 and listed in Table 6.

The finite element calculations correlated with the experimental results. For design purposes, the specification of the elastic behaviour of metal foam structural parts is indispensable. The finite element model can describe this feature on the basis of the accurate geometrical reconstruction.

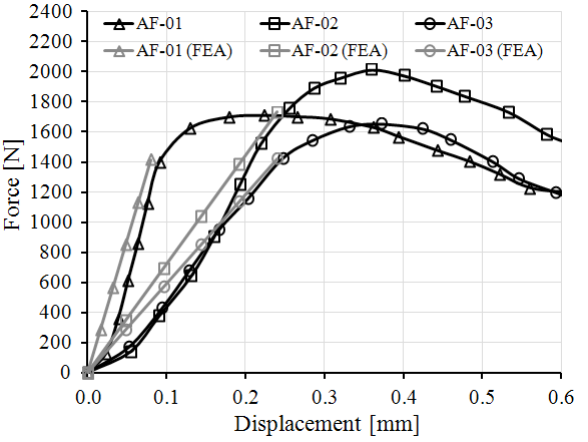

Fig. 8. *The real and the simulated force-displacement curves of the aluminium foam under quasi-static loading*

Table 6. *Comparison of the measured and simulated Quasi-elastic gradients in MPa*

	AF-01	AF-02	AF-03
Measurement	1295	738.9	500.5
Simulation	1243.4	689.7	476.3
Difference [%]	3.984	6.658	4.835

3 CONCLUSIONS

In the framework of the study, experimental and numerical analysis were conducted to clarify the elastic behaviour of metal foam. Closed-cell aluminium foams were compressed, and stress-strain curves were analysed. A deviation occurred in the elastic properties of foam specimens, which originated in the actual geometrical properties. For the numerical determination of elastic properties of the closed-cell aluminium foams, a manual geometrical reconstruction procedure was presented. This process was realized in several custom parameterized steps and resulted in a more accurate model than the automatic reconstruction used generally. The difference between the two procedures was proved with comparison analysis. The original image-stack was transformed into the form that is suitable for finite element simulations. The finite element calculations correlated with the experimental results and the numerical model precisely described the elastic behaviour of the investigated foam on the basis of the accurate geometrical reconstruction. The procedure can support the design process of load-bearing metal foam parts.

4 ACKNOWLEDGEMENTS

This research was supported by the ÚNKP-4 New National Excellence Program of the Ministry of Human Capacities of Hungary.

The authors would like to thank the Department of Materials Science and Technology, Széchenyi István University for the microcomputed tomography records.

5 REFERENCES

[1] Ashby, M.F., Evans, A.G., Fleck, N.A., Gibson, L.J. (2000). *Metal Foams: A Design Guide*. Butterworth-Heinemann, Woburn.

[2] Devivier, C., Tagliaferri, V., Trovalusci, F., Ucciardello, N. (2015). Mechanical characterization of open cell aluminium foams reinforced by nickel electro-deposition. *Materials and Design*, vol. 86, p. 272-278, **DOI:10.1016/j.matdes.2015.07.078**.

[3] Xiao, L., Song, W., Tang, H., Zhu, Z., Wang, J., Wang, H. (2015). High temperature compression properties of open-cell Ni–20Cr foams produced by impregnation. *Materials and Design*, vol. 85, p. 47-53, **DOI:10.1016/j.matdes.2015.06.167**.

[4] Orbulov, I.N., Májlinger, K. (2013). Description of the compressive response of metal matrix syntactic foams. *Materials and Design*, vol. 49, p. 1-9, **DOI:10.1016/j.matdes.2013.02.007**.

[5] Orbulov, I.N. (2012). Compressive properties of aluminium matrix syntactic foams. *Materials Science and Engineering: A*, vol. 555, p. 52-56, **DOI:10.1016/j.msea.2012.06.032**.

[6] Peroni, L., Scapin, M., Avalle, M., Weise, J., Lehmhus, D., Baumeister, J., Busse, M. (2012). Syntactic iron foams – on deformation mechanisms and strain-rate dependence of compressive properties. *Advanced Engineering Materials*, vol. 14, no. 10, p. 909-918, **DOI:10.1002/adem.201200160**.

[7] Luong, D.D., Shunmugasamy, V.C., Gupta, N., Lehmhus, D., Weise, J., Baumeister, J. (2015). Quasi-static and high strain rates compressive response of iron and Invar matrix syntactic foams. *Materials and Design*, vol. 66, part B, p. 516-531, **DOI:10.1016/j.matdes.2014.07.030**.

[8] Peroni, L., Scapin, M., Fichera, C., Lehmhus, D., Weise, J., Baumeister, J., Avalle, M. (2014). Investigation of the mechanical behaviour of AISI 316L stainless steel syntactic foams at different strain-rates. *Composites Part B: Engineering*, vol. 66, p. 430-442, **DOI:10.1016/j.compositesb.2014.06.001**.

[9] Pałka, K., Adamek, G., Jakubowicz, J. (2016). Compression behavior of Ti Foams with spherical and polyhedral pores. *Advanced Engineering Materials*, vol. 18, no. 8, p. 1511-1518, **DOI:10.1002/adem.201600169**.

[10] Triawan, F., Kishimoto, K., Adachi, T., Inaba, K., Nakamura, T., Hashimura, T. (2012). The elastic behavior of aluminum alloy foam under uniaxial loading and bending conditions. *Acta Materialia*, vol. 60, no. 6-7, p. 3084-3093, **DOI:10.1016/j.actamat.2012.02.013**.

[11] Hasan, A. (2010). An improved model for FE modeling and simulation of closed cell Al-alloy foams. *Advances in Materials Science and Engineering*, article ID 567390, **DOI:10.1155/2010/567390**.

[12] Kou, D.P., Li, J.R., Yu, J.L., Cheng, H.F. (2008). Mechanical behavior of open-cell metallic foams with dual-size cellular structure. *Scripta Materialia*, vol. 59, no. 5, p. 483-486, **DOI:10.1016/j.scriptamat.2008.04.022**.

[13] Jang, W.Y., Kyriakides, S., Kraynik, A.M. (2010). On the compressive strength of open-cell metal foams with Kelvin and random cell structures. *International Journal of Solids and Structures*, vol. 47, no. 21, p. 2872-2883, **DOI:10.1016/j.ijsolstr.2010.06.014**.

[14] Lu, Z.X., Liu, Q., Huang, J.X. (2011). Analysis of defects on the compressive behaviors of open-cell metal foams through models using the FEM. *Materials Science and Engineering: A*, vol. 530, p. 285-296, **DOI:10.1016/j.msea.2011.09.088**.

[15] An, Y., Wen, C., Hodgson, P.D., Yang, C. (2012). Investigation of cell shape effect on the mechanical behaviour of open-cell metal foams. *Computational Materials Science*, vol. 55, p. 1-9, **DOI:10.1016/j.commatsci.2011.11.030**.

[16] Smith, B.H., Szyniszewski, S., Hajjar, J.F., Schafer, B.W., Arwade, S.R. (2012). Characterization of steel foams for structural components. *Metals*, vol. 2, no. 4, p. 399-410, **DOI:10.3390/met2040399**.

[17] Schmidt, K., Becker, J. (2012). Generating validated 3D models of microporous ceramics. *Advanced Engineering Materials*, vol. 15, no. 1-2, p. 40-45, **DOI:10.1002/adem.201200097**.

[18] Shen, H., Brinson, L.C. (2007). Finite element modeling of porous titanium. International *Journal of Solids and Structures*, vol. 44, no. 1, p. 320-335, **DOI:10.1016/j.ijsolstr.2006.04.020**.

[19] Kádár, Cs., Maire, E., Borbély, A., Peix, G., Lendvai, J., Rajkovits, Zs. (2004). X-ray tomography and finite element simulation of the indentitation behavior of metal foams. *Materials Science and Engineering: A*, vol. 387-389, p. 321-325, **DOI:10.1016/j.msea.2004.03.091**.

[20] Zhu, X., Ai, S., Fang, D., Liu, B., Lu, X. (2014). A novel modeling approach of aluminum foam based on MATLAB image processing. *Computational Materials Science*, vol. 82, p. 451-456, **DOI:10.1016/j.commatsci.2013.10.020**.

[21] Adziman, M.F., Deshpande, S., Omiya, M., Inoue, H., Kishimoto, K. (2007). Compressive deformation in aluminum foam investigated using a 2D object oriented finite element modeling approach. *Key Engineering Materials*, vol. 353-358, p. 651-654, **DOI:10.4028/www.scientific.net/KEM.353-358.651**.

[22] Vendra, L., Rabiei, A. (2010). Evaluation of modulus of elasticity of composite metal foams by experimental and numerical techniques. *Materials Science and Engineering: A*, vol. 527, no. 7-8, p. 1784-1790, **DOI:10.1016/j.msea.2009.11.004**.

[23] Caty, O., Maire, E., Youssef, S., Bouchet, R. (2008). Modeling the properties of closed-cell cellular materials from tomography images using finite shell elements. *Acta Materialia*, vol. 56, no. 19, p. 5524-5534, **DOI:10.1016/j.actamat.2008.07.023**.

[24] Storm, J., Abendroth, M., Emmel, M., Liedke, T., Ballaschk, U., Voigt, C., Sieber, T., Kuna, M. (2013). Geometrical modelling of foam structures using implicit functions. *International Journal of Solids and Structures*, vol. 50, no. 3-4, p. 548-555, **DOI:10.1016/j.ijsolstr.2012.10.026**.

[25] Novak, N., Vesenjak, M., Ren, Z. (2016). Auxetic cellular materials – a Review. *Strojniski vestnik – Journal of Mechanical Engineering*, vol. 62, no. 9, p. 485-493, **DOI:10.5545/sv-jme.2016.3656**.

[26] Filice, L., Gagliardi, F., Umbrello, D. (2009). Simulation of aluminum foam behavior in compression tests. *The Arabian Journal for Science and Engineering*, vol. 34, no. 1C, p. 129-137.

[27] Geißendörfer, M., Liebscher, A., Proppe, C., Redenbach, C., Schwarzer, D. (2014). Stochastic multiscale modeling of metal foams. *Probabilistic Engineering Mechanics*, vol. 37, p. 132-137, **DOI:10.1016/j.probengmech.2014.06.006**.

[28] Vesenjak, M., Veyhl, C., Fiedler, T. (2012). Analysis of anisotropy and strain rate sensitivity of open-cell metal foam. *Materials Science and Engineering: A*, vol. 541, p. 105-109, **DOI:10.1016/j.msea.2012.02.010**.

[29] Zhang, T., Maire, E., Adrien, J., Onck, P.R., Salvo, L. (2013). Local tomography study of the fracture of an ERG metal foam. *Advanced Engineering Materials*, vol. 15, no. 8, p. 767-772, **DOI:10.1002/adem.201300004**.

[30] Siegkas, P., Tagarielli, V., Petrinic, N. (2014). Modelling stochastic foam geometries for FE simulations using 3D Voronoi cells. *Procedia Materials Science*, vol. 4, p. 221-226, **DOI:10.1016/j.mspro.2014.07.604**.

[31] Foroughi, B., Degischer, H.P., Kottar, A. (2013). Characterization and simulation of tensile deformation of non-uniform cellular aluminium until damage. *Advanced Engineering Materials*, vol. 15, no. 4, p. 276-286, **DOI:10.1002/adem.201200163**.

[32] Szlancsik, A., Katona, B., Bobor, K., Májlinger, K., Orbulov, I.N. (2015). Compressive behaviour of aluminium matrix syntactic foams reinforced by iron hollow spheres. *Materials and Design*, vol. 83, p. 230-237, **DOI:10.1016/j.matdes.2015.06.011**.

[33] Kozma, I., Zsoldos, I., Dorogi, G., Papp, S. (2014). Computer tomography based reconstruction of metal matrix syntactic foams. *Periodica Polytechnica Mechanical Engineering*, vol. 58, no. 2, p. 87-91, **DOI:10.3311/PPme.7337**.

[34] Maire, E., Fazekas, A., Salvo, L., Dendievel, R., Youssef, S., Cloetens, P., Letang, J.M. (2003). X-ray tomography applied to the characterization of cellular materials. Related finite element modeling problems. *Composites Science and Technology*, vol. 63, no. 16, p. 2431-2443, **DOI:10.1016/S0266-3538(03)00276-8**.

[35] Borovinšek, M., Vesenjak, M., Ren, Z. (2016). Estimating the base material properties of sintered metallic hollow spheres by inverse engineering procedure. *Mechanics of Materials*, vol. 100, p. 22-30, **DOI:10.1016/j.mechmat.2016.06.001**.

[36] Sulong, M.A., Vesenjak, M., Belova, I.V., Murch, G.E., Fiedler, T. (2014). Compressive properties of Advanced Pore Morphology (APM) foam elements. *Materials Science and Engineering: A*, vol. 607, p. 498-504, **DOI:10.1016/j.msea.2014.04.037**.

[37] Doroszko, M., Seweryn, A. (2015). Numerical modeling of the tensile deformation process of sintered 316L based on microtomography of porous mesostructures. *Materials and Design*, vol. 88, p. 493-504, **DOI:10.1016/j.matdes.2015.09.006**.

[38] Jirousek, O., Doktor, T., Kytýř, D., Zlámal, P., Fíla, T., Koudelka, P., Jandejsek, I., Vavřík, D. (2013). X-ray and finite element analysis of deformation response of closed-cell metal foam subjected to compressive loading. *Journal of Instrumentation*, vol. 8, p. 1-4, **DOI:10.1088/1748-0221/8/02/C02012**.

[39] Youssef, S., Maire, E., Gaertner, R. (2005). Finite element modelling of the actual structure of cellular materials determined by X-ray tomography. *Acta Materialia*, vol. 53, no. 3, p. 719-730, **DOI:10.1016/j.actamat.2004.10.024**.

[40] Saadatfar, M., Mukherjee, M., Madadi, M., Schröder-Turk, G.E., Garcia-Moreno, F., Schaller, F.M., Hutzler, S., Sheppard, A.P., Banhart, J., Ramamurty, U. (2012). Structure and deformation correlation of closed-cell aluminium foam subject to uniaxial compression. *Acta Materialia*, vol. 60, no. 8, p. 3604-3615, **DOI:10.1016/j.actamat.2012.02.029**.

[41] Hangai, Y., Yamaguchi, R., Takahashi, S., Utsunomiya, T., Kuwazuru, O., Yoshikawa, N. (2013). Deformation behavior estimation of aluminum foam by X-ray CT image-based finite element analysis. *Metallurgical and Materials Transactions: A*, vol. 44, no. 4, p. 1880-1887, **DOI:10.1007/s11661-012-1532-7**.

[42] Veyhl, C., Belova, I.V., Murch, G.E., Fiedler, T. (2011). Finite element analysis of the mechanical properties of cellular aluminium based on micro-computed tomography. *Materials Science and Engineering: A*, vol. 528, no. 13-14, p. 4550-4555, **DOI:10.1016/j.msea.2011.02.031**.

[43] Michailidis, N., Stergioudi, F., Omar, H., Papadoupoulos, D., Tsipas, D.N. (2011). Experimental and FEM analysis of the material response of porous metals imposed to mechanical loading. *Colloids and Surfaces A: Physicochemical and Engineering Aspects*, vol. 382, no. 1-3, p. 124-131, **DOI:10.1016/j.colsurfa.2010.12.017**.

[44] Ramírez, J.F., Cardona, M., Velez, J.A., Mariaka, I., Isaza, J.A., Mendoza, E., Betancourt, S., Fernández-Morales, P. (2014). Numerical modeling and simulation of uniaxial compression of aluminum foams using FEM and 3D-CT images. *Procedia Materials Science*, vol. 4, p. 227-231, **DOI:10.1016/j.mspro.2014.07.609**.

[45] Jeon, I., Asahina, T., Kang, K.J., Im, S., Lu, T.J. (2010). Finite element simulation of the plastic collapse of closed-cell aluminum foams with X-ray computed tomography. *Mechanics of Materials*, vol. 42, no. 3, p. 227-236, **DOI:10.1016/j.mechmat.2010.01.003**.

[46] Michailidis, N., Stergioudi, F., Omar, H., Tsipas, D.N. (2010). An image-based reconstruction of the 3D geometry of an Al open-cell foam and FEM modeling of the material response. *Mechanics of Materials*, vol. 42, no. 2, p. 142-147, **DOI:10.1016/j.mechmat.2009.10.006**.

[47] Michailidis, N., Stergioudi, F., Omar, H., Tsipas, D.N. (2010). FEM modeling of the response of porous Al in compression. *Computational Materials Science*, vol. 48, no. 2, p. 282-286, **DOI:10.1016/j.commatsci.2010.01.008**.

[48] Michailidis, N. (2011). Strain rate dependent compression response of Ni-foam investigated by experimental and FEM simulation methods. *Materials Science and Engineering: A*, vol. 528, no. 12, p. 4204-4208, **DOI:10.1016/j.msea.2011.02.002**.

[49] Zhu, X., Ai, S., Lu, X., Zhu, L., Liu, B. (2014). A novel 3D geometrical reconstruction method for aluminum foams and FEM modeling of the material response. *Theoretical*

and Applied Mechanics Letters, vol. 4, no. 2, p. 021006, **DOI:10.1063/2.1402106**.

[50] Zhu, X., Ai, S., Lu, X., Ling, X., Zhu, L., Liu, B. (2014). Thermal conductivity of closed-cell aluminum foam based on the 3D geometrical reconstruction. *International Journal of Heat and Mass Transfer*, vol. 72, p. 242-249, **DOI:10.1016/j.ijheatmasstransfer.2014.01.006**.

[51] Mankovits, T., Budai, I., Balogh, G., Gábora, A., Kozma, I., Varga, T.A., Manó, S., Kocsis, I. (2014). Structural analysis and its statistical evaluation of a closed-cell metal foam. *International Review of Applied Sciences and Engineering*, vol. 5, no. 2, p. 135-143, **DOI:10.1556/IRASE.5.2014.2.5**.

[52] ASTM E9-09:2009. *Standard Test Methods of Compression Testing of Metallic Materials at Room Temperature*. ASTM International, West Conshohocken, **DOI:10.1520/E0009-09**.

[53] Curle, U.A., Ivanchev, L. (2010). Wear of semi-solid rheocast SiCp/Al metal matrix composites. *Transactions of Nonferrous Metals Society of China*, vol. 20, sup. 3, p. 852-856, D**OI:10.1016/S1003-6326(10)60594-8**.

[54] ISO 13314:2011. *Mechanical Testing of Metals – Ductility Testing – Compression test for Porous and Cellular Metals*. International Organization for Standardization. Geneva.

Strojniški vestnik - Journal of Mechanical Engineering 64(2018)2, 114-120

DOI:10.5545/sv-jme.2017.5093 Original Scientific Paper
Received for review: 2017-11-16
Received revised form: 2018-01-19
Accepted for publication: 2018-02-09

The Effect of Internal Heat Exchanger Using R1234ze(E) as an Alternative Refrigerant in a Mobile Air-Conditioning System

Mehmet Direk[1,*] – Eren Soylu[2]
[1]University of Yalova, Faculty of Engineering, Turkey
[2]University of Yalova, Institute of Science and Engineering, Turkey

In this study, the use of R1234ze(E) refrigerant in an R134a-based mobile air-conditioning (MAC) system was experimentally investigated. Additionally, the effect of internal heat exchanger (IHX) on the performance of MAC was determined using R1234ze(E). Under the same conditions, we have tested and compared two different cases that use R1234ze(E) with and without an IHX by taking the performance of R134a as a reference. The inlet airflow temperatures of the evaporator and condenser were kept at 27 °C and 35 °C during the experiments, respectively. Performance parameters were determined using energy and exergy analysis. Compressor power was reduced by an average of 19 %, and the COP of R1234ze(E) were increased by an average of 4 % after activating the IHX. Moreover, it was determined that the value of exergy destruction of the system with R1234ze(E) was decreased by an average of 50 % when compared to R134a.
Keywords: R134a, R1234ze(E), mobile air conditioning, coefficient of performance, internal heat exchanger

Highlights
- *The performance of a MAC system using R134a and R1234ze(E) was tested.*
- *The effect of IHX on the system performance was determined.*
- *COP was increased by 4 % on average after IHX activated.*
- *The exergy destruction value was found to be decreased by 50 % on average in the case of R1234ze(E).*

0 INTRODUCTION

Even though R134a has low ozone depletion potential (ODP), its global warming potential (GWP) value is as high as 1300 **[1]**. Therefore, European Regulation No. 2006/40/EC and No. 517/2014 restrict the usage of HFCs which have GWP greater than 150 in MAC systems and other vapour compression refrigeration (VCR) systems **[2]** and **[3]**. Aprea et al. **[4]** experimentally investigated a refrigeration system using R1234ze(E) as a replacement of R134a. Total equivalent warming impact (TEW1) and life cycle climate performance indexes were found to be lower than R134a for all working conditions. In addition to low GWP values, R1234ze(E) has low flammability with regards considering safety issues **[5]**. Imamura et al. **[6]**, performed experiments to elucidate fire hazards of R32 and R1234ze(E). They observed that ignition could be prevented using mechanical ventilation when the level of leakage is equal to the upper flammability limit (UFL). Table 1 shows that the vapour density of R1234ze(E) is 19 %, and the latent heat is 7 % lower when compared to R134a. R1234ze(E) has a low mass flow rate per unit volume of compression and thus a lower cooling capacity. Mota-Babiloni et al. **[7]** have identified the performance parameters of a refrigeration system, which uses R134a and R1234ze(E), as the functions of different evaporator and condenser temperatures. They observed that the R1234ze(E) has lower cooling capacity and COP values by 30 % and 9 %, respectively, in comparison compared to R134a. Leighton et al. **[8]** tested R1234ze(E) as an alternative to R134a in a refrigeration system. They found that R1234ze(E) has a lower cooling capacity and COP by 21.5 % and 7.9 %, respectively.

Table 1. *Refrigerant properties of R1234ze(E) and R134a* **[1]** *and* **[9]**

Property	R134a	R1234ze(E)
ASHRAE safety classification	A1	A2L
ODP	0	0
GWP	1300	4
Critical temperature [K]	247.08	253.88
Critical pressure [kPa]	4059.28	3623.90
Vapor density [kg·m^{-3}]	14.35	11.65
Liquid density [kg·m^{-3}]	1295	1240
Latent heat of vaporization [kJ·kg^{-1}]	198.72	184.28

Janković et al. **[10]** carried out a study in a VCR system and found that the cooling capacity of R1234ze(E) is 27 % lower, and the COP value is similar to that of R134a. They also observed that at higher compressor speeds, R1234ze(E) provides the same cooling capacity with R134a at the rates of 34 % to 39 %. Kabeel et al. **[11]** figured out the performance of the VCR cycle for the cases of R134a and R1234ze(E). They found that the R1234ze(E)

*Corr. Author's Address: University of Yalova, Faculty of Engineering, Turkey, mehmetdirek@hotmail.com

has lower cooling capacity and compressor power by 2 % to 13 % and 9 % to 15 %, respectively. Righetti et al. [12] conducted performance analysis of a roll-bond evaporator for household refrigerators using R1234yf, R1234ze(E) and R600a and tested similar vaporization performance from the refrigerants. They concluded that these refrigerants could be considered as alternatives to R134a when they have similar mass flow rates. Sethi et al. [13], conducted a performance evaluation of two different refrigerants having low GWP, R1234yf and R1234ze(E), as substitutes for R134a. When the larger compressor displacement is used, R1234ze(E) performed similarly to R134a.

Mastrullo et al. [14] built a simulation model to assess the evolvement of the temperature inside a train compartment. They found that COP of the R1234ze(E) is 16 % higher than the case of R134a. Majurin et al. [15] were conducted research to figure the material compatibility exposures using R1234yf, R1234ze(E), and a mixture of R1234yf, R1234ze(E), and R32.

The performance of the VCR cycle can be increased by introducing an IHX into the liquid and gas suction line. The IHX increases the value of the sub-cooling at the condenser outlet, and thus raises the enthalpy difference in the evaporator and enhances the cooling capacity [16]. Cho and Park [17] determined the performance of an experimental automotive air-conditioning system for the cases of R134a and R1234yf refrigerant utilization. They found that when the IHX is used in the system, the cooling capacity of R1234yf was enhanced by 0.9 % compared to that of R134a at 2500 rpm. Furthermore, they determined that the amount of exergy destruction in the compressor is higher than that of the evaporator, after increasing the speed of the compressor. Direk et al. [18] investigated the effects of a double-pipe IHX added to the system on the performance parameters in an automobile air conditioning system using R1234yf. They stated that the contribution of the IHX to the COP is reduced by increasing the temperatures of the airflow entering the evaporator and the condenser. Babiloni et al. [7] found that R1234ze(E) provides the same cooling capacity values as R134a at 36 % higher compressor speed or geometric volume. They also found that the mass flow rate of R1234ze(E) was 5 % higher than R134a when it was operated at 43 % higher compressor speeds. As a result, they have determined that the difference in cooling capacity compared to R134a can be reduced by up to 20 % when R1234ze(E) is used with an IHX. Researchers in the literature use different types of heat exchangers for better system performance as they contribute to effective and more efficient functioning of the system [19]. Due to their high overall heat-transfer coefficient and compactness, plate type heat exchangers have recently gained more attention [20]. Such exchangers can be used instead of double-pipe heat exchangers as the IHX in the cooling systems. Devecioğlu and Oruç [21] investigated the effects of a plate-type heat exchanger in the liquid and gas suction line, on the system performance of an air conditioner using R453a, as an alternative to R22. They have found that the COP value obtained with R453a is lower than that of R22. However, there was a significant improvement in the COP value with the use of the IHX.

Jemaa et al. [22] theoretically investigated a VCR system using R1234ze(E) as an alternative to R134a under different evaporator and ambient temperatures. They determined that the irreversibility was lower in case of R1234ze(E). Yataganbaba et al. [23] developed a theoretical model to calculate the exergetic performance of the two evaporator VCR system using R1234yf and R1234ze(E) as alternatives to R134a. They determined that the second law efficiency of the system with R1234ze(E) and R134a is higher than that of R1234yf. Perez-Garcia et al. [24] conducted a second law analysis of the MAC system with IHX using R152a, R1234yf, and R1234ze(E). They determined that second law efficiency was the highest for R1234ze(E) when the superheating degree effect is increased.

To the best of our knowledge, this is the first experimental demonstration of drop in performance of R1234ze(E) in an R134a-based MAC system under various compressor speeds. In this research, the experimental setup was employed with on and off valves to activate liquid and gas section line IHX. The influence of energy and exergy performance of a plate-type IHX was extensively evaluated, and the exergy destruction in the components of the system was investigated. System performance parameters were realized, considering various compressor speeds, and the results were presented comparatively.

1 THERMODYNAMIC ANALYSIS

Fig. 1 shows the paths that the refrigerant follows within the system. The refrigerant follows the path of 1-2-3-4-5 when the IHX is inactive and follows the path of 1'-2'-3'-4'-5' when it is active.

Energy analysis was done by applying the first law of thermodynamics to each component of the MAC system. The exergy analysis was performed employing the second law of thermodynamics. Accordingly, the energy analysis for a steady-state system can be evaluated by:

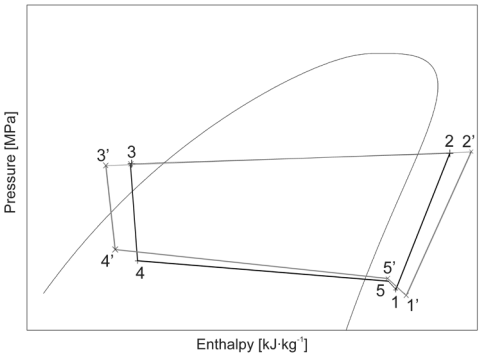

Fig. 1. *P-h diagram of the system with and without IHX*

$$\dot{Q}_{CV} - \dot{W}_{CV} = \sum \dot{m}_i h_i - \sum \dot{m}_o h_o. \quad (1)$$

The exergy analysis for a steady-state system was calculated by:

$$\dot{E}x_d = \sum \left(1 - \frac{T_0}{T}\right)\dot{Q} - \sum \dot{W} + \sum_i \dot{m}\psi - \sum_o \dot{m}\psi, \quad (2)$$

$$\psi = (h - h_0) - T_0(\mathrm{s} - s_0). \quad (3)$$

Assuming no heat loss from the compressor, the energy and exergy values can be obtained using:

$$\dot{W}_{comp} = \dot{m}_r \left(h_2 - h_1\right), \quad (4)$$

$$\dot{E}x_{d,comp} = \dot{m}_r \left(\psi_1 - \psi_2\right) + \dot{W}_{comp}. \quad (5)$$

The exergy destruction rate of the thermostatic expansion valve (TXV) can be calculated from:

$$\dot{E}x_{d,TXV} = \dot{m}_r \left(\psi_3 - \psi_4\right) = \dot{m}_r T_0 (s_4 - s_3). \quad (6)$$

The energy and exergy analysis of the evaporator and condenser can be expressed as:

$$\dot{Q}_{evap} = \dot{m}_r \left(h_4 - h_1\right), \quad (7)$$

$$\dot{E}x_{d,evap} = \dot{m}_r \left(\psi_1 - \psi_4\right) + \dot{Q}\left(1 - \frac{T_0}{T_{evap}}\right), \quad (8)$$

$$\dot{Q}_{cond} = \dot{m}_r \left(h_3 - h_2\right), \quad (9)$$

$$\dot{E}x_{d,cond} = \dot{m}_r \left(\psi_2 - \psi_3\right) - \dot{Q}\left(1 - \frac{T_0}{T_{cond}}\right). \quad (10)$$

The energy and exergy destruction rate for the IHX can be determined from:

$$h_{i,IHX,evap} + h_{i,IHX,cond} = h_{o,IHX,evap} + h_{o,IHX,cond}, \quad (11)$$

$$\dot{E}x_{d,IHX} = \dot{m}_r \left(\psi_{i,IHX,evap} - \psi_{o,IHX,evap}\right) + \dot{m}_r \left(\psi_{i,IHX,cond} + \psi_{o,IHX,cond}\right). \quad (12)$$

The COP of the MAC system can be obtained from:

$$COP = \dot{Q}_{evap} / \dot{W}_{comp}. \quad (13)$$

The total exergy destruction rate for the MAC system can be obtained from:

$$\dot{E}x_{d,t} = \dot{E}x_{d,comp} + \dot{E}x_{d,cond} + \dot{E}x_{d,TXV} + \dot{E}x_{d,evap} + \dot{E}x_{d,IHX}. \quad (14)$$

2 EXPERIMENTAL SETUP

The experimental system consists of the components of a VCR system used in MAC systems. This system, which is schematically shown in Fig. 2, consists of a swash-plate type compressor, a parallel-flow condenser, a laminar type evaporator, a thermostatic expansion valve and a liquid tank. In addition, a plate-type heat exchanger was introduced to the liquid and gas suction lines of the system to provide heat to the fluid stream exiting the evaporator in the vapour phase.

In the experimental MAC system used, the refrigerant is converted into superheated vapour at high pressure and temperature in the compressor and sent to the condenser. It is condensed through the air flow and exits the condenser in a phase of compressed liquid at high pressure.

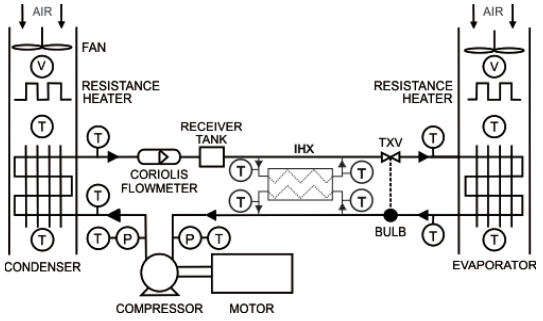

Fig. 2. Schematic diagram of the experimental setup

Afterwards, the refrigerant, which enters the IHX, transfers heat to the fluid stream that is in a vapour phase, which exits the evaporator and enters the IHX. The refrigerant in the liquid phase then passes through the liquid tank and through the Coriolis-type mass flow meter. Afterwards, the refrigerant flows to the TXV, and it arrives the evaporator as a liquid-vapour phase at low pressure after its pressure and temperature are decreased in TXV in such a way that the superheat at the outlet of the evaporator remains constant. The heat-loaded refrigerant, which exits the

evaporator, is directed to the IHX and finally to the compressor inlet and completes its cycle.

Electric heaters were installed to provide the desired airflow temperatures in the evaporator and condenser ducts, and the fans were installed to provide the airflow to the inlet of the air ducts at the desired speed. Copper tubes were used for the steam and liquid lines as connection elements. The connecting elements were isolated with elastomeric isolation material. The components of the experimental system are presented in Table 2.

Table 2. *Specifications of components MAC system*

Components	Specifications
Compressor	Swash-plate type 138 cc Number of Cylinders: 5
Condenser	(580 × 350 × 20) mm^3
Evaporator	(220 × 260 × 60) mm^3
Expansion valve	TXV (Internally equalized with bulb 5.27 kW)
Internal heat exchanger	(192 x 73 x 63) mm^3 Type: Brazed plate Number of plates: 24 Heat transfer area: 0.6 m^2

The system was equipped with various measuring instruments. The temperatures of the refrigerant were measured at the inlet and outlet points of each component using K-type thermocouples. The measured values were transferred to the computer via the data acquisition system.

The pressure measurements for evaporation and condensation were carried out by using a digital manifold at four points in the system. The mass flow rate of the refrigerant was measured with a Coriolis-type flow meter. The precisions of the measuring devices are presented in Table 3. A frequency inverter was used to set the compressor speed with a 2.2 kW electric motor.

Table 3. *Specifications of the instrumentation*

Measurement	Device	Range	Precision
Temperature	K-type Thermocouple	-100 °C to 1370 °C	±0.8 °C
Pressure	Electronic Manifold	-1 bar to 60 bar	±0.5 %
Air Flow Rate	Anemometer	0 ms^{-1} to 30 ms^{-1}	±2 %
Refrigerant Mass Flow Rate	Coriolis Mass Flow Meter	0 kg s^{-1} to 5 kg s^{-1}	±0.1 %
Power	Clamp Meter	0 kW to 600 kW	±2 %
Compressor Speed	Frequency inverter	10 Hz to 50 Hz	±0.2 %

The thermophysical properties of the refrigerant are taken from the REFPROP 9.1 program [9]. The charge amount of R134a in the system was determined when the system achieved the best COP. To provide mass equivalence in the system, the charge amount was calculated by using liquid densities. In the experimental study, 600 g of R134a and 625 g of R1234ze(E) refrigerant were charged into the system, in accordance with the liquid density of refrigerant presented in Table 1. In the experiments, the temperatures of the airflow entering the evaporator and condenser were kept constant at 27 °C and 35 °C, respectively. Experiments were carried out by changing the speed of the compressor between 750 rpm and 2750 rpm by 500 rpm increment intervals. During the experiments, the measurements were done after the system was stabilized. During the experiments, the electric heaters were run to regulate the air stream temperatures at the inlet of the evaporator and condenser. The main data used for measuring the performance of the cycle are temperature, pressure and refrigerant mass flow rate. With presented precision values in Table 3, the calculated uncertainty rates for the cooling capacity, COP and compressor power were ±2.99 % ±4.4 %, and ±3.24 %, respectively.

3 RESULTS AND DISCUSSION

In this section, the performance parameters of the system are discussed considering the effect of IHX for R1234ze(E). The superheat and sub-cooling degrees of the system are the best ways to show the IHX effect on the cooling cycle. Table 4 shows the experimental superheat and sub-cooling degrees for various compressor speeds and configurations of the system.

Table 4. *Superheat and sub-cooling values of each configuration*

	Compressor speed [rpm]	R134a	R1234ze(E)	R1234ze(E) + IHX
Superheat [°C]	750	5.2	6.14	10.26
	1250	7.5	10.66	15.65
	1750	10.2	13.92	20.01
	2250	12.7	20.75	24.82
	2750	15.6	22.86	29.38
Sub-cooling [°C]	750	5.77	8.51	12.01
	1250	7.08	12.46	16.70
	1750	8.81	14.45	20.44
	2250	10.93	16.09	24.59
	2750	9.54	20.73	28.16

It is understood from Table 4 that by adapting the IHX to the system, both the superheat and sub-cooling degree were increased. The increased sub-cooling degree improves the cooling capacity by increasing

the latent heat of vaporization of the refrigerant. However, the exergy destruction in the compressor increased by increasing the superheat value.

Fig. 3 represents the change in compressor power as a function of compressor speed. The vapour density of R1234ze(E) is lower than R134a, as seen in Table 1. Thus, the experimental results indicate that the mass flow rate of R134a is 17 % higher than that of R1234ze(E). This results in the higher compression power demands for R134a compared to R1234ze(E). When the IHX is adapted to the system, it increased the superheat value for R1234ze(E), as seen in Table 4.

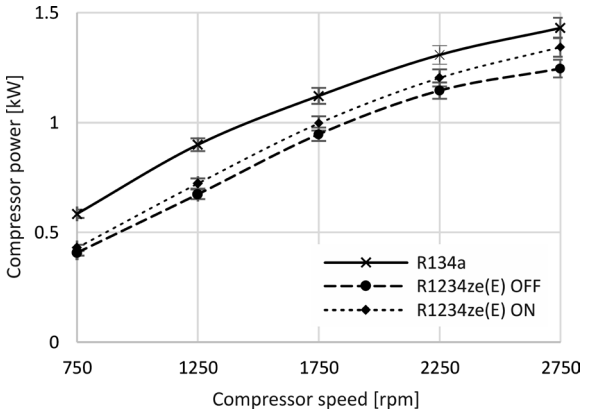

Fig. 3. *Compressor power versus compressor speed*

Considering the changes caused by the addition of IHX, the suction pressure of the compressor was reduced, and the value of superheat was increased; thus, the compression ratio was increased accordingly. As a result, the compressor power was enhanced by adapting IHX to the system.

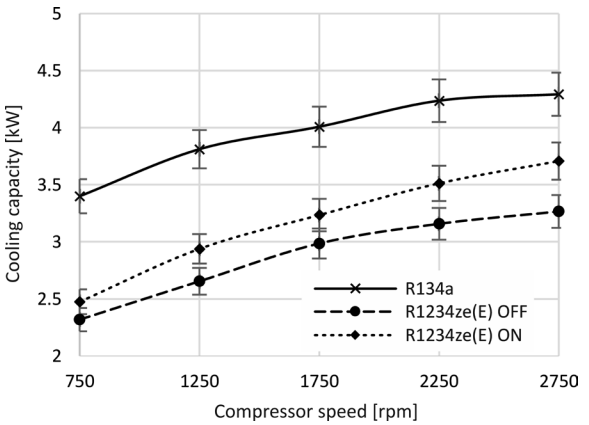

Fig. 4. *Cooling capacity versus compressor speed*

Fig. 4 demonstrates the cooling capacity for all configurations as a function of compressor speed. R1234ze(E) has 7 % lower latent heat of vaporization compared to R134a, which leads to lower cooling capacity at the same evaporation pressure. However, the IHX enhances latent heat by boosting the sub-cooling values. R1234ze(E) has an average 27 % lower cooling capacity as seen in Fig. 4. In addition, the cooling capacity was increased by 7 % after the IHX was introduced. The IHX enhances the value of the sub-cooling at the condenser outlet as depicted in Fig. 1. Table 4 also indicates that the amount of sub-cooling increases due to the compressor speed. Consequently, the amount of sub-cooling directly affects the enthalpy difference in the evaporator and thus, the cooling capacity improves.

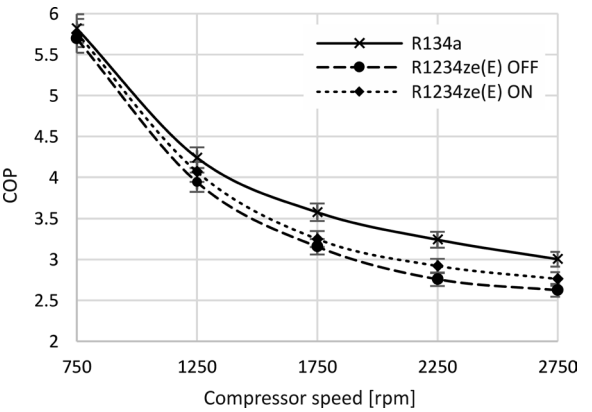

Fig. 5. *COP versus compressor speed*

The changes in COP depending on the compressor speed are presented in Fig. 5. It can be seen that the COP obtained at all compressor speeds for R1234ze(E) on the refrigerant is lower than that of R134a. However, COP of R1234ze(E) is very close to R134a at lower compressor speeds. Furthermore, the difference become lower when IHX was introduced into the system. An increase in the COP of R1234ze(E) was observed after the IHX was adapted. COP was increased by 4 % on average after the activation of IHX.

The exergy destruction of the system for different configurations is given in Fig. 6. It can be seen that the values of exergy destruction for R1234ze(E) are lower than that of R134a, regardless of the presence of IHX. The exergy destruction for all configurations was increased by increasing the compressor speed. In addition, the exergy destruction was increased by introducing IHX to the system with R1234ze(E). This is considered to be due to the increase in exergy destruction in the compressor and the exergy destruction inside the IHX at increasing compressor speeds.

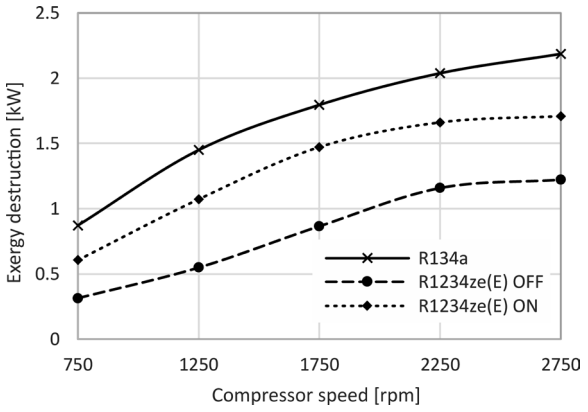

Fig. 6. *Exergy destruction versus compressor speed*

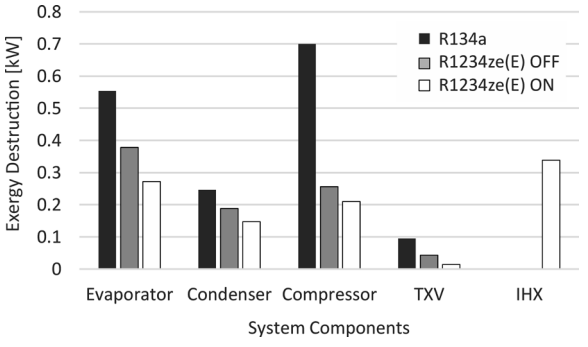

Fig. 7. *Equipment-based distribution of exergy destruction at 1750 rpm*

The equipment-based distribution of exergy destruction values at 1750 rpm are shown in Fig. 7. It should be noted that the exergy destruction values are decreased in the condenser, evaporator, and TXV, but increased in the compressor by employing the IHX. Moreover, introducing an IHX to the system leads to a certain amount of exergy destruction.

4 CONCLUSIONS

In this study, the usage of R1234ze(E) in an R134a-based MAC system was experimentally investigated. Additionally, the effect of the IHX, on the performance of the MAC system was determined by using R1234ze(E). The results of the study and the evaluations are presented below.

The compressor power for R1234ze(E) was lower than that of R134a by 19 %, but the difference became lower (14 %) when IHX was introduced into the system. The cooling capacity was lower for R1234ze(E) than R134a by 27 %. The cooling capacity was improved by 7 % when IHX was adapted.

The COP of R1234ze(E) was lower than that of R134a by 8 % to 10 %. The COP value was enhanced by 4 % when IHX was adapted to the system. The exergy destructions of R1234ze(E) were lower than R134a by 50 %, and this became lower by 25 % on average when IHX was adapted to the system.

In light of these results, it is considered that R1234ze(E) might be an alternative refrigerant suitable for MAC applications if necessary amendments are carried out.

5 ACKNOWLEDGEMENTS

The authors would like to thank the Scientific and Technological Research Council of Turkey (TÜBITAK) for supporting this study through Research Project No 216M437.

6 NOMENCLATURE

$\dot{Q}$	heat transfer, [kW]
$\dot{W}$	work, [kW]
$\dot{m}$	mass flow rate, [kg·s^{-1}]
h	enthalpy, [kJ·kg^{-1}]
$\dot{E}x$	exergy destruction, [kW]
T	temperature, [K]
s	entropy, [kJ·kg^{-1}·K^{-1}]
ψ	flow specific exergy, [kJ·kg^{-1}]

Subscripts:

comp	compressor,
cond	condenser,
CV	control volume,
e	electrical,
evap	evaporator,
ex	exergy,
d	destruction,
i	inlet,
o	outlet,
r	refrigerant,
t	total,
0	dead state.

7 REFERENCES

[1] Hartmann, D.L., Klein Tank, A.M.G.,Rusticucci, M.,Alexander, L.V., Brönnimann, S., Charabi, Y., Dentener, F.J., Dlugokencky, E.J., Easterling, D.R., Kaplan, A., Soden, B.J., Thorne, P.W., Wild, M., Zhai, P.M. (2013). Observations: Atmosphere and Surface. Stocker, T.F., Qin, D., Plattner, G-K., Tignor, M., Allen, S.K., Boschung, J., Nauels, A., Xia, Y., Bex, V., Midgley, P.M. (eds.), *Climate Change 2013: The Physical Science Basis*. Cambridge University Press, Cambridge, p. 159-254, **DOI:10.1017/CBO9781107415324.008**.

[2] *Directive 2006/40/EC of the European Parliament and of the Council of 17 May 2006 Relating to Emissions from Air*

Conditioning Systems in Motor Vehicles and Amending Council Directive 70/156/EC (2006). Official Journal of the European Union, Brussels.

[3] *Regulation (EU) No 517/2014 of the European Parliament and the Council of 16 April 2014 on Fluorinated Greenhouse Gases and Repealing Regulation (EC) No 842/2006 (2014).* Official Journal of the European Union, Brussels.

[4] Aprea, C., Greco, A., Maiorino, A., Masselli, C., Metallo, A. (2016). HFO1234ze as drop-in replacement for R134a in domestic refrigerators: An environmental impact analysis. *Energy Procedia*, vol. 101, p. 964-971, **DOI:10.1016/j.egypro.2016.11.122**.

[5] ASHRAE Standard 34 (2013). *Designation and Safety Classification of Refrigerants. American Society of Heating, Refrigerating and Air-Conditioning Engineers*, Atlanta.

[6] Imamura, T., Yoshida, Y., Ota, Y., Naito, K., Sugawa, O. (2017). Full-scale experiment to evaluate the combustion hazard of refrigerants with low global-warming potential in a conceivable accident scenario. *International Journal of Refrigeration*, vol. 82, p. 461-469, **DOI:10.1016/j.ijrefrig.2017.06.004**.

[7] Mota-Babiloni, A., Navarro-Esbrí, J., Mendoza-Miranda, J. M., & Peris, B. (2017). Experimental evaluation of system modifications to increase R1234ze(E) cooling capacity. *Applied Thermal Engineering*, vol. 111, p. 786-792, **DOI:10.1016/j.applthermaleng.2016.09.175**.

[8] Leighton, D., Hwang, Y., Radermacher, R. (2012). Modeling of household refrigerator performance with low global warming potential alternative refrigerants. *ASHRAE Transactions*, vol. 118, p. 658.

[9] Lemmon, E.W., Huber, M.L., McLinden, M.O. (2014). *REFPROP*, NIST Standard Reference.

[10] Janković, Z., Atienza, J.S., Suárez, J.A.M. (2015). Thermodynamic and heat transfer analyses for R1234yf and R1234ze(E) as drop-in replacements for R134a in a small power refrigerating system. *Applied Thermal Engineering*, vol. 80, p. 42-54, **DOI:10.1016/j.applthermaleng.2015.01.041**.

[11] Kabeel, A.E., Khalil, A., Bassuoni, M.M., Raslan, M.S. (2016). Comparative experimental study of low GWP alternative for R134a in a walk-in cold room. *International Journal of Refrigeration*, vol. 69, p. 303-312, **DOI:10.1016/j.ijrefrig.2016.06.017**.

[12] Righetti, G., Zilio, C., Giovanni, A.L. (2015). Comparative performance analysis of the low GWP refrigerants HFO1234yf, HFO1234ze(E) and HC600a inside a roll-bond evaporator. *International Journal of Refrigeration*, vol. 54, p. 1-9, **DOI:10.1016/j.ijrefrig.2015.02.010**.

[13] Sethi, A., Vera-Becerra, E., Yana-Motta, S. (2016). Low GWP R134a replacements for small refrigeration (plug-in) applications. *International Journal of Refrigeration*, vol. 66, p. 64-72, **DOI:10.1016/j.ijrefrig.2016.02.005**.

[14] Mastrullo, R., Mauro, A.W., Vellucci, C. (2016). Refrigerant alternatives for high speed train A/C systems: energy savings and environmental emissions evaluation under variable ambient conditions. *Energy Procedia*, vol. 101, p. 280-287, **DOI:10.1016/j.egypro.2016.11.036**.

[15] Majurin, J., Staats, S.J., Sorenson, E., Gilles, W. (2015). Material compatibility of HVAC&R system materials with low global warming potential refrigerants. *Science and Technology for the Built Environment*, vol. 21, p. 491-501, **DOI:10.1080/23744731.2015.1009353**.

[16] Klein, S.A., Reindl, D.T., Brownell, K. (2000). Refrigeration system performance using liquid-suction heat exchangers. *International Journal of Refrigeration*, vol. 23, no. 8, p. 588-596, **DOI:10.1016/S0140-7007(00)00008-6**.

[17] Cho, H., Park, C. (2016). Experimental investigation of performance and exergy analysis of automotive air conditioning systems using refrigerant R1234yf at various compressor speeds. *Applied Thermal Engineering*, vol. 101, p. 30-37, **DOI:10.1016/j.applthermaleng.2016.01.153**.

[18] Direk, M., Kelesoglu, A., Akin, A. (2017). Drop-in performance analysis and effect of IHX for an automotive air conditioning system with R1234yf as a replacement of R134a. *Strojniški vestnik-Journal of Mechanical Engineering*, vol. 63, no. 5, p. 314-319, **DOI:10.5545/sv-jme.2016.4247**.

[19] Bošnjaković, M., Čikić, A., Muhič, S., Stojkov, M. (2017). Development of a new type of finned heat exchanger. *Tehnički vjesnik - Technical Gazette*, vol. 24, no. 6, p. 1785-1796, **DOI:10.17559/TV-20171011071711**.

[20] Pribošek, J., Bobič, M., Golobič, I., Diaci, J. (2016). Correcting the Periodic Optical Distortion for Particle-Tracking Velocimetry in Corrugated-Plate Heat Exchangers. *Strojniški vestnik - Journal of Mechanical Engineering*, vol. 62 no. 1, p. 3-10, **DOI:10.5545/sv-jme.2015.3125**.

[21] Devecioğlu, A.G., Oruç, V. (2017). The influence of plate-type heat exchanger on energy efficiency and environmental effects of the air-conditionersa using R453A as a substitute for R22. *Applied Thermal Engineering*, vol. 112, p. 1364-1372, **DOI:10.1016/j.applthermaleng.2016.10.180**.

[22] Jemaa, R.B., Mansouri, R., Boukholda, I., Bellagi, A. (2017). Energy and exergy investigation of R1234ze as R134a replacement in vapor compression chillers. *International Journal of Hydrogen Energy*, vol. 42, no. 17, p. 12877-12887, **DOI:10.1016/j.ijhydene.2016.12.010**.

[23] Yataganbaba, A., Kilicarslan, A., Kurtbas, I. (2015). Exergy analysis of R1234yf and R1234ze as R134a replacements in a two evaporator vapor compression refrigeration system. *International Journal of Refrigeration*, vol. 60, p. 26-37, **DOI:10.1016/j.ijrefrig.2015.08.010**.

[24] Pérez-García, V., Belman-Flores, J.M., Rodríguez-Mu-oz, J.L., Rangel-Hernández, V.H., Gallegos-Mu-oz, A. (2017). Second law analysis of a mobile air conditioning system with internal heat exchanger using low GWP refrigerants. *Entropy*, vol. 19, no. 4, p. 175, **DOI:10.3390/e19040175**.

Strojniški vestnik - Journal of Mechanical Engineering 64(2018)2, 121-129
DOI:10.5545/sv-jme.2017.4942
Original Scientific Paper
Received for review: 2017-09-20
Received revised form: 2018-01-11
Accepted for publication: 2018-01-29

Surface Modification and Wear Properties of Direct Metal Laser Sintered Hybrid Tools Used in Moulds

István Hatos[1,*] – Imre Fekete[1] – Tamás Ibriksz[1] – József G. Kovács[2] – Mária B. Maros[3] – Hajnalka Hargitai[1]

[1] Széchenyi István University, Department of Materials Science and Technology, Hungary
[2] Budapest University of Technology and Economics, Department of Polymer Engineering, Hungary
[3] University of Miskolc, Department of Mechanical Technology, Hungary

Injection moulding is one of the most productive plastic forming processes. Product development and the reduction of production time require new solutions in tooling design and manufacturing. Direct metal laser sintering (DMLS) allows moulds to be built with special cooling systems, which offer curved cooling lines that can follow the geometry of the part (conformal cooling). One disadvantage of DMLS, its high cost, can be dramatically reduced with the building of hybrid structures. With conventional tool steels as the base plate and only the special geometry of the part sintered on the top, the final geometry can be manufactured after sintering by conventional process technologies. We produced hybrid structures by direct metal laser sintering maraging steel (MS1) powder onto the surface of commercial mould steels and studied the effect of different heat treatments on porosity, tribological behaviour and the microstructure. The transition zone was also characterized.
Keywords: direct metal laser sintering, hybrid structure, maraging steel, 1.2343 steel, heat treating, wear

Highlights

- *Age hardening and quenching was compared on the hardness of the different steel grades. Age-hardening results in almost the same hardness as quenching in maraging steels, while the same heat treatment resulted in softening in the case of 1.2343 steel.*
- *Quenching produced the same hardness as age hardening in MS1 steel.*
- *The sintered maraging steel showed lower wear resistance than its conventionally produced counterpart in all cases, which can be explained with the higher porosity as a result of sintering.*
- *In the case of hybrid structures, it is necessary to select heat treatments and heat-treating parameters that produce the required properties in both components.*
- *If tool steel is used in hybrid constructions, which require quenching to assure the prescribed properties, this heat treatment can produce the same hardness in the MS1 part as age hardening can when high-temperature tempering is applied after quenching.*

0 INTRODUCTION

Injection moulding is one of the most critical polymer processing technologies. The most significant phase of the injection moulding cycle is cooling time, which can be more than half the whole cycle **[1]**. One of the best ways to achieve a reduction in cooling time is to use mould inserts with conformal cooling **[2]**; shrinkage and warpage can thus also be decreased **[3]**.

With layer manufacturing technologies, parts of complex internal structures can be built, which can be a major advantage for injection moulds **[4]**. The cooling channels may have a complex form, which cannot be manufactured with conventional methods, such as drilling or milling **[5]**. Tooling companies are increasingly employing additive manufacturing (AM) technologies to fabricate moulds with integrated conformal cooling channels. Selective laser sintering (SLS) is an AM technique, which is capable of manufacturing 3D parts from different powder materials **[6]**. The powder is scanned and selectively sintered according to the two-dimensional cross-section of the sliced model of the CAD geometry. In the beginning, these systems only worked with polymer powders. Then, as the technology developed, companies introduced laser sintering processes for building parts from metal powders. Direct metal laser sintering (DMLS) **[7]** and selective laser melting (SLM) **[8]** are the most widespread techniques at present, and both technologies use metal powders without coating **[9]**.

Producing mould inserts from metal powders by AM is an expensive technology in comparison to conventional machining. A major challenge is to integrate free shape AM and cheap conventional manufacturing processes **[10]**. Metal AM is a promising technology to fabricate complex geometry and hybrid structures from different metals, e.g. cobalt-based alloy deposited on conventional tool steel **[11]** or sintering of maraging steel on a copper substrate **[12]**.

A limited number of tool steels are available for additive manufacturing; maraging steel (1.2709) powder is the regularly used raw material for

*Corr. Author's Address: Széchenyi István University, Egyetem square 1, Győr, Hungary, hatos@sze.hu

printing moulds. Maraging steels are strengthened by precipitation hardening in furnaces without a protective atmosphere and at relatively low temperatures (approx. 500 °C). Surface heat treatment, such as nitriding, can reduce wear and corrosion, and the lifetime of plastic injection moulds can be extended. Nitriding is a surface-hardening process, introducing nitrogen into the surface of the steel. In conventional gas nitriding processes, the temperature range of nitriding is 500 °C to 550 °C, which is higher than the aging temperature of maraging steels, and thus would result in over-aging. Different thermomechanical heat treatments such as nitriding [13], nitrocarburizing, boriding and carburizing can improve the wear resistance of maraging steel [14]; the best results can be achieved by plasma nitriding [15].

In the case of hybrid tooling, the base part is manufactured with conventional technologies, while the upper part (designed for conformal cooling) is built layer by layer with DMLS technology. In an optimal case, the base and the over-sintered material have the same chemical composition. Maraging steels have a relatively high price and only a limited range of raw materials is available; therefore, they are regularly replaced by conventional tool steels (1.2311, 1.2343, etc.) and heat treated similarly to the base part [16].

Samples made from DMLS MS1, Böhler W722 and 1.2343 steels with different surface hardness after ageing, hardening, nitrocarburizing and nitrocarburizing combined with post-oxidation (oxy-nitriding) were investigated. The microstructure, hardness and wear properties of the samples were characterized; the hybrid structures were studied and analysed mainly from a tribological point of view but also with a focus on the transition layer.

1 EXPERIMENTAL

1.1 Materials

The samples were prepared from "MaragingSteel MS1" steel powder by direct metal laser sintering (DMLS). Injection moulds having conformal cooling channels are regularly made from MS1. EOSINT M270 (200 W) was used with the EOS MS1_Surface 1.0 parameter setting and a layer thickness of 20 μm. Commercially available materials were selected as reference: Bohler-Uddeholm W722 VMR (~1.2709) maraging steel made by vacuum induction melting, and 1.2343 steel, a material generally used for injection moulds (Table 1).

1.2 Sample Manufacturing

Disk-like specimens with a diameter of 30 mm and a thickness of 5.5 mm were produced. Samples made of MS1 powder were sintered, while the reference materials were machined from a rod (Ø30 mm). To guarantee the same test conditions, the specimens were ground then polished with the same parameters with 1 μm diamond paste (surface roughness, Ra = 0.015 μm to 0.02 μm) before the heat treatments. The samples were repolished after age-hardening, but they were not repolished after nitro-carburizing and oxy-nitriding. Hybrid test specimens were also made by sintering MS1 material onto the surface of rectangular W722 and 1.2343 blocks.

1.3 Heat Treatment

Sintered parts (MS1) have a surface hardness of 33 HRC to 37 HRC [19], but injection moulds require a much harder material. Surface hardness can be increased by heat treatments, especially by surface hardening methods, like carbonitriding. MS1 and W722 grades can be hardened by precipitation treatments. Heat treatment parameters, generally applied during precipitation or age hardening are as follows: the heating temperature range is 455 °C to 510 °C, while the holding time is 3 to 12 hours. Then the metal is slowly cooled to room temperature in air [20]. The results of several heat treatments showed that the above-mentioned temperature-time parameters only produced a small, 1 HRC to 2 HRC increase in hardness [21]. In the case of MS1 and W722 steels, nitriding and age hardening are carried out in one step.

Bulk and surface heat treatments were used to achieve higher strength and hardness of the steels and enhance the wear resistance of their surface. The technological parameters of age hardening and

Table 1. *Chemical composition of the tested steel materials [17] to [19]*

Steel	C	Cr	Ni	Mn	Si	Al	Co	Mo	Ti	V
MS1	<0.03	<0.5	17 to19	<0.1	<0.1	0.05 to 0.15	8.5 to 9.5	4.5 to 5.2	0.6 to 0.8	
W722	<0.005		18				9.25	4.85	1.00	
1.2343	0.38	5.00		0.4	1.10			1.30		0.4

Table 2. *Heat treatment conditions*

Heat treatment method	Abbrev.	Material	Temperature [°C]	Duration [h]	Atmosphere
Age hardening	AH	MS1, W722 (1.2343)	500	4	air
Quenching+ 2 × tempering	Q	MS1, 1.2343	1050	1	vacuum
			530 and 480	530 and 480	
Nitro-carburizing	NC	MS1, W722, 1.2343(Q)	550	8 (∑12)	mixture of gases
Oxy-nitriding	NO	MS1, W722, 1.2343(Q)	550	7 (∑13)	mixture of gases 6 l/h to 7 l/h water
			450	1	

quenching were selected based on the literature [17] to [19] (Table 2.).

We used thermochemical treatments, such as nitro-carburizing and oxy-nitriding to study the effect of microstructure on the wear behaviour of both the simple and hybrid parts. Surface treatment parameters usually applied for 1.2343 steels were selected for the experiments (atmosphere: 50 % nitrogen (4 m³/h), 45 % ammonia (3.7 m³/h) and 5 % carbon dioxide (80 l/h)). The usual consequences of nitriding or nitro-carburizing are increased surface hardness and wear resistance, lower wear coefficient, increased fatigue resistance, ductility, and increased corrosion resistance, which usually result in increased tool life. The additional oxidation of the nitrided layer results in an additional improvement of all the surface characteristics mentioned above. Commercial oxy-nitriding involves nitriding for several hours followed by oxidation in a superheated steam atmosphere.

1.4 Test Methods

1.4.1 Microstructure and Pore Characterization

Both microstructure and pores were characterized on the polished cross-sections. Samples for metallographic examination were etched with Nital and examined with an optical microscope (Zeiss Axio Imager A1).

The transition zones of the hybrid parts were characterized with a scanning electron microscope equipped with EDS (Hitachi 3400).

1.4.2 Hardness Test

The macro and microVickers hardness of the sintered samples and the hardness profiles of the nitrided materials were tested.

We used the Vickers method to measure surface and core hardness based on the MSZ EN ISO 6507-1 standard [22] with KB750 and KB30 hardness testing machines. Surface hardness was tested both before and after heat treatments (HV10). After nitro-carburizing and oxi-nitriding, core hardness and nitriding hardness depth (Nhd) were determined according to the DIN 50190 standard (HV0.3).

1.4.3 Wear Test and Characterization

The wear resistance of specimens after different heat treatments was compared. We analysed the results by calculating the cross-sectional area and the depth of the wear track obtained with a sliding distance of 360 m (60 min), which minimized the influence of surface irregularities.

Ball-on-disk type tribology tests were performed with a UNMT-1 Universal nano & micro surface tester. Zirconium oxide ceramic balls (HV1280; diameter of 5 mm) were used as the sliding part and for each test, a new ball was applied. The sliding speed was 100 mm/s (rev. of 318.47 1/min), and the normal load was 20 N. The tests were repeated three times in each case with the same test conditions (Fig. 1).

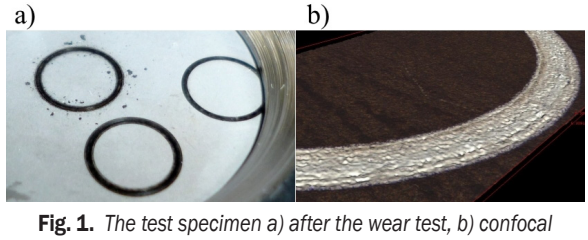

Fig. 1. *The test specimen a) after the wear test, b) confocal microscopic image*

For the analysis the effects of the different heat treatments on wear resistance, we determined the worn area by with series of 2D profile measurements of the wear tracks. The detailed description of the test method and the results of the 3D surface scan (the determination of worn area) can be found in [23]. Authors used a Hobson – Talysurf CLI2000 scanning surface topography instrument for the experiments (contact method, 100 Hz, radius of curvature: 5 μm). First, the centre of the wear track torus was determined, then the profile along two mutually perpendicular diameters was measured (see Fig. 2). The coordinates in a text file were stored, then the

worn areas were calculated with the algorithm we developed.

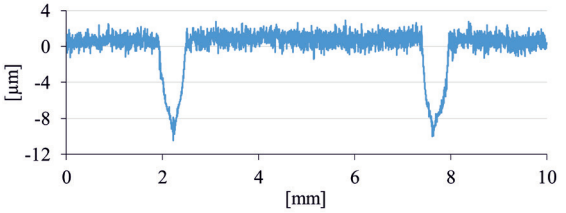

Fig. 2. *The 2D profile of the worn*

2 RESULTS

2.1 Microstructure and Porosity

The samples made with different manufacturing processes show different macroscopic characteristics. The metallographic examination showed that the DMLS material had a layered structure (Fig. 3) and the thickness of the structural layers was around 20 µm to 30 µm, consistent with sintering layer thickness. All layers had a regular wave-like form. In the microstructure of the samples made with the conventional manufacturing process, the direction of rolling is clearly recognizable.

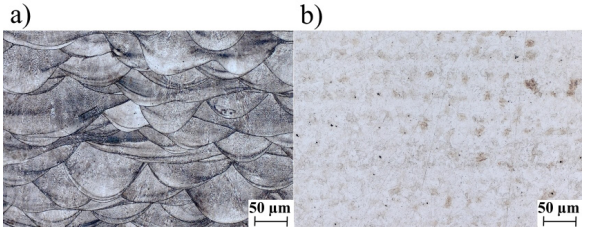

Fig. 3. *The side view of a) the DMLS material (MS1) showing the wavy layers, and b) the conventional W722 steel before heat treatment*

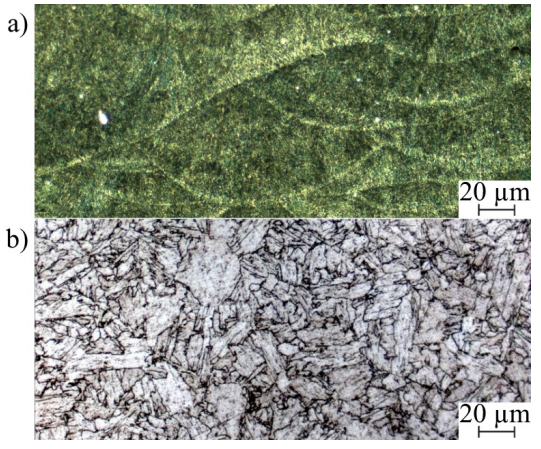

Fig. 4. *Microscopic images of a) age-hardened MS1, and b) W722 (Nital 2 %)*

The microscopic images of the age-hardened MS1 steel clearly show the typical wave-like structure of layers superimposed on each other, which presumably contain precipitations of the nanometre scale. The massive bundles of martensite can be clearly identified in the microstructure of W722. Finely dispersed intermetallic particles composed of the alloying elements can be clearly seen in the grains (Fig. 4).

2.2 Surface Hardness after Age Hardening and Hardening

To analyse the effect of heat treatment in the case of hybrid metals, we used age hardening for W722-MS1 and both age hardening and quenching for the 1.2343-MS1 combination. The results can be seen in Figure 5. Hardness increased significantly as a result of age hardening. Nearly the same hardness was achieved in the case of MS1 (sintered) and W722 (conventional) maraging steels. While the hardness of these two materials was ~590 HV when age-hardened, the heat treatment performed with the same technological parameters softened the 1.2343 steel. More suitable heat treatment (quenching and tempering twice), usually suggested for 1.2343 steel, resulted in the same hardness as that of the sintered MS1.

Nearly the same hardness can be achieved by three-step hardening and age hardening in the case of MS1 (Fig. 5).

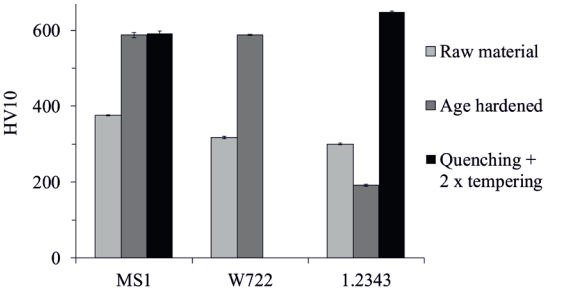

Fig. 5. *Surface hardness of MS1, W722 and 1.2343 materials before and after heat treatment*

This can be explained with the low differences between the temperature of tempering and age hardening, while the duration of the treatment is the same.

2.3 The Effect of Nitriding on the Microstructure of Hybrid Systems

Nitrided and carbonitrided layers typically consist of two areas. The inner (diffusion) region is characterized by the formation of nitride needles. Normal layer

thickness ranges from 0.2 mm to 1.5 mm. The outer region that is approximately 5 µm to 30 µm thick is called the compound layer. This non-metal layer consists mainly of γ'-nitrides (Fe4N), ε-nitrides (FexN) and possibly of carbonitrides (FexCyNz). Moreover, in alloyed steels nitrides and carbonitrides of the alloy elements are formed. The outer part of the surface layer can be formed as a porous edge, which later improves anti-corrosive properties through oxidation.

In the case of nitro-carburizing both nitrogen and carbon diffusion occur and similarly to nitriding, a compound layer of a few µm containing carbonitrides and an underlying diffusion zone of high nitrogen content is developed.

2.3.1 MS1 – W722 Hybrid Part

MS1 steel powder was sintered directly onto the surface of W722 steel; the hybrid part was then nitrocarburized. In the microscopic images, the parts produced with different technologies are well separated. The boundary between the two materials is not sharp; a ~50 µm-wide transition zone can be seen as a mixture of two materials, tracking the contour of the laser-scanning structure as images in Fig. 6 show.

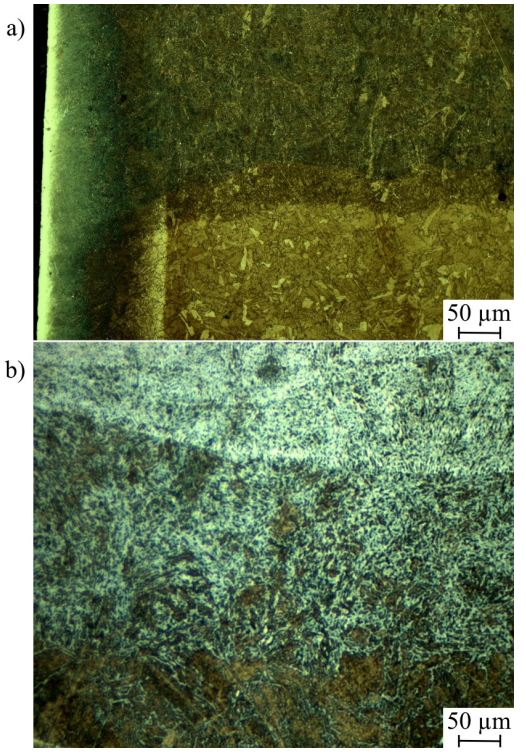

Fig. 6. *The microstructure of maraging steels after nitro-carburizing; a) the hybrid structure of W722 and MS1 steel, and b) the boundary area of the hybrid structure (Nital 2%)*

The thickness of the compound layer is nearly the same in the case of both materials; 13 µm for the MS1 and 12 µm for the W722 part.

Fig. 7 shows microhardness as a function of distance from the surface, i.e. the microhardness profiles obtained for the nitrocarburized (N) and oxy-nitrided (NO) MS1 and W722 steels. The initial part of the curves drops sharply, which indicates the low diffusion depth of C and N.

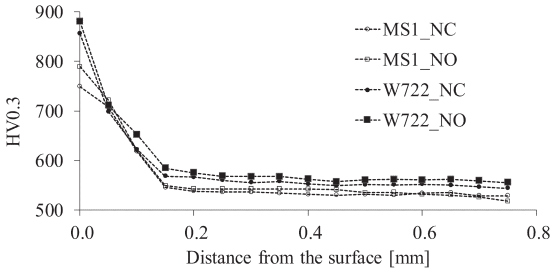

Fig. 7. *The HV0.3 microhardness profile of nitrocarburized (NC) and oxy-nitrided (NO) MS1 and W722 steels*

Surface hardening resulted in lower hardness in the core in each case, compared to that of age-hardened samples (Fig. 8). It can be explained with the higher duration time of the applied thermochemical treatments. On the one hand, during age hardening fine particles, typically coherent or semi-coherent inter-metallics are produced, which efficiently impede the movement of dislocations, and defects of the crystal lattice are created, which harden the material. On the other hand, during nitro-carburizing, the longer duration time leads to the further ripening and growing of non-equilibrium particles, resulting in the formation of incoherent precipitations of larger size and of more equilibrium composition. Altogether, this process, called over-aging, decreases the strength and hardness of the material.

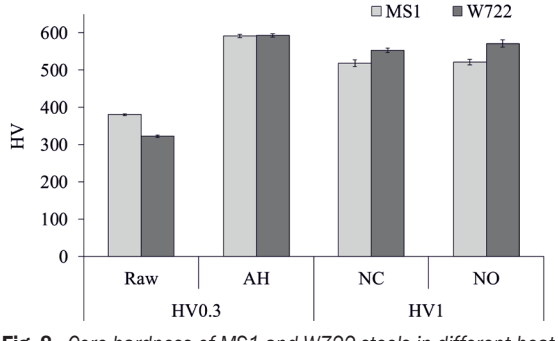

Fig. 8. *Core hardness of MS1 and W722 steels in different heat treatment conditions*

The decrease of hardness due to nitro-carburizing compared to age hardening is higher for MS1 (50HV) than for W722 (30HV). Therefore, over-ageing during nitro-carburizing is stronger in the case of MS1 than in the case of W722, i.e. greater reduction of hardness can be expected in the case of the MS1 steel. Nhd was determined in the cases of both materials and both nitriding processes, resulting in Nhd = 0.13 mm for MS1, and Nhd = 0.12 mm for W722 steel.

2.3.2 MS1 – 1.2343 Hybrid Part

In earlier research [24], authors produced hybrid structures using commercial tool steels of different chemical compositions and heat treatment specifications. Heat treatment was used in the different steps of the manufacturing process, and the residual stresses generated during processing were described based on deformation measurements. The authors concluded that hardening is suggested before sintering in all cases when the DMLS process is applied on a raw material different than that of a maraging type tool steel, and the prescribed surface hardness value of the mould is similar. Otherwise, substantial internal stresses in the material would be generated during the high-temperature heat treatment after construction [24].

In this paper, MS1 steel powder was sintered onto both the untreated and the quenched 1.2343 steel plates. In the case of untreated (raw material) base plates, the hybrid part was first quenched and double tempered, followed by nitro-carburizing. In this case, the hardness of both materials was ~600HV, while in the case of a quenched base plate and a hybrid part subjected only to nitrocarburizing, the hardness of the sintered MS1 material was altogether ~380HV.

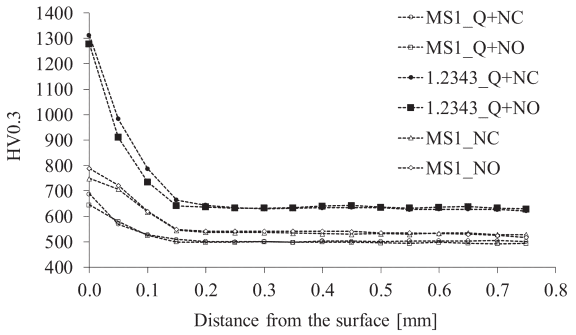

Fig. 9. *HV0.3 microhardness profile of nitrocarburized (NC) and oxy-nitrided (NO) steels*

The nitro-carburizing hardness profile clearly shows that the hardness of the quenched and nitrocarburized 1.2343 material at a distance of 0.05 mm from the surface is ~200HV higher than that of the nitro-carburized MS1 steel (Fig. 9.) because of the higher amount of nitride-forming elements and carbon concentration.

The hardness at a distance of 0.05 mm from the surface of the maraging steel that was quenched and then nitrocarburized was ~200HV lower than that of the MS1 steel subjected only to nitrocarburizing. This can be explained with two phenomena of the over-aging caused by the long holding time of the Q-type heat treatment; (i) the metastable martensite reversion into austenite and (ii) the coarsening of the intermetallic precipitates.

2.4 Transition Zone in Hybrid Structures

The quality of the transition zone in the case of hybrid tool inserts has outstanding importance in terms of operation and lifetime. In order to avoid the wear of the tool locally, the hardness of the transition zone cannot deviate significantly from the homogeneous parts of the tool. In our experiments, MS1-W722 and MS1-1.2343 hybrid samples were tested. Microscopic analysis (Fig. 10) and HV0.3 hardness measurements were carried out on the transition zone and its environment.

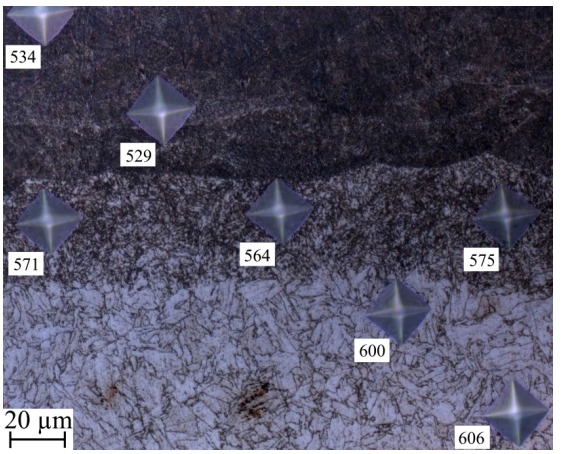

Fig. 10. *Microstructure of the age-hardened MS1-W722 hybrid part (W722 on the bottom, MS1 on the top and the transition layer in the middle) with the traces and resulted values of HV0.3 hardness measurement*

As seen in Fig. 10, the transition zone, which was melted by the laser beam during the sintering, resulted in a finer structure of W722.

Based on our results, the hardness of the transition layer of the MS1-W722 hybrid part after age hardening can be expected between the hardness

values of the homogeneous base materials. The hardness of the boundary layer between the MS1 and the 1.2343 in the hybrid structure is slightly lower than that of base materials (Fig. 11).

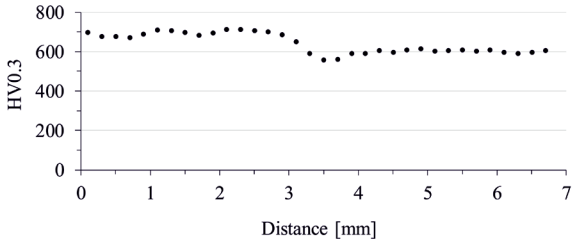

Fig. 11. *HV0.3 hardness measurement in the cross-section of the MS1-1.2343 sample*

Scanning electron microscopy combined with EDS analysis was used to study the transition layer in the MS1-1.2343 hybrid part (Fig. 12).

In the case of this material combination, the transition zone cannot be seen as clearly as in the case of MS1-W722. Element map analysis was carried out, and the Ni and Cr distribution was studied to characterize the transition layer.

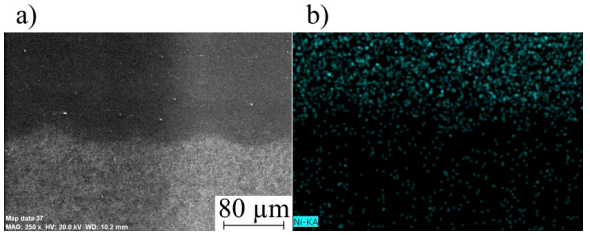

Fig. 12. *a) SEM image (MS1 – top, 1.2343 – bottom) and b) Ni element map of EDS analysis of the MS1-1.2343 hybrid part*

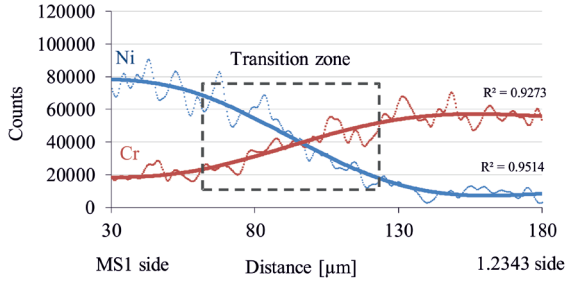

Fig. 13. *Changing the Ni and Cr element concentration from the MS1 side to the 1.2343 material*

The element concentration of Ni and Cr alloying elements in different cross sections from the MS1 side to the 1.2343 side was characterized by image analysis with the use of the element map images (Fig. 13). The values on the y-axis of the diagram correlate with the quantity of the elements in the appropriate cross section. The concentration of the elements changes continuously in the transition layer, which can ensure the correct interfacial properties, but more investigations are needed to verify this.

2.5 Porosity

Polished cross-sectional surfaces of the hybrid parts were examined with an optical microscope, revealing pores of micrometre size on the MS1 side of the part (Fig. 14.). The area-related amount of porosity can be determined in the microscopic image. The 0.32% porosity of the sintered MS1 part decreased after nitro-carburizing to 0.28 %.

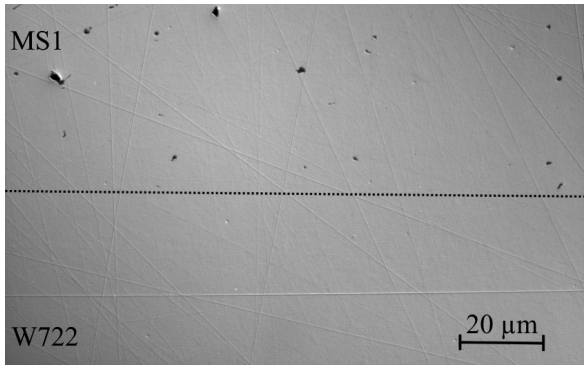

Fig. 14. *Morphology and location of the pores on the polished cross-section of the DMLS material*

2.6 Wear Test

Wear tests were carried out on age-hardened polished MS1 samples with the same normal load and different duration time (10 min, 20 min, 30 min, 60 min, 120 min, 240 min).

To evaluate wear resistance and characterize the time-dependent nature of the wear process, wear track depth, and the cross-sectional area of wear with 2D profile diagrams were determined. Fig. 15 shows these two parameters as a function of time.

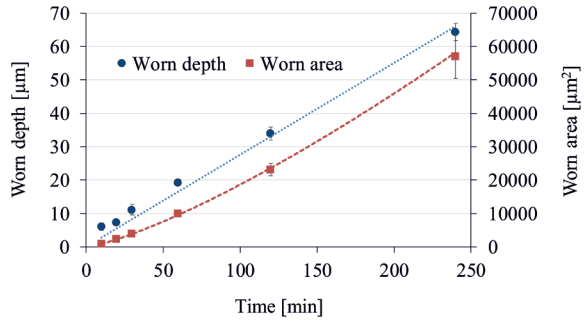

Fig. 15. *Depth of wear track and the worn area as a function of sliding time*

Material loss after an initial burn-in phase is considered to be linear. Taking these results into account, we performed the subsequent tests for a sliding time of 60 min.

Fig. 16. shows the results of the three material grades for different heat treatments.

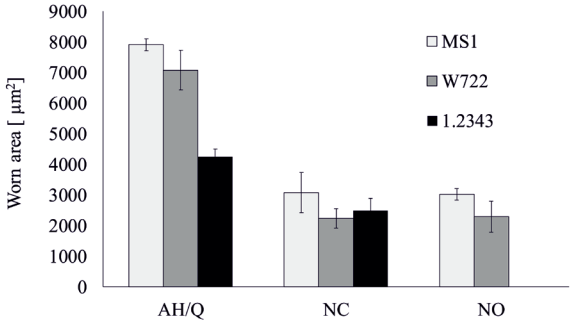

Fig. 16. *The measured values of the worn area of MS1, W722 and 1.2343 steel in age hardened or quenched (AH/Q); nitrocarburized (NC) and oxy-nitrided (NO) conditions*

The worn area decreased significantly after nitro-carburizing and oxy-nitriding, thus providing higher wear resistance. In addition, wear resistance was higher for the W722 material compared to that of the MS1 steel for all the investigated heat treatment conditions.

Compared to the quenched and tempered 1.2343 steel, a worn area twice the size was measured in case of age-hardened MS1 steel, which can clearly be attributed to the higher hardness of conventional steel. The lower wear resistance of the sintered and nitrocarburized MS1 materials compared to that of the nitrocarburized, and Q+2T treated 1.2343 steel can be explained with the presence of micro-porosity, while the cause of the lower hardness of MS1 is over-ageing during nitro-carburizing.

As a result of nitrocarburizing, the wear resistance of MS1 and W722 steels was improved by ~65 % compared to their wear resistance without surface treatment. The wear test results of hybrid model structures composed of differently heat-treated base plate and insert materials suggest that nitriding and nitro-carburizing are effective ways of increasing the wear resistance of hybrid tool inserts.

3 CONCLUSIONS

We used DMLS to produce hybrid structures combining conventional processing technology with rapid prototyping. W722 maraging steel of equivalent chemical composition as the sintering powder and 1.2343 conventional tool steel were selected as base materials, and MS1 maraging steel powder was used for laser sintering. Different heat treatments (age hardening, quenching, quenching with double tempering, nitro-carburizing and oxy-nitriding) were applied after production. We characterized the microstructure, hardness and wear properties of the different steels, and studied the hybrid structures and analysed them from a tribological point of view.

We showed that the different manufacturing processes resulted in different microstructures in the case of laser-sintered and hot-rolled maraging steels, as well as the higher porosity of the laser-sintered material. Comparing the effect of age hardening and quenching on the hardness of the different steel grades, we found that age-hardening results in almost the same hardness as quenching in maraging steels, while the same heat treatment resulted in softening in the case of 1.2343 steel. Quenching produced the same hardness as age hardening in MS1 steel. Heat treatment parameters have a significant impact on the mechanical properties. In the case of hybrid structures, it is necessary to select heat treatments and heat-treating parameters that produce the required properties in both components.

The transition zone of both the MS1-W722 and MS1-1.2343 hybrid parts was studied. EDS analysis showed continuous changing of element concentration in the transition zone. There is no sharp boundary between the two materials in the hybrid part, neither in the microstructure nor in the mechanical properties.

We confirmed experimentally that laser-sintered parts possess higher porosity compared with conventionally made steels, which explains the lower wear resistance of MS1 samples, compared to W722 maraging steel samples made from a conventionally produced steel bar.

The higher wear resistance of 1.2343 steel compared to that of maraging steel can be ascribed to its higher carbon content, and its higher attainable surface hardness. When nitro-carburizing was applied, the worn area, which is an indication of wear resistance, dramatically decreased and nearly the same value was achieved for all steels. The sintered maraging steel showed lower wear resistance than its conventionally produced counterpart did in all cases, which can be explained with the higher porosity as a result of sintering.

Our results indicate that nitro-carburizing provides an effective way to increase the wear performance of hybrid tools.

We showed that if tool steel is used in hybrid constructions requiring quenching to assure the prescribed properties, this heat treatment can produce

the same hardness in the MS1 part as age hardening can when high-temperature tempering is applied after quenching.

4 ACKNOWLEDGEMENTS

The research presented in this paper was supported by EFOP 3.6.1-16-2016-00017 and EFOP-3.6.2-16-2017-00016; and it was carried out as part of the GINOP-2.3.4-15-2016-00004 project, aimed to promote the cooperation between the higher education and the industry.

5 REFERENCES

[1] Mayer, S. (2005). Optimized mould temperature control procedure using DMLS, *EOS Whitepaper.* EOS, Krailing, Munich.

[2] Ilyas, I., Taylor, C., Dalgarno, K., Gosden, J. (2010). Design and manufacture of injection mould tool inserts produced using indirect SLS and machining processes. *Rapid Prototyping Journal*, vol. 16, no. 6, p. 429-440, **DOI:10.1108/13552541011083353**.

[3] Hassan, H., Regnier, N., Pujos, C., Arquis, E., Defaye, G. (2010). Modeling the effect of cooling system on the shrinkage and temperature of the polymer by injection molding. *Applied Thermal Engineering*, vol. 30, no. 13, p. 1547-1557, **DOI:10.1016/j.applthermaleng.2010.02.025**.

[4] Agazzi, A., Sobotka, V., LeGoff, R., Jarny, Y. (2013). Optimal cooling design in injection moulding process – A new approach based on morphological surfaces. *Applied Thermal Engineering*, vol. 52, no. 1, p. 170-178, **DOI:10.1016/j.applthermaleng.2012.11.019**.

[5] Hassan, H., Regnier, N., Le Bot, C., Defaye, G. (2010). 3D study of cooling system effect on the heat transfer during polymer injection molding. *International Journal of Thermal Science*, vol. 49, no. 1, p. 161-169, **DOI:10.1016/j.ijthermalsci.2009.07.006**.

[6] Santos, E.C., Shiomi, M., Osakada, K., Laoui, T. (2006). Rapid manufacturing of metal components by laser forming. *Internal Journal of Machine Tools & Manufacture*, vol. 46, no. 12-13, p. 1459-1468, **DOI:10.1016/j.ijmachtools.2005.09.005**.

[7] Shellabear, M., Nyrhilä, O. (2004). DMLS – Development history and state of the art, LANE 2004 Conference, from *https://www.i3dmfg.com/wp-content/uploads/2015/07/History-of-DMLS.pdf* accessed on 2017-09-18.

[8] Pinkerton, A.J. (2016). Lasers in additive manufacturing. *Optics & Laser Technology*, vol. 78, part A, p. 25-32, **DOI:10.1016/j.optlastec.2015.09.025**.

[9] Siddique, S., Imran, M., Rauer, M., Kaloudis, M., Wycisk, E., Emmelmann, C., Walther, F. (2015). Computed tomography for characterization of fatigue performance of selective laser melted parts. *Materials & Design*, vol. 83, p. 661-669, **DOI:10.1016/j.matdes.2015.06.063**.

[10] Baumers, M., Truck, C., Wildman, R., Ashcroft, I., Rosamond, E., Hague, R. (2012). Combined build-time, energy consumption and cost estimation for direct metal laser sintering. *Proceedings of the Solid Freeform Fabrication Symposium*, p. 932-944.

[11] Boivie, K., Karlsen, R., Ystgaard, P. (2012). The concept of hybrid manufacturing for high performance parts. *The South African Journal of Industrial Engineering*, vol. 23, no. 2, p. 106-115, **DOI:10.7166/23-2-334**.

[12] Wallis, C., Buchmayer, B., Kitzmantel, M., Brandstätter, E. (2016). Additive manufacturing of maraging steel on a copper substrate using selective laser melting. *Metal Additive Manufacturing Conference Proceedings*.

[13] Shetty, K., Kumar, S., Rao, P.R. (2009). Effect of ion nitriding on the microstructure and properties of Maraging steel (250 Grade). *Surface and Coating Technology*, vol. 203, no. 10-11, p. 1530-1536, **DOI:10.1016/j.surfcoat.2008.11.034**.

[14] Cajner, F., Landek, D., Leskovšek, V. (2010). Surface modifications of maraging steels used in the manufacturing of moulds and dies. *Materials and Technology*, vol. 44, no. 2, p. 85-91.

[15] Wen, D.C. (2009). Microstructure and corrosion resistance of the layers formed on the surface of precipitation hardenable plastic mold steel by plasma-nitriding. *Applied Surface Science*, vol. 256, no. 3, p. 797-804, **DOI:10.1016/j.apsusc.2009.08.062**.

[16] Hatos, I., Hargitai, H. (2013). Manufacturing process for injection molding insert with conformal cooling. *A Jövő Járműve*, vol. 03-04, p. 95-97. (in Hungarian)

[17] Böhler Data Sheet (2009). *W722 VMR Maraging High Stength Steel*, Böhler Edelstahl, Kapfenberg.

[18] Böhler Data sheet (2005). *W300 Hot Work Tool Steel*, Böhler Edelstahl, Kapfenberg

[19] Material Data sheet (2007). *EOS MaragingSteel MS1 for EOSINT M270 Systems*, EOS, Krailling, München

[20] ASM Materials Information (1991). *ASM Handbook, Heat Treating*, vol. 4, p. 528-548.

[21] Kempen, K., Yasa, E., Thijs, L., Kruth, J.-P., Van Humbeeck, J. (2011). Microstructure and mechanical properties of selective laser melted 18Ni-300 steel. *Physics Procedia*, vol. 12, part A, p. 255-263, **DOI:10.1016/j.phpro.2011.03.033**.

[22] MSZ EN ISO 6507-1:2005 Standard: *Metallic materials – Vicker Hardness test – Part 1: Test method.* International Organization of Standardization, Geneva

[23] Hatos, I., Hargitai H., Solecki L. (2015). Study of 2D and 3D methods for worn surface analysis of tool materials. *Acta Technica Jaurinensis*, vol. 8, no. 2, p. 165-178, **DOI:10.14513/actatechjaur.v8.n2.373**.

[24] Hatos, I., Hargitai, H., Kovacs, J. G. (2017). Characterization of internal stresses in hybrid steel structures produced by direct metal laser sintering. *Materials Science Forum*, vol. 885, p. 196-201, **DOI:10.4028/www.scientific.net/MSF.885.196.**

Strojniški vestnik - Journal of Mechanical Engineering 64(2018)2, 130-143
DOI:10.5545/sv-jme.2017.5061
Original Scientific Paper
Received for review: 2017-11-07
Received revised form: 2017-12-12
Accepted for publication: 2017-12-21

Judging Method of Tooth Damage Behavior of the High Speed Milling Cutter

Minghui Zhang – Minli Zheng* – Bin Jiang
Harbin University of Science and Technology, National & Local United Engineering Laboratory of High Efficiency Cutting and Tools, China

In the actual processing of the high speed milling cutter, due to the local damage of milling cutter components, the security and the decline in service life of the milling cutter generally exist, which seriously restricts its technical advantages of high-efficiency and high-precision processing. The tooth damage of the milling cutter is fuzzy and uncertain, which brings obstacles to the improvement of security stability and working efficiency of the milling cutter. The high speed milling cutter is subjected to high centrifugal force and cutting load during the milling process, resulting in damage to the milling components. Based on the material mechanical properties of milling cutter components and the impact experiment under a high strain rate, the damage types and formation mechanism of the milling cutter are analyzed, and the milling cutter damage model is established. The damage equivalent weight is adopted to quantitatively evaluate the damage degree of milling cutter teeth. Finite element simulation is used to find the vulnerable part of the milling cutter in high speed milling. Then the evolution process of milling cutter damage is analyzed, and the recognition and judgment method of milling cutter damage behavior is put forward, and lastly, this judgment method concerning the milling cutter damage is verified through experiment.

Keywords: high speed milling cutter, component material, strain rate, damage model

Highlights

- *Damage types and indexes were identified for the high speed milling cutter.*
- *A model that can calculate milling cutter damage under the centrifugal force, the dynamic cutting force and the pre-tightening force was established.*
- *The initial and the critical damage values were obtained by the cutting simulation and the high speed milling test.*
- *Damage behavior features of the milling cutter components materials were analyzed.*
- *A recognition and judgment method of milling cutter damage behavior was put forward.*

0 INTRODUCTION

With high efficiency, good quality and low energy consumption, the high speed milling technology represents the main development direction of the mold manufacturing [1] and [2]. In particular, the high speed milling cutter has been widely applied in the manufacturing field because of its superior performances and economic advantages [3]. Safety stability is not only the high-performance requirement of high speed milling cutter at a high level, but also the basis of the high speed and stable cutting. It not only fully demonstrates the safety state and performance of the milling cutter in the high speed cutting process, but also can comprehensively reflect the product economy and social satisfaction degree of the milling cutter [4]. It is the final criterion to examine whether the high speed milling cutter can meet the safety requirements of high efficiency and high precision machining of key components. Therefore, the damage mechanism of the high speed milling cutter is studied to prolong the safe and stable cutting time and improve milling efficiency and machining quality, which provides an important theoretical basis and engineering value for the design of more efficient and safer cutting tools, and also plays a positive role in the development and application of the high speed milling technology.

At present, the guidance documents on the safety of high speed milling cutters all over the world mainly adopt the international standard ISO 15641 [5]. This method ensures the safe and stable operation of the high speed milling cutter, which is the prerequisite for high speed milling. However, this method can neither reveal the dynamic process of the decline in the safety of the high speed milling cutter, nor make clear the evolution process of the performance decline of the milling cutter caused by the damage of the milling cutter components such as the joint surface and screw.

The damage is the change of the local performance of the cutter body components caused by various external factors, which degrades the performance of the milling cutter. The cutter damage evolves from the micro defects in the material, and under the comprehensive action of the fatigue effect and the overload effect of the cutting load, when the micro damage accumulates to a certain extent, the vulnerable and unstable state may be broken at any time, and then massive macroscopic damage appears [6]. Li et al. [7] established an application research framework centering on in geometry, computer

*Corr. Author's Address: Harbin University of Science and Technology., Xuefu Road 52, Harbin, China, mh_zhang610@hotmail.com

simulation and finite element analysis based on the proposal of a small-to-large (micro structure - material structure - component structure) hierarchical multi-scale analysis method. Then the macro-mechanical response of the microstructure of the polycrystalline material was obtained, and the mechanical properties of the material were predicted. Cheng et al. [8] and Ge [9] proposed a microelement method suitable for the micro-macro scale-span analysis of new materials with the micro structure, which can realize the direct transition analysis from the material micro structure to the component macro response. Barabash et al. [10] studied the microstructural evolution of tool materials and revealed the inherent relationship between the geometric construction of the microstructure component, micro crack behavior and microstructure failure. Birck et al. [11] analyzed the characteristics in the damage process using the grid discrete element method. Jiang et al. [12] carried out the molecular dynamics simulation to simulate the mesoscopic state of the milling cutter and its components under different stress conditions using MAPS software. It was found that the sensitivity of the mesoscopic motion to external stress was different. Based on this, a quantitative analysis of the safety of the milling cutter was conducted, and then an evaluation model of milling tool efficiency life was established. In summary, the material damage of milling cutter components is imperceptible in the early formation stage, and it has more mesoscopic and microscopic characteristics.

Because the milling cutter has many design parameters, among which there are strong correlations, it is still difficult to fundamentally improve the tool structure form in order to improve the stability and cutting efficiency of the milling cutter. At present, it is more appropriate to optimize the corresponding parameters according to the specific functional requirements, and the goal is the form of driving, which is the design concept of the milling cutter [13] and [14]. However, on the one hand, the optimization of parameters depends on empirical formulas and test data. On the other hand, there is a lack of scientific theories, and there are many ways to solve this problem at home and abroad, such as the parametric design method, TRIZ method [15], and axiomatic design method [16] and [17]. Although these methods play a certain guiding role in the decoupling of the milling cutter design technology, how to translate this abstract solution into a practical solution becomes the primary difficulty. In practical application, it is not fully developed, and it is still necessary to carry out further study.

The damage of the high speed milling cutter will lead to the changes in dynamic characteristics of the tool structure, which will be reflected by the different damage indexes of the milling cutter. By identifying the damage types, the state of the milling cutter before and after damage can be visually compared. Therefore, obtaining all kinds of damage indexes is the key factor to analyze the damage of the milling cutter. In this paper, a new physical quantity of equivalent damage is introduced, which directly reflects the damage evolution process in the system unit. By studying the relationship between various damages and the safety of milling cutters, an effective way to restrain the damage of high speed milling cutters is provided.

1 METHODOLOGY, OBJECTIVE, AND SCOPE OF THE RESEARCH

The performance of the high speed milling cutter mostly depends on several factors, such as, the materials composing the cutter components, the cutter structure, the selection of the insert coating and the rationality of the design [17]. Among them, the materials of the cutter components are its inherent attribute which is the precondition for studying the

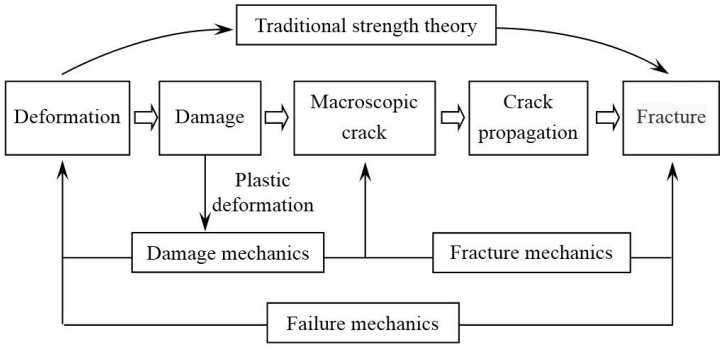

Fig. 1. *Theory of damage analysis of milling cutter materials*

damage of the milling cutter. The study on the damage mechanism of the high speed milling cutter is carried out on the basis of damage mechanics shown in Fig. 1. This paper studies the process of the deformation, development and destruction of the cutter materials along with the cutter when the cutter is subject to different external loads.

Starting from materials science, the macroscopic physical properties of the component materials of the high speed milling cutter are determined by its own atoms or molecules. The performance of the cutter can vary significantly depending on the properties of materials [18]. Therefore, the properties of the cutter components are very important for the cutting performance of the cutter. In fact, the damage has already been in existence in the manufacturing, production and processing of the material processing. The initial damage is inherent in the material itself, and the microcrack expansion rate is determined by the external load. As a result, the damage value depends on the material properties and the structural parameters of the cutter components. The various components of the high speed face milling cutter are not mutually independent. Instead, there is a connection structure. In addition, the functions of each component are different. Therefore, according to the actual role of the high speed milling cutter in the cutting process, the functions of the milling cutter includes the connecting of the cutter bar to the milling cutter and the machine tool, the connecting of the screw to the insert, the connecting of the screw to the cutter body, the supporting of the milling cutter body and the cutting of the insert.

The high speed milling cutter is connected to the tool system in the cutting process. Thus, there is a constraint relationship between the cutter and the tool system. The principal axis direction is stipulated as Z-axis, the feed direction as X-axis and the line spacing direction as Y-axis. During the cutting process, the loading of the milling cutter mainly include the centrifugal force formed by the high-speed tool rotation, the pretightening force to tighten the screw and the cutting force imposed on the cutting edge. The forces are illustrated in Fig. 2.

In Fig. 2, F_z is the pre-tightening force imposed to the milling cutter mounting surface; P_e is the centrifugal force, n is the spindle speed, F_{ic} is the transient cutting force imposed to the cutting teeth, M_d is the running torque of the milling cutter, F_{id1} is the force imposed to the junction surface of the cutter body and insert side, F_{id2} is the force imposed to the junction of the cutting edge and the insert bottom, M_{i0} is the bending moment of the screw and F_{i0} is the force imposed to the junction of the screw and the insert.

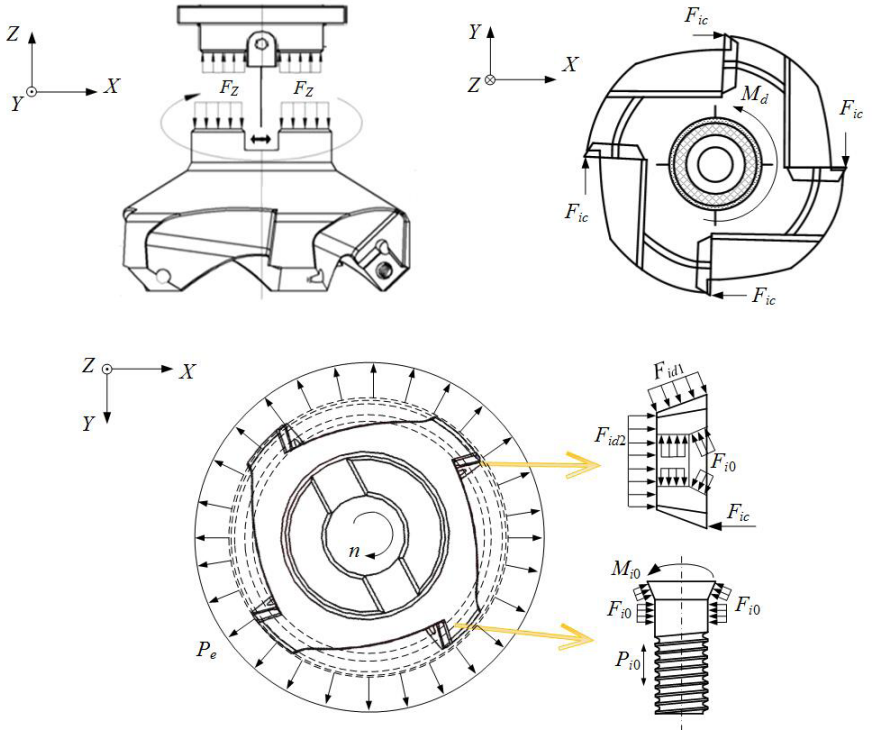

Fig. 2. *Force analysis in the cutting process of the milling cutter*

In high speed milling, the cutting force is directly imposed to the insert and is transmitted and distributed to the milling cutter components. The different loads of each component of the milling cutter lead to, the deformation of different properties of the locating surface of the cutter body and insert, and the joint surface of the insert and screw occurs, and the damage of different attributes can be further developed.

2 MODEL OF DAMAGE EVOLUTION OF THE MILLING CUTTER

In addition to the structure of the cutting tool, the critical damage value of the cutter components materials is the inherent nature of material itself. The equivalent volume element is adopted to establish the damage RVE model. It is assumed that the cutting tool material is isotropic, and the triaxial stress does not change over time. The initial defect expands from the microcrack and the initial damage of the RVE model starts to form.

The stress of the equivalent damage is adopted and the triaxial stress state is simplified to a uniaxial stress state unit model. The elastic strain energy density of the two models is the same. Considering the unilateral condition of crack closure, the equivalent damage stress can be expressed as:

$$\sigma^* = \sqrt{(1+\mu)\sigma^+ + \frac{1-D}{1-hD}\left((1+\mu)\sigma^- - \mu\sigma^2\right)}, \quad (1)$$

where σ^* is the equivalent damage stress; μ is the Poisson's ratio of the milling cutter component material; σ is the stress tensor of the triaxial state; D is the damage value of the milling cutter, and h is the microdefect closure parameter.

The initial damage value and the critical damage value are assumed to be the inherent properties of the milling cutter. For the selected milling cutter component, the microcrack propagation velocity is determined by the external load. The change of the RVE damage value of the milling cutter with the stress is shown in Fig. 3.

It can be seen from Fig. 3 that the damage value at the starting point of the curve is close to zero. It is believed that the damage value at this starting point is the initial damage value of the cutter materials. As the stress increases and exceeds a certain value, the damage value grows accordingly and then rises rapidly. The damage critical value depends on the material properties of the high speed milling cutter components and the deformation properties of the milling cutter. The damage value of RVE is determined by the material properties of the milling cutter components and the structure parameters of the material. The analysis indicates that the overall trend of the milling cutter damage is that the value of equivalent damage grows with the increase of the stress.

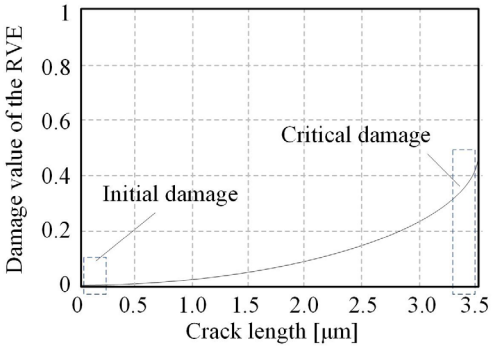

Fig. 3. *Model of damage of the milling cutter changing with stress*

A sliding crack model based on micromechanics theory is adopted to solve the problem of crack propagation under the compressive stress. A representative study of the crack performance under the compressive stress is the sliding crack morphology presented by Horii et al. [19], which is shown in Fig. 4. The curved microcrack is replaced by a straight line, and the open crack is generated at the tip of the microcrack. The axial compressive stress does not directly determine the expansion direction of the initial open crack, and there is a great angle between them. When the microcrack evolves into the medium term, the open crack will extend in the direction of the axial compressive stress. And when the open crack extends in the direction of the maximum axial compressive stress, its geometrical characteristics are obtained. The length of the initial microcrack is $2c$; the angle between the initial microcrack and the maximum axial compressive stress is θ, and the length of all the open cracks is l.

In a damage system, each micro void or microcrack is considered as a quasiparticle, whose evolution can be described in the damage state space. In the phase space, the state variable can be the dimension and orientation of the micropores or microcracks as well as the position coordinates of real space. Let $n(P_i, Q_i)$ be the number density of the microdamage. According to the law of conservation, the evolution of the damage can be expressed as:

$$\frac{\partial n}{\partial t} + \sum_i \frac{\partial (nP_i)}{\partial P_i} + \sum_i \frac{\partial (nQ_i)}{\partial Q_i} = n_N - n_A, \quad (2)$$

where n_A is the nucleation rate of the microdamage; n_N is the elimination coefficient caused by the convergence and healing of the microdamage; P_i is the damage evolution sensitivity; Q_i is the degree of insensitivity to damage evolution. The time rate can be taken as 0 and the nucleation rate before the damage critical period can also be viewed as 0. Eq. (2) can be rewritten as:

$$\frac{\partial n}{\partial t}+\sum_i \frac{\partial\left(nP_i\right)}{\partial P_i}=n_N. \tag{3}$$

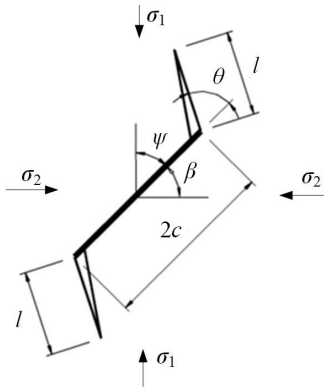

Fig. 4. *Sliding model of the microcrack*

The cyclic mechanical load in high-speed milling causes the accumulation of the milling cutter damage, which first appears at the micro meso level, eventually leading to the macroscopic fatigue crack propagation in the macro level of the tool materials. All these will produce damages. The initial defects existing in the high-speed milling cutter and its component material unit are mainly microcracks. It is assumed that these cracks are evenly distributed and interact with each other. Considering the interaction between microcracks, the sliding microcrack model including the sliding microcrack array under the stress state is established. The strains ε_1 and ε_2 caused by axial compressive stress σ_c can be expressed as:

$$(\varepsilon_1,\varepsilon_2)^T=(\varepsilon_1^e+\Delta\varepsilon_1,\varepsilon_2^e+\Delta\varepsilon_2)^T, \tag{4}$$

where ε_1^e and ε_2^e are the elastic strains in the undamaged condition. $\Delta\varepsilon_1$ and $\Delta\varepsilon_2$ are the total loss strain caused by the initial microcrack slip and the sliding crack propagation. The elastic strain is shown in Eq. (5).

$$(\varepsilon_1^0,\varepsilon_2^0)^T=\frac{(\kappa+1)(\mu+1)}{4E}\begin{bmatrix}1 & \frac{\kappa-3}{\kappa+1}\\ \frac{\kappa-3}{\kappa+1} & 1\end{bmatrix}(\sigma_c,0)^T, \tag{5}$$

where E is the elasticity modulus of the cutter material and μ is the Poisson's ratio of the cutter material.

$$\begin{cases}\kappa=3-4\mu & \text{(plane strain)}\\ \kappa=\left[(3-\mu)(1+\mu)\right] & \text{(plane stress)}\end{cases}. \tag{6}$$

Since the current problem is a linear one, it can be considered that the damage strain is relevant to the fact that the externally loaded axial stress σ_c is linear. It is assumed that there are N initial microcrack defects in the cutter material unit model. The interaction between the micro cracks is not considered. Then, the total damage strain of the tool material unit can be written as:

$$(\varepsilon_1,\varepsilon_2)^T=\left((\varepsilon_1^0,\varepsilon_2^0)^T+N\begin{bmatrix}S_{11} & S_{12}\\ S_{21} & S_{22}\end{bmatrix}\right)(\sigma_c,0)^T, \tag{7}$$

when $\varepsilon_1=\varepsilon_2$, there is:

$$\sigma_c=\frac{E\varepsilon}{1+ENS_{11}}. \tag{8}$$

It can be seen that under the effect of axial compressive stress, the strain of the material is controlled by the elasticity modulus, and the elastic modulus at this time is smaller than that in the case of damage accumulation. E_D is adopted to define the material unit damage. Then, Eq. (8) can be simplified as:

$$\sigma_c=E_D\varepsilon=E(1-D)\varepsilon. \tag{9}$$

Therefore, the damage of the milling cutter component unit can be obtained through solving Eq. (8) and (9) simultaneously. The equation is as follows:

$$D=1-\frac{E}{1+ENS_{11}}. \tag{10}$$

The effective stress in the damage state can be obtained by applying the equivalent damage value D and the equivalent damage stress conducive to analyzing the mechanism of the milling cutter damage.

3 RESULTS

3.1 Cutting Tool Materials

This paper analyzes the milling cutter damage formation and evolution process taking the indexable four-tooth high speed face milling cutter with a diameter of 63 mm and equal teeth distance as an example. Its tool cutting edge angle is 45°, flank angle is 20°, rake angle is 0°, and edge inclination angle is 10°. The shape of the milling cutter is shown in Fig.

5. The cutter components include the cutter body, the corresponding materials of the screw and the cutting edge materials. The mass fractions of the elements in the materials are listed in Tables 1 and 2.

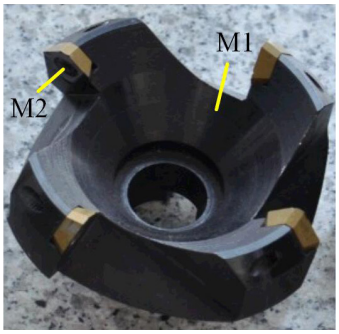

Fig. 5. *Four-tooth high speed face milling cutter with a diameter of 63 mm*

Table 1. *Chemical composition of the materials in the milling cutter body and screw*

Components	C	Si	Mn	Cr	Ni	P	S
M1	0.45	0.27	0.73	1.10	0.27	0.03	0.03
M2	0.39	0.21	0.64	1.08	0.15	0.03	0.02

Table 2. *Chemical composition of the materials in the milling cutting edge*

Component	W	C	Co	O
Insert	68.67	21.77	7.54	2.02

3.2 Damage Behavior Features of the Milling Cutter Components

The tensile and compression tests of the cutter component materials were carried out on a WDW-200 computer control electronic universal testing machine under the same load level and the stress-strain curves are shown in Fig. 6. The shape of the stress-strain curve in Fig. 6 reflects the various deformation processes of the materials, including the elastic deformation stage, the plastic deformation stage, the necking deformation stage and the strengthening stage under the action of external load.

The traditional material mechanics strength theory has limitations. It is learned from ordinary physics that atoms interact with each other: when the atomic spacing is small, they repel each other; when the spacing is large, they attract each other. The cutter materials are damaged when the binding force between atoms are overcome. The distance increases with the growth of the stress value. When the stress overcomes the binding force between atoms and reaches the maximum value σ_m of the action force, this value is the theoretical fracture strength.

However, numerous test results and engineering applications indicats that the actual fracture strength of the material is one to three orders of magnitude smaller than the theoretical fracture strength, which is because there must be various defects in the actual materials, such as microscopic cracks, vacancies, incisions, and scores, to decline the safety and stability of the tool and reduce the tool life. For the real milling cutter component materials, the ductile fracture process under tensile stress is the process of pulling the atoms apart along the direction which is vertical to the tensile stress. The approximate calculation formula of the microcrack intensity σ_t of the material can be approximated as:

$$\sigma_t = \left(K_m / \sqrt{2\pi}\right) \cdot \left(1/\sqrt{r_{ij}}\right) \cdot \tilde{\sigma}_{ij}, \tag{11}$$

where K_m reflects the intensity level of the stress field near the tip of the insert cutting zone, ij reflects the second order tensor and r_{ij} reflects the second order tensor of the crack area. This formula stands for the stress solution in the crack area of the tool.

According to the stereoscan photograph of the test sample, which is shown in Fig. 7, the tensile fracture of each component of the milling cutter all presents as microporous aggregation fracture. Due to the intense slippage and the dislocation pileup, many micro voids are frequently seen in local area, or there

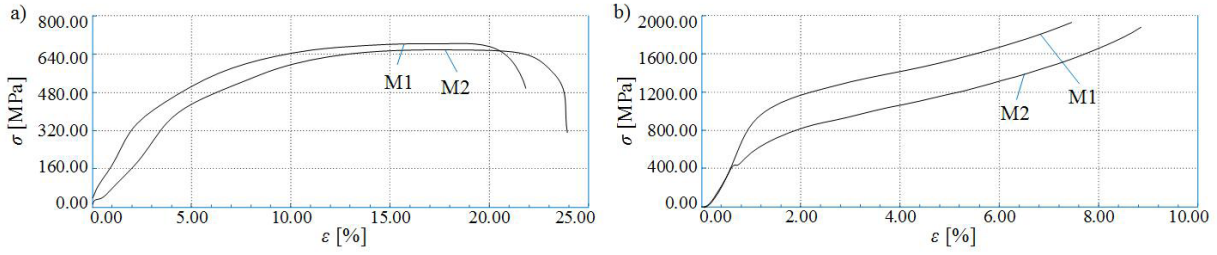

Fig. 6. *Formation and evolution of component material damage; a) tensile failure damage; and b) compression damage*

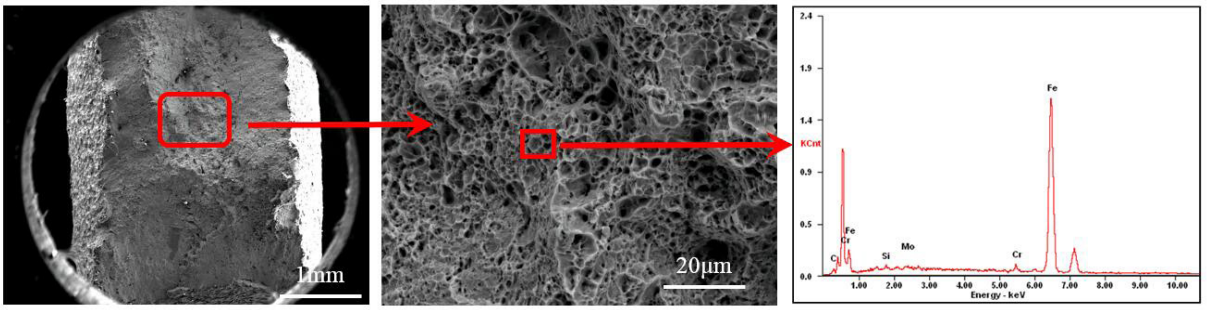

Fig. 7. *Scanning electron microscope observation and energy spectrum analysis*

are some impurities crushing, and fractures of foreign matters and base metal interface.

Fig. 7 shows that the fracture is not smooth, for the direction of crack propagation in the metal materials is relevant to the direction of maximum stress, and the crack propagation follows the path with the least resistance. The morphology and structure of the fracture directly record the occurrence of the fracture microcracks, the process of crack propagation and the ultimate moment of fracture. The fracture process of the tested materials develops from the local to the whole, including two processes: crack generation and crack propagation.

The mechanical responses of materials under different load conditions are quite different. Because the milling cutter is used for periodic intermittent cutting, the dynamic response under the impact load is needed. The stress-strain curve and strain rate were obtained by carrying out the impulse test to the milling cutter screw and cutter body materials under the impulsive pressures of 0.4 MPa, 0.6 MPa and 0.8 MPa using SHPB equipment. The stress-strain curves fitted by the stress-strain data collected using the data acquisition unit are shown in Figs. 8 and 9.

The transient waveform memory recorded the incident wave signal ε_i, reflected wave signal ε_r and

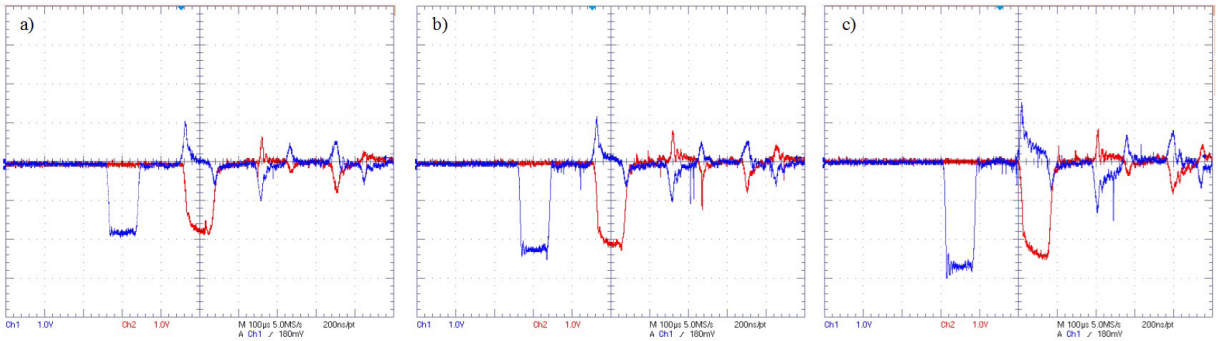

Fig. 8. *M1 waveform of the milling cutter components under the impact; a) 0.4 MPa; b) 0.6 MPa; and c) 0.8 MPa*

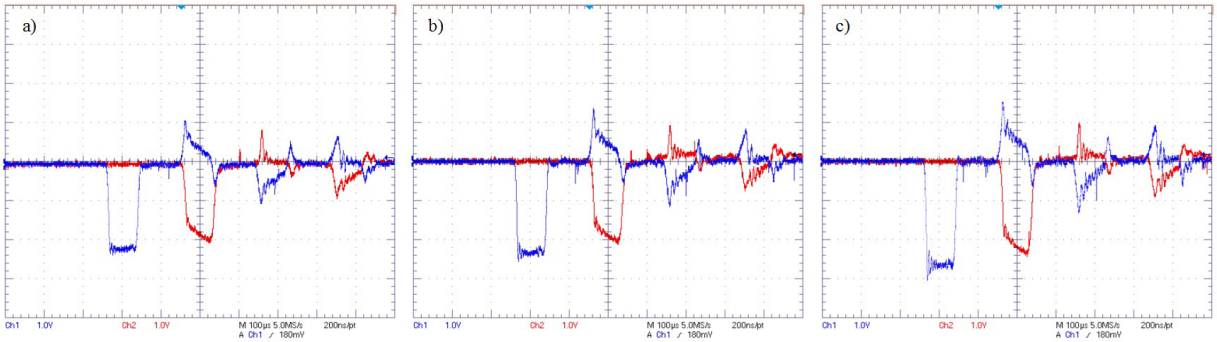

Fig. 9. *M2 waveform of the milling cutter components under the impact; a) 0.4 MPa; b) 0.6 MPa; and c) 0.8 MPa*

the transmitted wave signal ε_t. Based on the theory of stress wave, the three signals, ε_i, ε_r and ε_t confirm the stress-strain relationship of the material, as shown in Eq. (12).

$$\varepsilon_s = -\frac{2c_0}{l_0}\int_0^t \varepsilon_r \cdot dt, \tag{12}$$

where ε_s is the average strain; c_0 refers to the wave velocity of the one-dimensional stress wave propagation in the rod; l_0 is the initial length of the test piece; ε_r is the strain of the reflected wave.

The average stress in the test is:

$$\bar{\sigma} = E \cdot A \cdot \varepsilon_t / A_s, \tag{13}$$

where E is the elasticity modulus of the incident bar; A is the sectional area of the incident bar; A_s is the sectional area of the specimen.

The stress and strain data of M1 and M2 materials of the milling cutter components under the load condition are fitted to curves, which are shown in Fig. 10.

The impact surface of the tested specimen under the impact effect was observed under the scanning microscope. It is discovered that the defects of the material after the impact are more obvious. Excluding the defects of the materials, the surface of the tested specimen under the impact load presents as a wavy interface, which is the basic organizational characteristics after the impact is imposed. It can be seen from the stress-strain curves of the above materials that with the increase of the stress, the yield limit of the material began to be linear and when it reaches a certain value, the yield capacity weakens dramatically, and the deformation extent starts to intensify.

Under the various stress levels, the strain rates of the milling cutter components at a variety of impact levels are 231.0, 345.9, 891.5, 952.1, 1121.2, and 1311.9, respectively. It can be seen that the strain rates of the screw materials are lower than those of the cutter body materials, indicating that the screw materials have a poor capacity to withstand the load, while the cutter body materials have strong impact resistance ability.

The constitutive relation model of the milling cutter materials can be obtained using the Johnson-Cook (JC) model [20]. This model is suitable for a variety of conditions and can be used to describe the relationship between one function and its effect. Its basic form is as follows:

$$\sigma = [A + B(\bar{\varepsilon})^n]\left[1 + C\ln\left(\frac{\dot{\varepsilon}}{\dot{\varepsilon}_0}\right)\right]\left[1 - \left(\frac{T_\alpha - T_r}{T_m - T_r}\right)^m\right], \tag{14}$$

where A, B, C and m are constants; σ is the flow stress under nonzero strain rate; n is the work hardening index; $\bar{\varepsilon}$ is the equivalent plastic strain; $\dot{\varepsilon}$ is the equivalent plastic strain rate; $\dot{\varepsilon}_0$ is the reference strain rate, T_α is the test temperature, T_r is the reference temperature, T_m is the melting temperature.

After conversion and parameter fitting, the parameters of the JC model of the component materials of the milling cutter were obtained, as shown in Table 3.

Table 3. *Parameters of the JC model of the milling cutter components*

JC model variable	A [MPa]	B [MPa]	C	m	n
M1	20.516	61.367	0.0087	1.134	0.704
M2	19.452	57.423	0.0382	1.732	0.536

The strength of the material is the function of strain, strain rate and temperature. This model can be

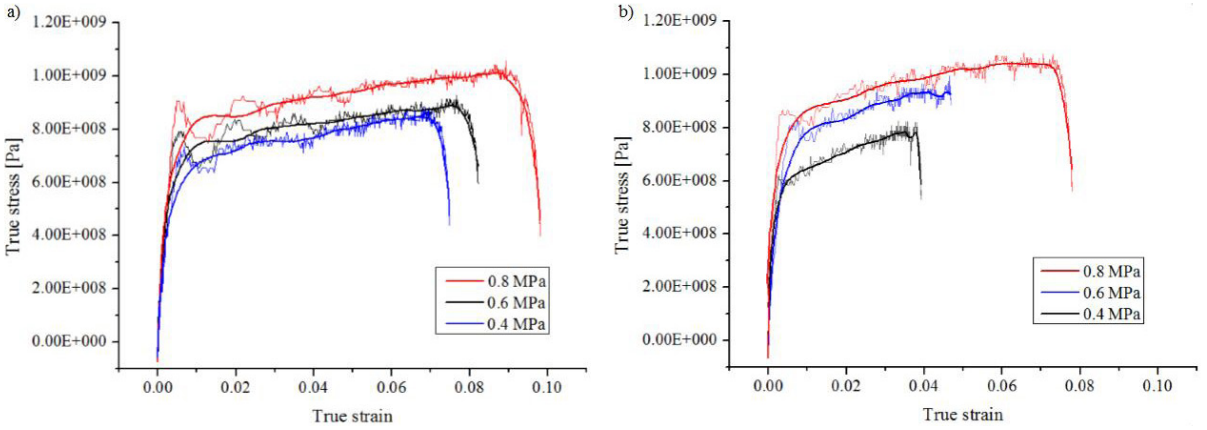

Fig. 10. *Strain-stress fitting curve of the milling cutter components; a) milling cutter material M1; and b) milling cutter material M2*

used to analyze the performance of the milling cutter materials and provide basis for studying the material conditions required in the various damages of the milling cutter.

The mechanical property of the component materials of the high speed milling cutter under a high strain rate and the stress-strain relationships of the component materials within the range of a high strain rate were obtained through the static load and impact experiment. These changing characteristics of the yield strength of component materials under different impact loads were analyzed and the rate of response of the materials to the external stress was obtained. All these provide experimental analysis basis to the milling cutter to resist the dynamic cutting force in the cutting process, thereby providing support to suppress the milling cutter damage and ensure efficient, stable and secure cutting.

3.3 Formation and Evolution of Milling Cutter Damage

According to the load analysis of the milling cutter components in the previous parts of this paper, the milling cutter is subject to multiple forces in the cutting process, including the centrifugal force, the dynamic cutting force and the prestressing force. Meanwhile, the surface-to-surface contact is formed between the upper end face of the tool and the knife handle. Under the action of the axial force, the cutter handle wedge determines the horizontal direction of the cutter handle end surface which is vertical to the upper end surface of the cutting miller. Besides, the horizontal displacement of this end surface is restricted. The high speed cutting experiment related to the cutting parameters in Table 4 is carried out by adopting the high speed milling cutter structure and component materials listed in Part 3.1. The screw specification is M5.0, the locking torque is 5 Nm, and therefore the pretightening force of the milling cutter screw is 5.33 kN.

Table 4. *High speed milling test scheme*

Cutting speed v [m/min]	Milling depth a_p [mm]	Feed per tooth f [mm/r]	Milling width a_e [mm]
2000	0.5	0.08	56

Fig. 11 presents the loads and constraints imposed on the cutter in the finite element simulation.

Under the action of the centrifugal force, the dynamic cutting force and the pre-tightening force, the milling cutter is prone to suffer damage in such areas as the junction surface of the insert and the cutter body, the junction surface of the insert and the screw, the junction surface of the cutter body and the screw and the root of the cutter body and the cutter tooth. Next, these four areas will be analyzed.

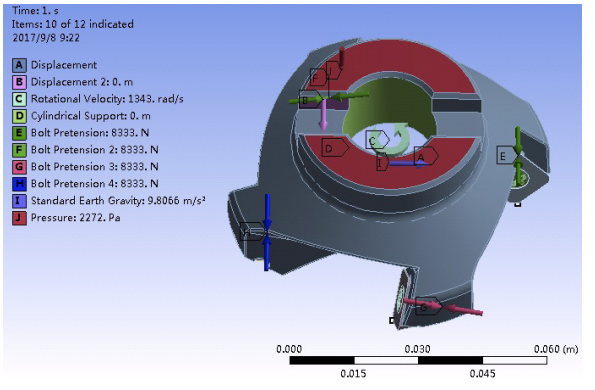

Fig. 11. *Load and constraint conditions imposed in the finite element*

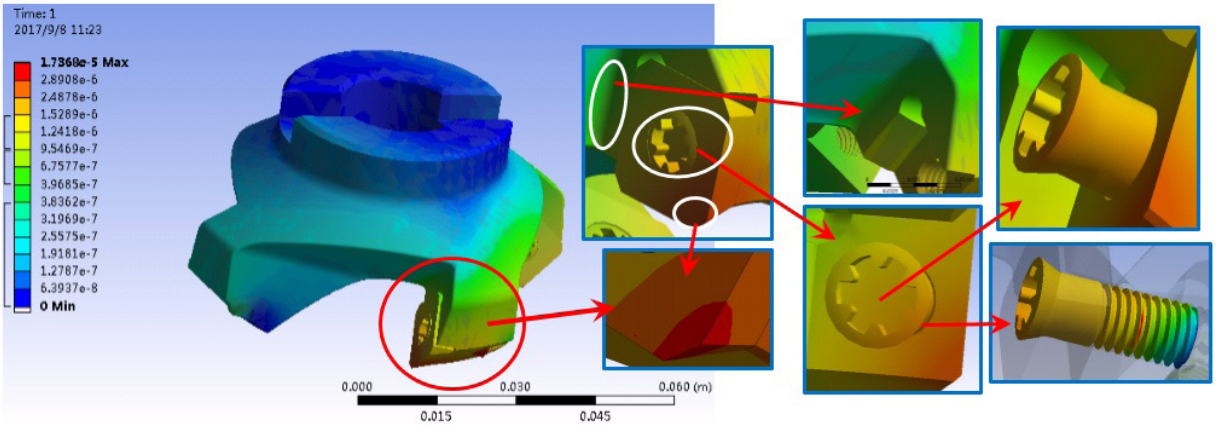

Fig. 12. *Division of the deformation zone of the milling cutter*

The deformation process of the screw head and the screw thread in high speed milling is explored, as shown in Fig. 13. It is demonstrated that the elastic deformation occurs in the screw head and the screw thread at the beginning of the process. With the continuous processing, the elastic deformation differs from the plastic deformation.

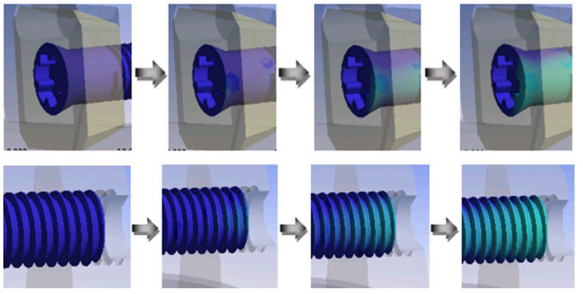

Fig. 13. *Formation and evolution of screw damage*

In this paper, the deformation process of the junction surface of the cutter body and insert in high speed milling is examined, as shown in Fig. 14. It is demonstrated that the compression deformations occur in joint surfaces. As the cutting force acts on the tool tip, the compression deformation in the tool tip is larger.

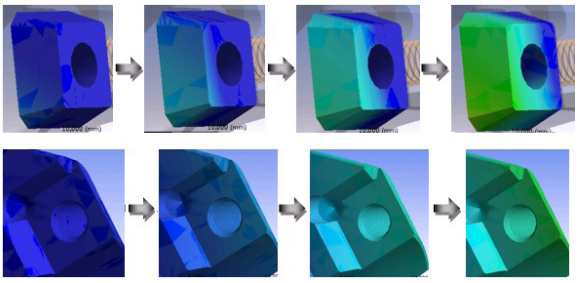

Fig. 14. *Formation and evolution of the damage to the joint surface of the insert and the cutter body*

As can be seen from the simulation analysis, the bolt pre-tightening force of the milling cutter components mainly have an impact on the locating surface of the insert and screw. The greater the pre-tightening force is, the greater the squeezing stress between the insert and the cutter body is, and the more obvious the compression deformation is. The pre-tightening force of the screw exerts an effect on mainly two parts of the insert: one is the locating surface between the insert and the cutter body, and the other is the locating surface between the insert and the screw. From the perspective of stress value, the impact of the pre-tightening force on the cutter components is not as obvious as that of the cutting force. Compression damage occurs in the joint surface of the insert and the cutter body due to the impact of the cutting force. The action direction of the pre-tightening force is consistent with that of the main cutting force, which will intensify the degree of compressive injury of the joint surface.

3.4 Cutting Conditions

The high speed milling aluminum alloy 7075 test is carried out on the MIKRON UCP710 Five-axis CNC Machining Center, and the actual experimental setup is as shown in Fig. 15. The scheme of the high speed cutting experiment is shown in Table 5.

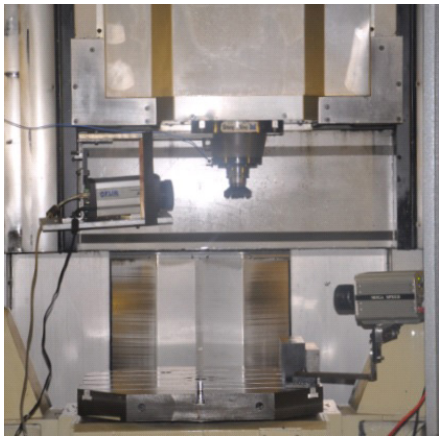

Fig. 15. *Machining field of high speed milling cutter*

Table 5. *High speed milling test schemes*

Cutting speed v [m/min]	Milling depth a_p [mm]	Feed per tooth f [mm/r]	Milling width a_e [mm]
2000	0.5	0.08	56
2600	1.0	0.15	56

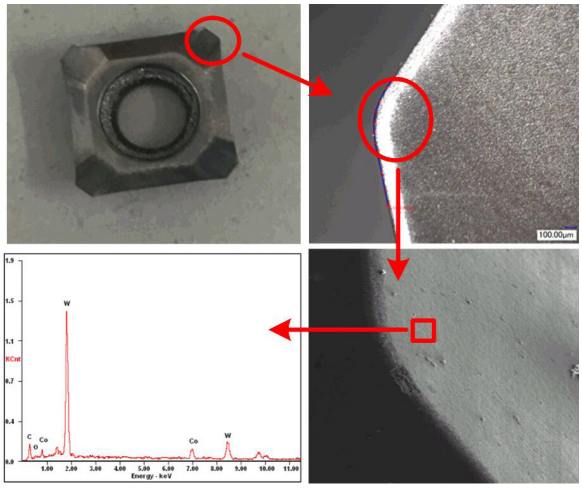

Fig. 16. *Micro morphology of milling cutter insert*

The test adopts the cutting parameters which are the same as those in simulation. Among them, the insert is WALTER SEHW1204 WKP35, which is the tungsten carbide coating, and the energy spectrums of the insert are as shown in Fig. 16.

4 RESULTS AND DISCUSSION

The simulation test was carried out on two milling cutters with the same structure and components.

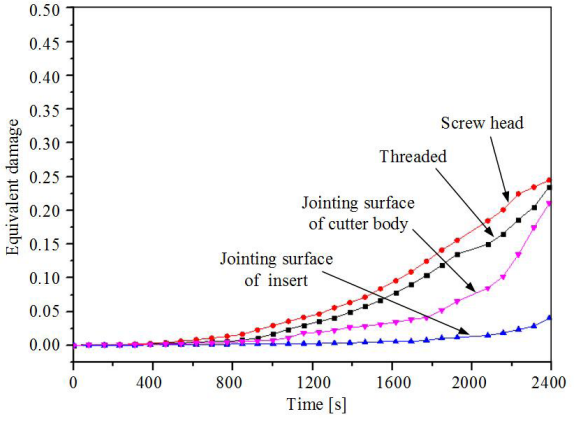

Fig. 17. *Evolution of the milling cutter tooth damage*

The evolution of the cutter tooth damage in the revised program is shown in Fig. 17. The damage degree of the screw and the junction surface of the two milling cutters are obtained through finite element simulation, as shown in Fig. 18.

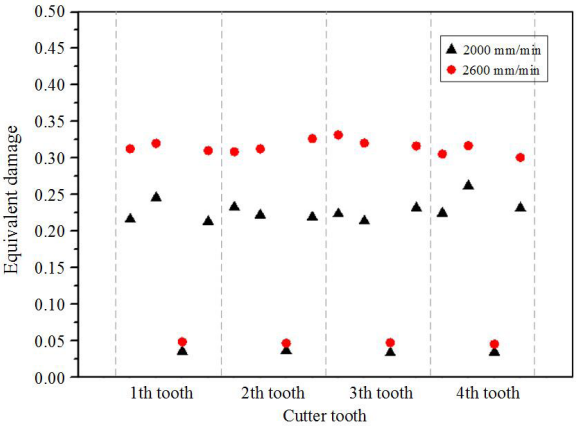

Fig. 18. *Comparison of the damage degree of each cutter tooth under different cutting parameters*

It can be seen from Fig. 18 that the milling cutter suffered from a high degree of damage at larger cutting speed, because the cutter teeth suffer from periodic

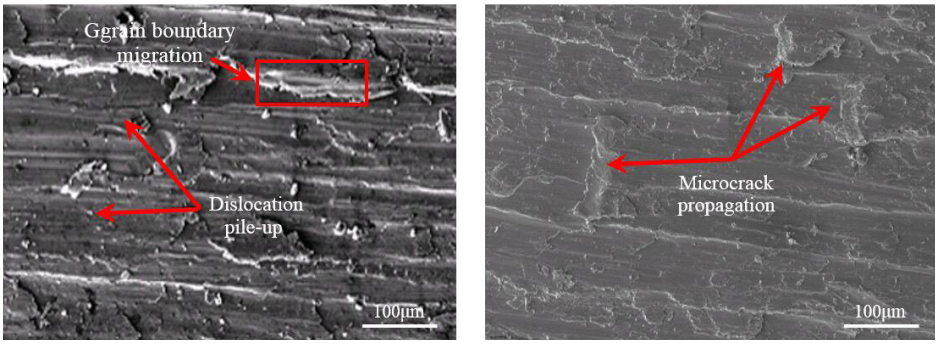

Fig. 19. *Detection results of the milling cutter joint surface*

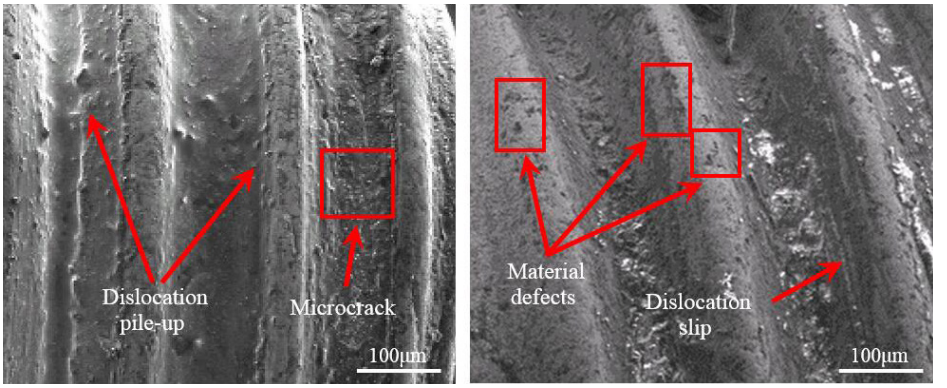

Fig. 20. *Detection results of the screw thread*

shocks constantly in the process of cutting, which causes damage to the milling cutter components. In the cutting process, different parts of the teeth suffer from different degrees of damage due to the impact of the cutter vibration, insert installation error and machine tool environment.

After cutting, the damage detection of two milling cutters is carried out, and the results are shown in Figs. 19 and 20.

The grain boundary migration, micro crack propagation and crystal surface cleavage were observed at the joint surface of the tested milling cutter with higher cutting speed by comparing and analyzing the damage detection results of two milling cutters. Obvious damage and small scale structural damage characteristic are shown. In terms of the tested milling cutter with lower cutting speed, there is only a dislocation band in the joint surface of the cutter. Dislocation slip, dislocation pileup and other micro plastic deformation mainly occur in this band, and no obvious damage or structural destruction is found. The result is consistent with that of the milling cutter damage model, which shows that the milling cutter damage evaluation method can be used to judge the damage degree of the milling cutter.

Based on the damage model, simulation and tests results of the high speed milling cutter, the damage formation and evolution process under the condition of cutting load are analyzed. The characteristic curve of the high speed milling cutter damage evolution process is shown in Fig. 21. According to the curve, the process of safety deterioration of the milling cutter caused by the damage can be proved, and the damage state of the milling cutter can be determined.

In Fig. 21, I is the damage characteristic curve of the milling cutter in the safe and stable cutting process. In this process, the injury does not continue to develop, and steady cutting is achieved later. II is the characteristic curve of the slowly developing damage which continues to evolve after occurrence until the critical value is reached. The safety performance of the milling cutter presents dynamic security recession characteristics. III is the damage characteristic curve when the milling tool passes stage I, and the damage reaches the critical value rapidly and develops continuously until the integrity failure occurs. The effect of cutting loads σ_0, σ_1 and σ_2 is mainly affected by the load conditions in the cutting process. δ_0, δ_1, δ_2 and δ_3 depend on the material properties of the milling cutter components and the macro-structure of the milling cutter.

Thus, the mathematical model of the damage characteristic curve of the milling cutter can be constructed, as shown in Eq. (15).

$$S=\begin{cases}\psi(x,\sigma) & (0\le\sigma\le\sigma_0)\\ \omega(y,\sigma) & (\sigma_0\le\sigma\le\sigma_1),\\ \xi(z,\sigma) & (\sigma_1\le\sigma\le\sigma_2)\end{cases} \tag{15}$$

where $\psi(x)$ is the constant in the constitutive relation of the milling cutter's component materials, and it determines the inherent property of the material. In the safety decline stage, the damage varies with the effect of the cutting load of the milling cutter. $\omega(x)$ is the value of the variable in the damage model. $\xi(x)$ is the critical damage to the milling cutter. As long as the yield strength of the material is reached, the cutter integrity failure occurs.

According to the previous analysis of the milling cutter damage, the damage factors of the milling cutter in the above formula are the material properties and the variables obtained by the test. The adoption of this mathematical model can provide theoretical basis for

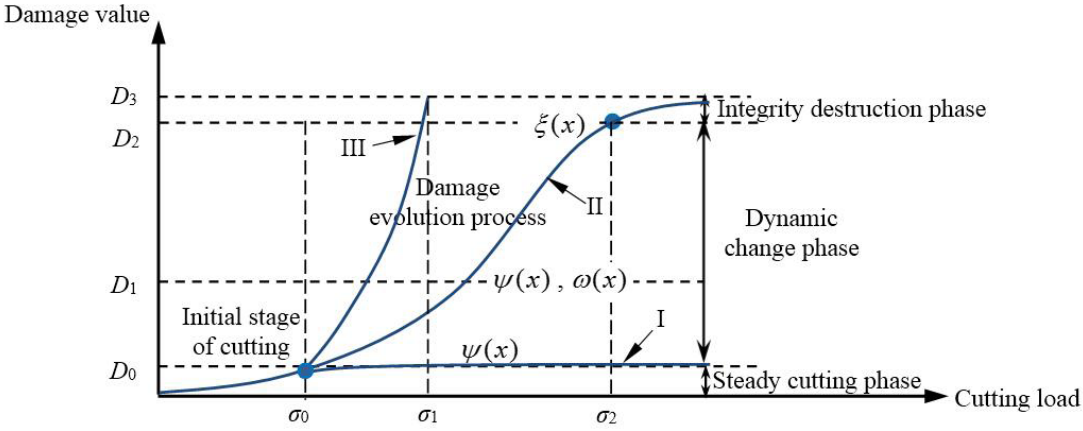

Fig. 21. *Characteristic curve of the damage process of the high speed milling cutter*

analyzing the damage to different parts of the milling cutter.

High speed milling test can be completed using the cutting parameters in Table 3. The unit cutting force is obtained, which is 483.98 N. The initial damage values of the component materials M1 and M2 are found to be 0.0075 and 0.0118, and the critical damage values are found to be 0.1243 and 0.1439, respectively based on the material constitutive relationship of the high speed milling cutter components and the equivalent damage stress value obtained from the compression test.

In order to control the occurrence and development of the damage behavior of the high speed milling cutter, the milling cutter components first meet the ISO 15641 international standard [5]. This requirement is taken to ensure the integrity of the components of the high speed milling cutter in the cutting process as an important prerequisite for the high-speed milling process. This can effectively control the large scale deformation and integrity damage of the milling cutters, but it cannot restrain small scale deformation and damage. Therefore, on the basis of the milling cutter meeting the ISO 15641 standard, the damage evaluation method of the high speed milling cutter is put forward, as shown in Fig. 22.

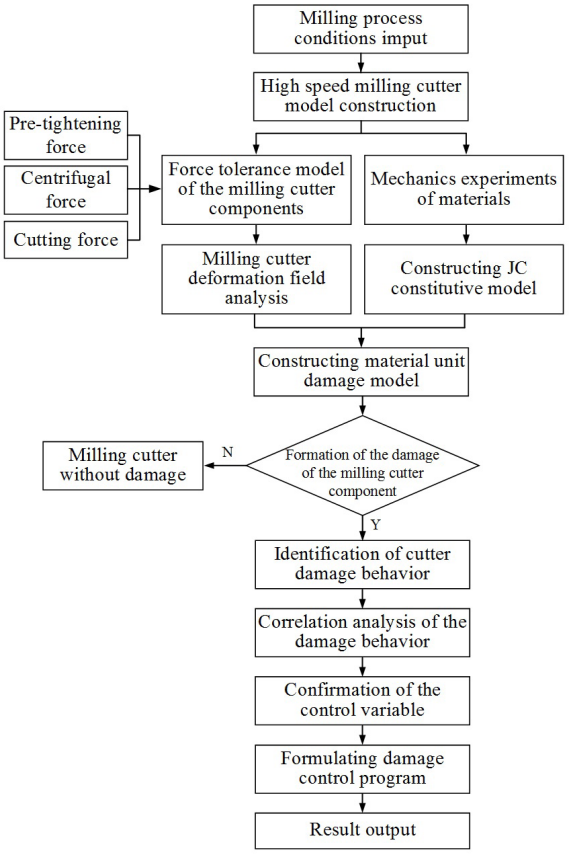

Fig. 22. *Recognition and judgment method of milling cutter damage behavior*

5 CONCLUSIONS

Under the requirements of high efficiency, high machining quality and high life expectancy for the high speed milling cutter, the decline of the cutting stability and tool life caused by the damage cannot be judged only using existing norms and standards. In this paper, the damage areas of the milling cutter are recognized, and the method of judging the damage of the milling cutter is given. The main research conclusions are as follows:

I. Under the action of the centrifugal force, the instantaneous cutting force and the pre-tightening force, the analyses of the deformation of the milling cutter components demonstrate that damage areas include: the junction surface of the insert and the cutter body, the junction surface of the insert and the screw, the junction surface of the cutter body and the screw and the root of the cutter tooth.

II. The analyses of the damage detection and the test of the mechanical property indicate that, the compression damage, ductility fracture and tensile fracture occur in the joint surfaces of the milling cutter components, due to the dislocation slip, the dislocation pile-up, the grain boundary migration and microcrack propagation generated under the action of the centrifugal force, the pre-tightening force and the cutting force.

III. The component material experiments are conducted to fit the curve of stress-strain and obtain the strain rates in instantaneous and certain action time with high strain rate and without high strain rate. Subsequently, the constitutive relationship is modeled.

IV. A model of the damage evolution of the milling cutter is established based on the equivalent damage, which can reflect the extent of the damage of the milling cutter. Combining with the finite element simulation results, the initial value and critical value of the component damage are obtained to introduce the process of the damage evolution. Finally, experimental results of two cutting test schemes are provided to verify the evaluation method of the milling cutter damage method.

6 ACKNOWLEDGEMENTS

This work is supported by the National Natural Science Foundation of China (No. 51375124).

7 REFERENCES

[1] Mativenga, P.T., Hon, K.K.B. (2005). Wear and cutting forces in high-speed machining of H13 using physical vapour deposition coated carbide tools. *Proceedings of the Institution of Mechanical Engineers, Part B: Journal of Engineering Manufacture*, vol. 219, no. 2, p. 191-199, **DOI:10.1243/095440505X8127**.

[2] Tamás, P., Illés, B. (2016). Process improvement trends for manufacturing systems in industry 4.0. *Academic Journal of Manufacturing Engineering*, vol. 14, no. 4, p. 119-125.

[3] Lin, P.T., Gea, H.C., Jaluria, Y. (2011). A modified reliability index approach for reliability-based design optimization. *Journal of Mechanical Design*, vol. 133, no. 4, p. 44-50, **DOI:10.1115/1.4003842**.

[4] Biriş, C. (2016). Considerations on manufacturing accuracy and surface quality of NC laser cutting machine tools. *Academic Journal of Manufacturing Engineering*, vol. 14, no. 2, p. 33-39.

[5] ISO 15641:2001. *Milling Cutters for High Speed Machining - Safety Requirements*. International Organization for Standardization. Geneva.

[6] Beňo, J., Maňková, I., Vrábel, M., Karpuschewski, B., Emmer, T., Schmidt, K. (2012). Operation safety and performance of milling cutters with shank style holders of tool inserts. *Procedia Engineering*, vol. 48, no. 1, p. 15-22, **DOI:10.1016/j.proeng.2012.09.479**.

[7] Ren, H., Li, X.D., Li, J.C. (2010). Numerical simulation and virtual failure of particle reinforced composite microstructure. *Journal of Mechanical Engineering*, vol. 46, no. 4, p. 35-41, **DOI:10.3901/JME.2010.04.035**.

[8] Cheng, M.H., Cao, Y.Z., Peng, H.W., Yang, G.Y. (2015). Influence of microstructural changes on the macro response of functionally graded material structures. *Materials Research Innovations*, vol. 19, no. 8, p. 835-839, **DOI:10.1179/1432891715Z.0000000001815**.

[9] Ge, C.F. (2011). The identification analysis for macro distributions curves of functionally graded materials properties based on materials components. *Advanced Materials Research*, vol. 228-229, p. 50-54, **DOI:10.4028/www.scientific.net/AMR.228-229.50**.

[10] Barabash, R.I., Bei, H., Gao, Y.F., Ice, G.E. (2010). Indentation-induced localized deformation and elastic strain partitioning in composites at submicron length scale. *Acta Materialia*, vol. 58, no. 20, p. 6784-6789, **DOI:10.1016/j.actamat.2010.09.004**.

[11] Birck, G., Iturrioz, I., Lacidogna, G., Carpinteri, A. (2016). Damage process in heterogeneous materials analyzed by a lattice model simulation. *Engineering Failure Analysis*, vol. 70, p. 157-176, **DOI:10.1016/j.engfailanal.2016.08.004**.

[12] Jiang, B., Song, J.G., Wang, S.T. (2012). Model of intrinsic/extrinsic about the safety for high speed milling tools on mesoscale. *Advanced Materials Research*, vol. 500, p. 198-204, **DOI:10.4028/www.scientific.net/AMR.500.198**.

[13] Lorenzini, G., Helbig, D., da Silva, C.C.C., Real, M.V, dos Santos, E.D., Isoldi, L.A., Rocha, L.A.O. (2016). Numerical evaluation of the effect of type and shape of perforations on the buckling of thin steel plates by means of the constructal design method. *International Journal of Heat and Technology*, vol. 34, no. 1, p. 9-20, **DOI:10.18280/ijht.34Sp0102**.

[14] Kruch, S., Chaboche, J.-L. (2011). Multi-scale analysis in elasto-viscoplasticity coupled with damage. *International Journal of Plasticity*, vol. 27, no, 12, p. 2026-2039, **DOI:10.1016/j.ijplas.2011.03.007**.

[15] Burgess, S.C. (2012). A backwards design method for mechanical conceptual design. *Journal of Mechanical Design*, vol. 134, no. 3, p. 213-221, **DOI:10.1115/1.4005620**.

[16] Faassen, R.P.H., van de Wouw, N., Oosterling, J.A.J., Nijmeijer, H. (2003). Prediction of regenerative chatter modeling and analysis of high-speed milling. *International Journal of Machine Tools and Manufacture*, vol. 43, no. 14, p. 1437-1446, **DOI:10.1016/S0890-6955(03)00171-8**.

[17] Qian, S.R., Qin, S.J., Shi, H.S. (2017). Influencing factors of peridynamics analysis and calculation. *International Journal of Heat and Technology*, vol. 35, no. 2, p. 398-402, **DOI:10.18280/ijht.350224**.

[18] Ji, S.Y., Liu, X.L., Ma, D.L., Ding, Y.P., Wu, J. (2011). Parametric design of face milling cutter based on UG template model. *Advanced Materials Research*, vol. 188, p. 336-339, **DOI:10.4028/www.scientific.net/AMR.188.336**.

[19] Horii, H., Nemat-Nasser, S. (1986). Brittle failure in compression: splitting, faulting and brittle-ductile transition. *Philosophical Transactions of the Royal Society of London, Series A: Mathematical and Physical Sciences*, vol. 319. no. 1549, p. 337-374, **DOI:10.1098/rsta.1986.0101**.

[20] Johnson, G.R., Cook, W.H. (1983). A constitutive model and data for metals subjected to large strains, high strain rates and high temperatures. *Proceedings of the 7th International Symposium on Ballistics*, The Hague, p. 541–547.

Vsebina

Strojniški vestnik - Journal of Mechanical Engineering
letnik 64, (2018), številka 2
Ljubljana, februar 2018
ISSN 0039-2480

Izhaja mesečno

Razširjeni povzetki (extended abstracts)

Strojniški vestnik - Journal of Mechanical Engineering 64(2018)2, SI 13

Prejeto v recenzijo: 2017-09-12
Prejeto popravljeno: 2018-01-06
Odobreno za objavo: 2018-01-25

Dinamska karakterizacija varjenih lameliranih struktur

Primož Ogrinec – Gregor Čepon* – Miha Boltežar
Univerza v Ljubljani, Fakulteta za strojništvo, Slovenija

Za uspešno obvladovanje vibracij in hrupnosti električnih naprav je ključen razvoj veljavnih strukturnih modelov v povezavi z modeli vzbujevalnih mehanizmov. Jedra statorjev električnih naprav so, zaradi boljšega električnega izkoristka, običajno izdelana iz paketov tankih pločevin, ki so med seboj povezane z linijskimi vari. Zaradi spreminjajočega se magnetnega polja je jedro podvrženo elektromagnetnim silam in pojavu magnetostrikcije, kar se odraža v obliki neželjenih vibracij in akustične emisije. Amplituda dinamskega odziva tovrstnih struktur je tako odvisna od velikosti vzbujevalnih mehanizmov ter od dinamskih lastnosti lamelirane strukture. Preko optimizacije strukturnih lastnosti se lahko izognemo obratovanju v območju lastnih frekvenc ter resonančnim pojavom. Za natačno in zanesljivo napovedovanje dinamskega odziva je tako potreben razvoj veljavnih dinamskih modelov s podrobno formulacijo kontakta med posameznimi lamelami. Lamelirane strukture imajo namreč bistveno manjšo togost kot ekvivalentne homogene strukture in izkazujejo ortotropno obnašanje skupaj z visokimi nivoji dušenja, ki so posledica tornih kontaktov med lamelami.

V sklopu tega dela je predstavljen numerični model varjene lamelirane strukture, kjer je strukturni model zasnovan na osnovi dvostopenjskega kontaktnega algoritma. Lamele so zamrežene z lupinskimi končnimi elementi, med katere so v normalni smeri napeti nosilčni elementi. V prvi fazi kontaktnega modela nosilčni elementi delujejo kot vzmeti, kar omogoča izračun kontaktnega tlaka med posameznimi lamelami. Tlak v normalni smeri je namreč posledica vara ter zaostalih napetosti po procesu varjenja. Le ta je predstavljen z modelom termo-elasto-plastične palice, na podlagi katerega je moč določiti skrček materiala kot posledico zaostalih napetosti v materialu. Na podlagi idenitificiranega normalnega tlaka se v drugi fazi kontaktnega modela določi materialne parametre nosilcev, s katerimi modeliramo silo trenja. Vpliv drsnega trenja med lamelami je predstavljen preko modificiranega strižnega modula nosilčnih elementov, ki ga določimo preko identificiranega kontaktnega tlaka.

Dinamski model varjene lamelirane strukture je bil validiran na osnovi izvedene dinamske analize treh statorskih paketov. Statorski paketi so se med seboj razlikovali tako z vidika geometrije kot tudi števila in razporeditve varov po obodu paketa. Izvedena primerjava lastnih frekvenc in lastnih oblik kaže dobro ujemanje med napovedjo numeričnega modela in meritvami. Glede na obstoječe raziskave razviti modela omogoča predvsem natančnejšo identifikacijo lastnih frekvenc in modalnih oblik, ki predstavljajo nihanje strukture v smeri zlaganja lamel.

Ključne besede: Lamelirana struktura, statorski paket, kontaktni model, modalna analiza

*Naslov avtorja za dopisovanje: Univerza v Ljubljani, Fakulteta za strojništvo, Aškerčeva 6, 1000 Ljubljana, Slovenija, gregor.cepon@fs.uni-lj.s

Strojniški vestnik - Journal of Mechanical Engineering 64(2018)2, SI 14

Prejeto v recenzijo: 2017-04-25
Prejeto popravljeno: 2017-07-15
Odobreno za objavo: 2017-08-24

Vpliv zračnosti v zgibih na natančnost gibanja robotskih manipulatorjev

Selçuk Erkaya*
Univerza Erciyes, Oddelek za mehatroniko, Turčija

Cilj pričujoče študije je preučitev vpliva zračnosti v zgibih na natančnost gibanja robotskega sistema. Predmet analize občutljivosti gibanja je trajektorija vrha robota. Ocenjena je kinematika in dinamika robotov s šestimi prostostnimi stopnjami z zračnostjo v zgibu in brez nje. Pri izvajanju zahtevanega gibanja so bili upoštevani različni scenariji za vrednost zračnosti in trajanje delovnih ciklov. Odstopanja od zahtevane trajektorije med delovnim procesom so bila napovedana s pomočjo modela v obliki nevronske mreže.

Tudi pri zelo natančni konstrukciji in izdelavi celotnega sistema se ni mogoče popolnoma izogniti problemu zračnosti v zgibih. Za zagotovitev natančnosti pozicioniranja vrha robota je treba kvantificirati vpliv negotovih dejavnikov ter določiti optimalne tolerance/zračnosti. V ta namen so bile preučene neobčutljivosti gibanja, ki izhajajo predvsem iz zračnosti v zgibih na robotskem manipulatorju. Za študijo primerov in primerjavo so bile izbrane tri vrednosti zračnosti v nepopolnem referenčnem zgibu (zgib št. 5): 0,2, 0,4 in 0,6 mm. Izbrani sta bili tudi dve vrednosti za trajanje delovnega cikla: 6 in 12 sekund. Za napovedovanje odstopanj trajektorije zaradi zračnosti v zgibu je bil uporabljen model dinamične nevronske mreže.

Pri zgibih z zračnostjo obstajajo različne vrste relativnega gibanja med deli zgiba: prosto gibanje, udarno gibanje in stalen stik. Različne vrste gibanj vplivajo na kinematične in dinamične lastnosti sistema. Model kontaktne sile je pomemben za popis dinamike trkov med tečajem in ležajem v zgibu z zračnostjo. Predvsem zaradi enostavnosti modela kontaktne sile, njegove uporabnosti pri udarcih v sistemu več teles, preprostih izračunov in hitre konvergence je bila dinamika sistema z zračnostjo v zgibih popisana z modelom, ki sta ga razvila Lankarani in Nikravesh. Torne lastnosti med tečajem in ležajem so bile popisane s prilagojenim modelom Coulombovega trenja. Razvit je bil dinamični model robotskega manipulatorja, ki upošteva različne vrste gibanj zaradi zračnosti v zgibu.

Zračnost v zgibih povzroča impulzne kontaktne sile. Te sile se pojavijo v krajšem časovnem intervalu. Vršne sile se pojavijo ob začetku gibanja. Robotski manipulator z zračnostjo v zgibu ima večjo vršno frekvenco v krajšem delovnem ciklu. Ko se povečuje zračnost, se poveča tudi amplituda kontaktne sile. Ta lastnost sile ne zmanjšuje le občutljivosti gibanja in ponovljivosti robotskega manipulatorja, temveč privede tudi do poslabšanja lastnosti, povezanih z vibracijami in hrupom. Dinamika robotskega manipulatorja je očitno odvisna od zračnosti in od delovnega cikla. S povečanjem zračnosti se poveča tudi odstopanje od trajektorije. Odstopanja so bolj kaotična takrat, ko je treba delovno nalogo opraviti v krajšem času. Bolj izražena načina prostega gibanja in udarcev sta glavni razlog za izpolnitev iste trajektorije v krajšem delovnem ciklu z večjo hitrostjo. Ta odstopanja je mogoče napovedati z modelom nevronske mreže z ustreznimi vhodnimi spremenljivkami. Rezultati korelacij dobro potrjujejo sposobnost predlaganega modela nevronske mreže za napovedovanje pravih odstopanj.

V bližnji prihodnosti bodo ti rezultati nadgrajeni z dodatnimi raziskavami sistemov z več zgibi, vpliva mazanja, obrabe itd.

Zračnost v zgibu očitno vpliva na kinematiko in dinamiko sistema ter povzroča impulzne kontaktne sile/momente v krajšem časovnem intervalu. Tako velikost zračnosti kot trajanje delovnega cikla sta pomembna vplivna dejavnika pri vršni amplitudi in frekvenci. Raziskovalci bodo lahko uporabili te rezultate pri preučevanju neželenih vplivov zračnosti v zgibih na delovanje robotskih sistemov ter izboljšali občutljivost gibanja s snovanjem robustnih krmilnih sistemov za ustvarjanje potrebnih krmilnih izhodov.

Ključne besede: napaka trajektorije, zračnost v zgibu, model NARX, natančnost 3D-gibanja, negotovost

*Naslov avtorja za dopisovanje: Univerza Erciyes, Oddelek za mehatroniko, 38039 Kayseri, Turčija, erkayaselcuk@gmail.com

Strojniški vestnik - Journal of Mechanical Engineering 64(2018)2, SI 15

Prejeto v recenzijo: 2017-07-18
Prejeto popravljeno: 2017-12-11
Odobreno za objavo: 2017-12-18

Optimizacija hidrostatičnih ležajev vrtilne mize po metodi optimizacije roja delcev za zmanjšanje porabe energije

Yumo Wang[1] – Zhifeng Liu[1,*] – Ligang Cai[1] – Qiang Cheng[1] – Xiangmin Dong[2]

[1] Državni laboratorij za napredne proizvodne tehnologije, Tehniška univerza v Pekingu, Peking, Kitajska
[2] Oddelek za strojništvo, Kolidž za naftno industrijo Chengde, Chengde, Kitajska

Hidrostatična vrtilna miza je pomemben del računalniško numerično krmiljenih (CNC) obdelovalnih strojev, saj nosi obdelovanec in izvaja zelo natančno vrtilno gibanje. Delovanje hidrostatične vrtilne mize je močno odvisno od geometrije oljnih blazinic in s pravilno konstrukcijo je mogoče doseči zmanjšanje porabe energije ter izboljšanje zmogljivosti vrtilne mize.

Olje pod tlakom v oljne blazinice nenehno dovaja zunanji sistem in obratovalne stroške hidrostatične vrtilne mize je tako mogoče zmanjšati z zmanjšanjem moči za pogon opreme, potrebne za oskrbo z oljem. Analiza in optimizacija hidrostatičnih ležajev je zahtevna naloga, ki zahteva obsežne numerične analize, geometrijska točnost izdelave oljne blazinice pa je odvisna od sposobnosti obdelovalnega procesa. Za optimizacijo hidrostatičnega ležaja je zato potreben učinkovit in dovolj točen optimizacijski algoritem, kot je optimizacija z rojem delcev (PSO). To je učinkovita numerična metoda, ki zahteva manjše računske kapacitete. V članku je predstavljena optimizacija konstrukcije oljnih blazinic hidrostatične vrtilne mize po metodi optimizacije roja delcev, ki izboljša nosilnost in zmanjša stroške rabljene energije. Reynoldsova enačba za izračun porazdelitve tlaka in pretoka olja do ležajev je bila razrešena po metodi končnih diferenc. Strošek energije, rabljene za dovajanje olja, je odvisen od delovnega režima vrtilne mize, optimalna rešitev pa pomeni minimalno porabo energije. Geometrijski parametri oljne blazinice v metodi PSO konvergirajo v optimalen rezultat.

Predlagana je praktična metoda za optimizacijo hidrostatične vrtilne mize na podlagi PSO, ki izboljšuje njeno delovno zmogljivost. Reynoldsova enačba hidrostatične vrtilne mize je prilagojena delovnemu stanju, obratovalne značilnosti, kot sta porazdelitev tlaka in pretok olja, pa so bile določene po metodi končnih razlik (FDM). Nosilnost oljne blazinice je mogoče opisati z brezdimenzijsko nosilnostjo in z brezdimenzijskim pretokom. Brezdimenzijska nosilnost ustreza sili oljnih blazinic, brezdimenzijski pretok pa pretoku olja, ki je potreben za vzdrževanje debeline oljnega filma. Sprememba velikosti žepa za olje vpliva tako na brezdimenzijsko nosilnost kakor tudi na brezdimenzijski pretok. Za optimizacijski parameter je bila izbrana geometrija oljnih blazinic. Minimalna debelina oljnega filma je bila nastavljena na konstantno varnostno raven, kot kriterij za vse parametre pa je bila izbrana poraba moči. Optimalna rešitev je bila določena z algoritmom PSO.

Razsežnost žepa za olje močno vpliva na rabo energije. Pravilno oblikovan žep zmanjša potrebno moč za nošenje ter izboljša delovanje hidrostatične vrtilne mize.

Pri konstantni (varnostni) debelini filma je bila izračunana optimalna velikost žepa je 0,5431. Z večanjem debeline filma se povečuje potrebna moč za nošenje, optimalna velikost žepa pa ostaja praktično nespremenjena. Ta se pri različnih debelinah filma ne spreminja za več kot 7 %.

Obratovalne značilnosti, kot sta porazdelitev tlaka in pretok olja, so bile določene z Reynoldsovo enačbo in FDM. Odvisnost med razsežnostjo žepa za olje in potrebno močjo za nošenje je bila določena numerično, zanesljivost algoritma pa je bila določena eksperimentalno na miniaturnem preizkuševališču. Optimalna velikost žepa za minimalno moč črpalke je bila določena po metodi PSO. V članku je predstavljena učinkovita in praktična optimizacijska metoda za konstruiranje hidrostatičnih vrtilnih miz.

Ključne besede: hidrostatična vrtilna miza, Reynoldsova enačba, PSO, zmogljivost ležaja, varčevanje z energijo, eksperiment

*Naslov avtorja za dopisovanje: Državni laboratorij za napredne proizvodne tehnologije, Tehniška univerza v Pekingu, Peking, Kitajska, lzfeng1@126.com

Strojniški vestnik - Journal of Mechanical Engineering 64(2018)2, SI 16

Prejeto v recenzijo: 2017-11-04
Prejeto popravljeno: 2018-01-08
Odobreno za objavo: 2018-01-24

Določitev tlačnega odziva zaprtocelične aluminijaste pene in linearno-elastična simulacija geometrijskih modelov, neposredno rekonstruiranih iz posnetkov μCT, po metodi končnih elementov

Tamás Mankovits[1,*] – Tamás Antal Varga[1] – Sándor Manó[2] – Imre Kocsis[1]

[1]Tehniška fakulteta, Univerza v Debrecenu, Madžarska
[2]Medicinska fakulteta, Univerza v Debrecenu, Madžarska

Kovinske pene imajo lahko celično strukturo z odličnimi mehanskimi in fizikalnimi lastnostmi. Znano je, da imajo te pene veliko tlačno trdnost in da dobro absorbirajo energijo, zato se povečuje zanimanje za njihovo uporabo pri nalogah dušenja vibracij in absorbiranja zvoka, kakor tudi na področju nosilnih konstrukcijskih elementov. Mnoge aplikacije se zanašajo na tlačne lastnosti kovinskih pen, ki so neposredno odvisne od njihove strukture. Kovinska pena, kot nosilni konstrukcijski element (npr. del vozila, biomedicinski vsadek), mora biti v delovnih pogojih elastična, zato je treba natančno napovedati odziv materiala v elastičnem območju.

Razvoj učinkovitega postopka za tridimenzionalno modeliranje in simulacijo kovinskih pen po metodi končnih elementov je še vedno eden večjih izzivov za inženirje. Numerično določanje tlačnih lastnosti penaste strukture je zahtevna tehnična naloga, ki pa je pri konstruiranju nepogrešljiva. Pri projektiranju nosilnih konstrukcij iz kovinskih pen je treba upoštevati elastično vedenje v delovnih pogojih, za tehnične preračune dejanske penaste strukture pa so potrebni tudi natančni geometrijski modeli.

Obravnavana zaprtocelična kovinska pena je bila izdelana iz kompozitnega materiala s kovinsko osnovo Duralcan F3S.20S po postopku neposrednega penjenja z dodajanjem penila. Preskušanci so bili zaradi primerljivosti okarakterizirani po vodilnem standardu za tlačne preskuse poroznih materialov. Tlačni preskusi so bili opravljeni pri sobni temperaturi na univerzalnem preskuševalnem stroju INSTRON 8874, in sicer brez lubrikanta. Za kakovostne napovedi odziva poroznih materialov je treba postaviti modele po metodi končnih elementov, ki ustrezno opisujejo dejansko geometrijo.

Nedavne študije so pokazale, da je rentgenska računalniška tomografija učinkovito in zmogljivo orodje za neinvazivno in neporušno snemanje celotne strukture materialov. Programska oprema omogoča nastavitev uporabniških parametrov za vsak korak transformacije, določiti pa je mogoče tudi vrstni red transformacij in tako doseči različne lastnosti modela. Pomemben del postopka je tudi ročna rekonstrukcija predmetov s kompleksno geometrijo. Prvi korak je priprava prerezov (posnetkov CT) z vzporednimi ravninami dane gostote. Drugi korak je izvedba zaporedja transformacij, ki dajo geometrijsko točen tridimenzionalni objekt, primeren za analizo po metodi končnih elementov.

Raziskava preskušancev je dokazala, da točnost predlagane rekonstrukcijske metode izpolnjuje zahteve ter da je postopek ponovljiv in ga je mogoče validirati. Pripravljeni so bili računski modeli eksperimenta, sestavljenega iz preskušanca iz aluminijaste pene in dveh togih plošč. V modelu je bil privzet stik brez trenja, toga zgornja plošča je imela vnaprej določen odmik, spodnja fiksna plošča pa je bila uporabljena za meritev odzivne sile.

Predlagani postopek omogoča raziskave dejanske strukture kot tridimenzionalnega modela iz kateregakoli materiala, ki ga je mogoče analizirati na podlagi posnetkov CT. Geometrijska rekonstrukcija in rezultati izračunov po metodi končnih elementov izkazujejo dobro korelacijo z izmerjenimi vrednostmi v elastičnem območju, s čimer je dokazana uporabnost predstavljene metode.

Ključne besede: zaprtocelična pena, geometrijska rekonstrukcija, tlačni preskus, metoda končnih elementov

*Naslov avtorja za dopisovanje: Tehniška fakulteta, Univerza v Debrecenu, Ótemető 2-4, H-4028 Debrecen, Madžarska, tamas.mankovits@eng.unideb.hu

Strojniški vestnik - Journal of Mechanical Engineering 64(2018)3, SI 17

Prejeto v recenzijo: 2017-11-16
Prejeto popravljeno: 2018-01-19
Odobreno za objavo: 2018-02-09

Vpliv notranjega prenosnika toplote pri uporabi R1234ze(E) kot alternativnega hladiva v mobilni klimatski napravi

Mehmet Direk[1,*] – Eren Soylu[2]
[1]Univerza v Yalovi, Fakulteta za strojništvo, Turčija
[2]Univerza v Yalovi, Znanstveno-tehniški inštitut, Turčija

Hladiva z majhnim potencialom globalnega segrevanja (GWP) so zaradi okoljskih omejitev začela zamenjevati fluorirane ogljikovodike (HFC). V zadnjem času večina mobilnih klimatskih naprav (MAC) deluje s hladivom R134a (GWP = 1300). Evropska Direktiva 2006/40/ES in Uredba 517/2014 za mobilne klimatske naprave omejujeta uporabo HFC s številom GWP, večjim od 150. Ena od alternativ za R134a z manjšim GWP je R1234ze(E), ki ima podobne termofizikalne lastnosti in zelo majhno vnetljivost. V predstavljeni študiji je bila eksperimentalno raziskana uporaba hladiva R1234ze(E) v napravi MAC, ki je bila sprva projektirana za hladivo R134a. Določen je bil tudi vpliv notranjega prenosnika toplote (IHX) na delovanje MAC s hladivom R1234ze(E). Preizkušena in primerjana sta bila dva različna primera uporabe R1234ze(E) z in brez IHX, kot referenca pa je bilo uporabljeno delovanje sistema, napolnjenega s hladivom R134a. V ta namen je bil zgrajen eksperimentalni sistem MAC, projektiran za hladivo R134a.

Ovrednoteni sta bili energijska in eksergijska učinkovitost ploščatega izmenjevalnika toplote in raziskano je bilo uničenje eksergije v komponentah sistema. Parametri delovanja sistema so bili določeni z različnimi vrtilnimi frekvencami kompresorja. Raziskani parametri delovanja so bili hladilna zmogljivost, moč kompresorja, hladilno število (COP), uničenje eksergije in porazdelitev uničenja eksergije po komponentah sistema. Količina R134a v sistemu je bila določena glede na najboljšo vrednost hladilnega števila. Količina polnitve za ekvivalentno maso v sistemu je bila izračunana s pomočjo gostot tekočega hladiva. V eksperimentalni študiji je bil sistem napolnjen s 600 g hladiva R134a in s 625 g hladiva R1234ze, skladno z gostoto tekočega hladiva. Temperatura zraka na vhodu v uparjalnik in kondenzator je bila konstantnih 27 oz. 35 °C. Vrtilna frekvenca kompresorja se je med eksperimentom spreminjala med 750 in 2750 vrt/min v korakih po 500 vrt/min.

Rezultati so pokazali, da je masni pretok hladiva R134a za 17 % večji kot pretok R1234ze(E). Porabljena mehanska moč pri R134a je zato večja kot pri R1234ze(E). Ko je bil sistemu dodan IHX, se je povečala vrednost pregrevanja R1234ze(E). Gostota par R1234ze(E) je manjša od gostote par R134a, hladivo R1234ze(E) pa ima po drugi strani za 7 % manjšo izparilno toploto kot R134a, zaradi česar je zmogljivost hlajenja pri enakem uparjalnem tlaku manjša. Hladivo R1234ze(E) ima tako v povprečju za 27 % manjšo hladilno zmogljivost. IHX poveča latentno toploto s povečanjem vrednosti podhladitve. Hladilna zmogljivost se je po uvedbi IHX povečala za 7 %. Hladilno število pri R1234ze(E) je bilo za 8 % do 10 % manjše kot pri R134a. Ko je bil sistemu dodan IHX, se je hladilno število povečalo za 4 %. Po aktivaciji notranjega prenosnika toplote se je povečala tudi vrednost uničenja eksergije. Sledi sklep, da je R1234ze(E) primerno alternativno hladivo za aplikacije mobilnih klimatskih naprav, če so opravljene določene prilagoditve.

Ključne besede: R134a, R1234ze(E), mobilne klimatske naprave, hladilno število, notranji prenosnik toplote

*Corr. Author's Address: Univerza v Yalovi, Fakulteta za strojništvo, Turčija, mehmetdirek@hotmail.com

Strojniški vestnik - Journal of Mechanical Engineering 64(2018)2, SI 18

Prejeto v recenzijo: 2017-09-20
Prejeto popravljeno: 2018-01-11
Odobreno za objavo: 2018-01-29

Modifikacija površine in obrabne lastnosti neposredno lasersko sintranih hibridnih kovinskih orodij za brizganje plastike

István Hatos[1,*] – Imre Fekete[1] – Tamás Ibriksz[1] – József G. Kovács[2] – Mária B. Maros[3] – Hajnalka Hargitai[1]

[1] Univerza Széchenyi István, Oddelek za materiale in tehnologijo, Madžarska
[2] Univerza za tehniko in ekonomijo v Budimpešti, Oddelek za inženiring polimerov, Madžarska
[3] Univerza v Miskolcu, Oddelek za mehansko tehnologijo, Madžarska

Injekcijsko brizganje je eden najproduktivnejših postopkov predelave plastičnih mas. Razvoj izdelkov in nenehno skrajševanje časa proizvodnje zahtevata nove rešitve pri konstruiranju in izdelavi orodij. Neposredno lasersko sintranje kovin (DMLS) omogoča izdelavo orodij s posebnimi ukrivljenimi hladilnimi kanali, ki sledijo geometriji dela (konformno hlajenje). Ena od slabosti DMLS so veliki stroški, ki pa jih je mogoče drastično zmanjšati z gradnjo hibridnih konstrukcij. Z uporabo osnovne plošče iz običajnega orodnega jekla, na katero se montira sintran del s posebno geometrijo, se dokončna geometrija po sintranju doseže s konvencionalnimi obdelovalnimi tehnologijami.

V predstavljeni študiji je bil uporabljen postopek DMLS za izdelavo hibridnih konstrukcij, ki združujejo konvencionalne obdelovalne tehnologije s postopki za hitro izdelavo prototipov. Za osnovni material sta bila izbrana maraging jeklo W722 z enakovredno kemično sestavo kot pri prahu za sintranje in konvencionalno orodno jeklo 1.2343, za lasersko sintanje pa je bil uporabljen prah maraging jekla MS1. Po izdelavi so bile uporabljene različne toplotne obdelave (utrjanje s staranjem, gašenje, gašenje z dvojnim popuščanjem, nitrocementiranje in oksinitriranje). Nato je bila opravljena karakterizacija mikrostrukture, trdote in obrabnih lastnosti različnih jekel, preučitev hibridnih konstrukcij in tribološka analiza le-teh.

Izkazalo se je, da so v različnih proizvodnih postopkih nastale različne mikrostrukture lasersko sintranega in toplo valjanega maraging jekla, kakor tudi večja poroznost lasersko sintranega materiala. Primerjava vplivov utrjanja s staranjem in gašenja na trdoto različnih kvalitet jekel je pokazala, da je z utrjanjem maraging jekel s staranjem dosegljiva praktično enaka trdota kot z gašenjem, medtem ko je enaka toplotna obdelava pri jeklu 1.2343 povzročila zmehčanje. Trdota jekla MS1 je bila enaka po gašenju in po utrjanju s staranjem. Parametri toplotne obdelave imajo velik vpliv na mehanske lastnosti. Pri hibridnih konstrukcijah je zato zelo pomembna izbira postopka in parametrov toplotne obdelave, ki zagotavljajo zahtevane lastnosti pri obeh komponentah.

Preučeno je bilo tudi prehodno območje pri hibridnih delih MS1-W722 in MS1-1.2343. Analiza ESD je pokazala zvezno spreminjanje koncentracije elementov v prehodnem območju. Med materialoma v hibridnem delu ni ostre meje, tako glede mikrostrukture kot glede mehanskih lastnosti.

Eksperimentalno je bilo potrjeno, da so lasersko sintrani deli poroznejši od delov iz konvencionalnih jekel, s čimer je mogoče pojasniti manjšo obrabno obstojnost vzorcev iz jekla M1 v primerjavi z vzorci iz maraging jekla W722, ki so bili izdelani iz običajne jeklene palice. Večjo obrabno obstojnost jekla 1.2343 v primerjavi z obstojnostjo maraging jekla je mogoče pripisati večji vsebnosti ogljika in večji površinski trdoti. Po uporabi nitrocementiranja se je drastično zmanjšala obrabljena površina kot indikator obrabne obstojnosti, in pri vseh jeklih je bila dosežena praktično enaka vrednost. Sintrano maraging jeklo ima v vseh primerih manjšo obrabno obstojnost kot deli iz konvencionalno izdelanega jekla, kar je mogoče pojasniti z večjo poroznostjo po sintranju.

Iz rezultatov sledi zaključek, da nitrocementiranje učinkovito izboljšuje obrabne lastnosti hibridnih orodij. Kadar se orodno jeklo uporablja v hibridnih konstrukcijah, ki za doseganje predpisanih lastnosti zahtevajo gašenje, je s to toplotno obdelavo mogoče doseči enako trdoto dela iz jekla MS1 kot pri utrjanju s staranjem, če gašenju sledi visokotemperaturno popuščanje.

Ključne besede: neposredno lasersko sintranje kovin, hibridna konstrukcija, maraging jeklo, jeklo 1.2343, toplotna obdelava, obraba, prehodno območje

*Naslov avtorja za dopisovanje: Univerza Széchenyi István, Oddelek za materiale in tehnologijo, Egyetem square 1, Győr, Madžarska, hatos@sze.hu

Strojniški vestnik - Journal of Mechanical Engineering 64(2018)2, SI 19

Prejeto v recenzijo: 2017-11-07
Prejeto popravljeno: 2017-12-12
Odobreno za objavo: 2017-12-21

Metoda za ocenjevanje poškodbenih lastnosti zob visokohitrostnih rezkarjev

Minghui Zhang – Minli Zheng* – Bin Jiang
Znanstveno-tehniška univerza v Harbinu, Nacionalni in lokalni tehnični laboratorij za visokoučinkovito odrezavanje in orodja, Kitajska

Pri obdelavi z visokohitrostnimi rezkarji se pojavljajo lokalne poškodbe orodja, ki ogrožajo varnost in skrajšujejo življenjsko dobo orodja, posledično pa izničijo tehnične prednosti visokozmogljive in visokonatančne obdelave. Poškodbe zob rezkarjev je tudi težko napovedati, kar povzroča težave pri izboljševanju stabilnosti in učinkovitosti delovanja rezkarjev. Zato obstaja potreba po raziskavah poškodb zob visokohitrostnih rezkarjev.

Zaradi poškodb visokohitrostnega rezkarja se spremenijo dinamične lastnosti orodja, ki jih popisujemo z različnimi indeksi poškodb. Identifikacija vrst poškodb omogoča vizualno primerjavo stanja rezkarja pred poškodbo in po njej. V članku so analizirane vrste in mehanizmi oblikovanja poškodb rezkarjev z namenom vzpostavitve modela, ki bo uporaben za računanje poškodb rezkarja pod vplivom centrifugalne sile, dinamičnih rezalnih sil in sil prednapetja. Stopnja poškodbe zob rezkarja je popisana z ekvivalentno poškodbo. Začetne in kritične vrednosti poškodb so določene s simulacijo odrezavanja in s preskusom visokohitrostnega rezkanja. Predstavljena je metoda za prepoznavanje in ocenjevanje poškodb rezkarja. Možnost vrednotenja poškodb rezkarja predstavlja prednost pri optimizaciji parametrov rezkanja ter izboljšuje učinkovitost obdelave. Glavni zaključki raziskave so:

I. Analiza deformacij komponent rezkarja pod vplivom centrifugalne sile, trenutne rezalne sile in sile prednapetja je razkrila naslednja mesta poškodb: stična površina med ploščico in telesom rezkarja, stična površina med ploščico in vijakom, stična površina med telesom rezkarja in vijakom ter koren zoba.
II. Analize odkritih poškodb in preskusi mehanskih lastnosti so pokazali, da na stičnih površinah komponent rezkarja prihaja do tlačnih poškodb, duktilnega in nateznega zloma zaradi drsenja dislokacij, zbiranja dislokacij, migracije kristalnih mej in napredovanja mikrorazpok pod vplivom centrifugalne sile, sile prednapetja in rezalnih sil.
III. Opravljeni so bili preskusi materialov komponent za določitev krivulje odvisnosti deformacij od napetosti in preoblikovalne hitrosti z visoko hitrostjo obremenjevanja in brez nje. Oblikovan je ustrezen konstitutivni model.
IV. Postavljen je model razvoja poškodb rezkarja na podlagi ekvivalentne poškodbe, ki lahko odraža razsežnost poškodbe rezkarja. V kombinaciji z rezultati simulacije po metodi končnih elementov sta določeni začetna in kritična vrednost poškodbe komponent za uvedbo procesa razvoja poškodbe. Končno so podani rezultati eksperimentov z dvema shemama odrezavanja za verifikacijo metode ocenjevanja poškodbenega modela rezkarja.

Visokohitrostno rezkanje je razširjeno v proizvodni industriji zaradi odlične zmogljivosti in ekonomskih prednosti. V članku je preučen mehanizem poškodb visokohitrostnih rezkarjev za podaljšanje varnega in stabilnega časa odrezavanja ter za izboljšanje učinkovitosti in kakovosti obdelave. Članek tako predstavlja pomembno teoretično in tehnično osnovo za snovanje učinkovitejših in varnejših rezalnih orodij, pozitivno vlogo pa ima tudi pri razvoju in uporabi tehnologije visokohitrostnega rezkanja.

Ključne besede: visokohitrostni rezkar, material komponent, hitrost obremenjevanja, poškodbeni model, analiza po metodi končnih elementov, poškodbene lastnosti

*Naslov avtorja za dopisovanje: Znanstveno-tehniška univerza v Harbinu, Xuefu Road 52, Harbin, Kitajska, mh_zhang610@hotmail.com